Fracture of Fillet Welds Under Extreme Loading

by

Athanasios G. Sampos

B.S. in Marine Engineering Hellenic Naval Academy, 1988

Submitted to the Department of Ocean Engineering
and Materials Science and Engineering
in partial fulfillment of the requirements for the degrees of

Naval Engineer

and

Master of Science in Materials Science

at the

MASSACHUSETTS INSTITUTE OF TECHNOLOGY

June 1996

Author .....
Department of Ocean Engineering
May 10, 1996

Certified by .....
Koichi Masubuchi, Kawasaki Professor of Engineering
Thesis Supervisor, Department of Ocean Engineering

Certified by .....
Frederick J. McGarry, Professor of Civil Engineering and Polymer
Thesis Reader, Department of Materials Science and Engineering

Accepted by .....
Douglas A. Carmichael, Professor of Power Engineering
Chair, Departmental Committee on Graduate Students

Accepted by .....
Michael F. Rubner, TDK Professor of Materials Science and Engineering
Chair, Departmental Committee on Graduate Students

Fracture of fillet welds under extreme loading

by
Athanasios G. Sampos

Submitted to the Departments Ocean Engineering
and Materials Science and Engineering
on May 10, 1996, in partial fulfillment of the
requirements for the degrees of
Naval Engineer
and
Master of Science in Materials Science

Abstract

An experimental study was carried out on the performance of the fillet welds under conditions of extensive plastic deformation, applied for more than one cycles. The experiment was specially designed to simulate a ship structural detail subjected to loading encountered during incidents of ship collision or grounding. The effect of the structural geometry and the weld defects was examined. The video microscope was extensively used to gather images of the critical to fail area during the experiment. Cracking initiation and propagation were recorded.

Fracture was observed to take place either in the longitudinal fillet tearing mode or in the opening mode at the toe of the fillet weld. The tearing resistance of the weld was calculated for the case where peeling fracture occurred. The effect of the stress concentration at the toe of the weld on the opening fracture mode was examined. Most of the failures occurred at the second loading cycle.

Peeling fracture under alternating plasticity can be avoided by maintaining the fillet weld in the elastic range. Fracture at the second cycle is more likely to occur because the changes in the deformation behavior of the material impose larger strain concentration at the highly stressed areas. Weld defects reduce the fracture resistance of the structure under extreme plasticity as far as they create strain concentration or reduce the amount of the deforming material.

The video microscope was proven to be portable, maneuverable in close areas and required no specials skills to use. Therefore, it can be used for on-site structural detail inspections, besides being an experiment tool.

Thesis Supervisor : Koichi Masubuchi

Title : Kawasaki Professor of Engineering

Acknowledgments

I would like to thank my thesis advisor, Professor Masubuchi, for his guidance and support. I am grateful to Professor McGarry not only for being my thesis reader, but also because, as my first teacher in fracture, he raised my interest in that subject. I also give thanks to Professor McClintock for his insightful comments and advice. Special thanks to LiLiang and Tony Zona for their involvement throughout this thesis. Finally, I would like to thank my family and friends who continuously supported me during my studies.

Table of Contents

List of Figures

List of Tables

1. Introduction

Ships are the largest mobile structures built by man, and both their size and requirement for mobility exert strong influences on their structural arrangement and design. The ship's structural components usually perform a multipurpose function, besides providing the structural integrity of the ship. Because of its multifunctionality, ship structure requires plate or sheet-type members arranged in combination with system of stiffeners. The requirement to provide resistance to multiple load components, while supporting other ship functions (watertight integrity, shell fairness, access, arrangeable areas, etc.), increases considerably the complexity of a ship structure and introduces a large number of structural details (figure 1.1) [1].

Jordan [2] classified those details in 12 families, each of which consisted of numerous different configurations. By surveying approximately 86 ships, he created a database of failures originated at those details and tried to evaluate their in service performance. He found that many of the failures were created after the ship had encountered heavy weather conditions which caused structural overloading.

Most of the 12 families that Jordan identified include fillet welds. Some typical examples can be seen in figure 1.2. A significant percentage of the failures that he had recorded were associated with welding itself. Most of those failures were considered to be caused by fatigue. For this reason a considerable amount of research has been conducted,

concerning the performance of the fillet welds and the ship structural details under "normal" service loading, [3], [4], [5].

But "normal" service loads are not the only ones that a ship may encounter. It is possible for a ship structure to be subjected to extreme loading conditions caused by either heavy seas or accidents, such as collisions and groundings. The ship structural response to that loading is important because it may ultimately involve catastrophic failure modes, leading to the loss of a ship. Even non-catastrophic failures may become significant, if an oil spillage, caused by a moderate damage, results to an environmental disaster.

Under extreme loading conditions the ship structure may be subjected to large plastic deformations, which may be monotonic or even cyclic. Alternating plasticity may occur during awaiting and salvaging operations of a grounded ship [6] or during extremely heavy seas [7]. Also high strain rate effects should be considered as a result of the dynamic nature of the collision or grounding loading.

The scope of this work is to investigate the performance of the fillet welds on the ship structural details under such conditions, identify possible local failure modes and examine the importance of the weld defects.

Trying to understand the loads that are involved a literature survey has been conducted on the collision and grounding of ships and the dynamic response of the ship's structures. Additionally a review on the fracture and fatigue of ship structures has been performed, especially where fillet welds are involved. Particular attention was paid on the subject of very low cycle fatigue.

The main part of this investigation consists of a series of experiments, during which deep plastic deformation was applied to mild steel specimens. The specimens were appropriately designed to that represent the geometry of a structural detail. In most of the cases a second loading cycle was needed, in order to achieve fracture initiation. The Hi-Scope video microscope was used to record images during the experiment.

The information gathered during the experiments and the images obtained by the video microscope has been used for the qualitative and quantitative analysis of the fracture of the fillet welds under extreme loading conditions.

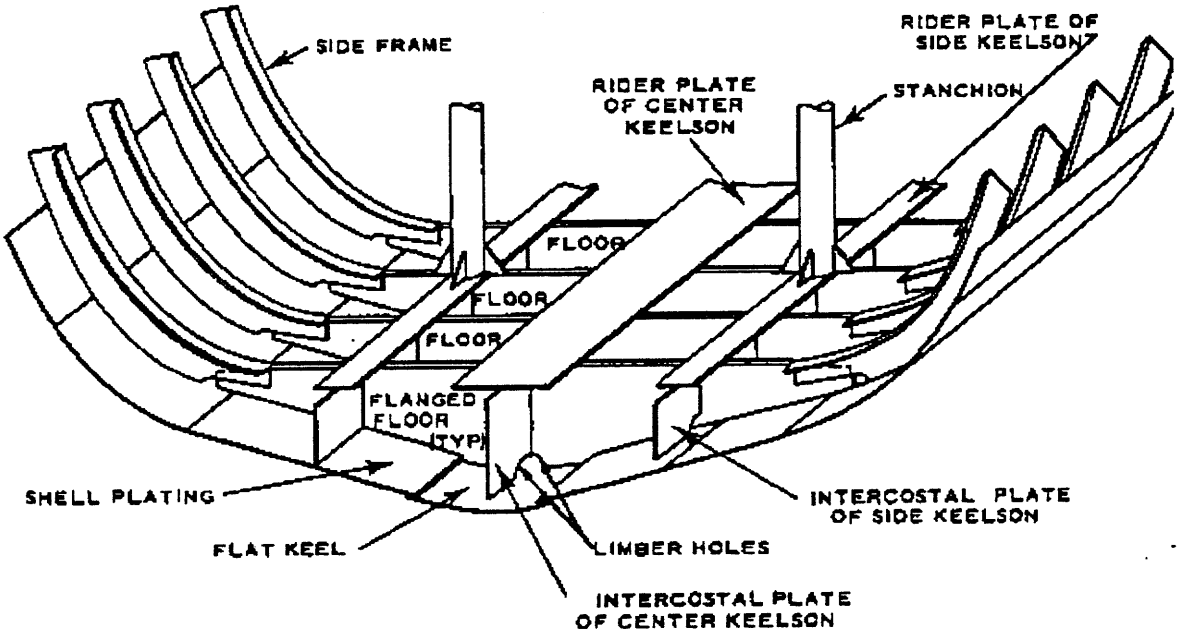

Figure 1.1 : Typical ship structural arrangement [1]

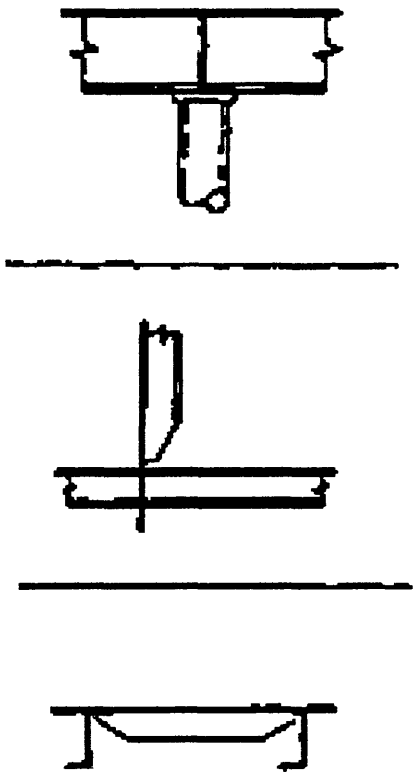

Figure 1.2: Ship structural details with fillet welds [2]

2. Background

2.1 Failure modes of ship structures

Catastrophic failure modes of ship structures represent the progressive structural failure which may finally lead to capsizing and sinking. Possible failure modes can be characterized according to cause, type and extent of damage, and consequences in terms of fatalities, pollution and economic losses. Component failures can be caused by ductile collapse, fracture to single overloads or incremental collapse, and low or high cycle fatigue from time varying loads. A component failure can develop into a progressive failure. Although only global failure modes may usually cause fatalities, moderate structural damages may result to significant pollution and economic losses. Identifying the possible failure modes of a ship structure is important because their analysis can give results that can be incorporated into the design, fabrication and operation of a ship.

For ship structures, which mainly consist of steel members, the basic type of failures and their subdivisions are as follows [8]:

1. Large local plasticity
2. Instability

   Bifurcation

Nonbifurcation

3. Fracture

Direct (tensile rupture)

Fatigue

Brittle

In practice a combination of the above occurs in ship structural members. Fracture is the worst failure mode in the case of marine vehicles, because it may lead to flooding and eventually sinking or to an environmental disaster from oil spilling.

2.2 Fracture mechanisms

Three principle fracture mechanisms can be generally identified: cleavage, nucleation and growth of voids and rupture [9].

2.2.1 Cleavage

Cleavage is usually considered to be a form of brittle fracture that is characterized by no apparent deformation in the vicinity of the crack. Usually propagation occurs along particular crystallographic planes, preferably those with the lowest packing density. In the case of body centered cubic (BCC) materials, cleavage occurs on {100} planes. Although

the cleavage crack propagates in a brittle manner, three different mechanisms for the crack nucleation can be identified. As a result three cleavage types can be identified.

For cleavage 1, pre-existing cracks are large enough to allow cracks to propagate at a stress lower than the yield stress at which activation of slip systems occurs and plasticity is very limited.

In cleavage 2 a localized plasticity occurs at the crack tip thus fracture is preceded by yielding. Cleavage nuclei are initiated by slip bands or twins which can be blocked by a grain boundary or a second phase particle. Therefore the length of the nucleated cracks is proportional to the grain size and consequently the fracture stress can be defined as

$$\sigma_f = \left(\frac{EG}{\pi d}\right)^{1/2}, \tag{2.1}$$

where E is Young's modulus and G is the toughness.

In cleavage 3 more extensive plastic flow (strains of about 1-10%) occurs, because of the low yield stress. General plasticity can nucleate cracks at grain boundaries, allow them to grow and, after a critical length, propagate as cleavage cracks.

Cleavage fracture is usually transgranular. However, impurities or imperfections at the grain boundaries can produce brittle intergranular fracture (BIF).

2.2.2 Void growth mechanism

A typical mode of ductile fracture is by void growth. The process consists of three stages: void nucleation, void growth and void coalescence [9].

Stress concentrations at hard particles can lead to local plasticity, which can result to interface decohesion or particle cracking that create an initial free surface. The nucleation of a void at a particle depends on how strongly the particle is bonded to the matrix.

After nucleation, voids grow around the particle by means of plastic strain and hydrostatic stress. Void growth is favored by high stress triaxiality conditions. Void coalescence is the final stage of void controlled ductile fracture. It is usually assumed that plasticity is localized between the voids. This localized deformation leads to final coalescence of voids and complete material separation.

Ductile fracture is normally transgranular. However, if the volume fraction of voids on grain boundaries is large, then the void growth can take place in an intergrannular manner. Under these circumstances ductile fracture is termed fibrous.

2.2.3 Rupture

Rupture is a further type of ductile fracture which is associated with plastic instability. In simple tension, plastic deformation proceeds uniformly along the entire length of the specimen until, at a critical point deformation becomes localized, forming a neck or a

shear band. With further extension the localized plastic zone will become more pronounced and eventually the cross-section will become zero. This instability induced rupture depends on the geometry of the specimen, strain hardening, strain rate sensitivity and softening of the material.

A prerequisite for pure rupture is the suppression of void nucleation and growth. Strain and strain-rate hardening oppose early local instability and enhance the possibility of rupture. On the other hand, the possibility of void nucleation and growth increases with the degree of the existing geometrical constraint [9].

2.2.4 Modes of fracture

The growth of cracks is categorized in terms of the orientation of the crack to an applied stress, and the type of applied stress. Refer to figure 2.1.

Mode I Cracks: They are the cracks which have a stress field perpendicular to their major axis, and as such are also termed "opening mode" cracks. Here, the displacement is perpendicular to the plane of the crack.

Mode II Cracks: Mode II or "sliding mode" cracks are characterized by a shear stress acting across the crack plane, parallel to its long axis. The displacement of the crack surfaces is in the plane of the crack and perpendicular to its leading edge, thereby sliding one surface of the crack along the other.

Mode III Cracks: Mode III or "tearing mode" crack is caused by out of plane shear stress. Crack surface displacements are in the plane of the crack and parallel to its leading edge.

2.3 Linear elastic fracture mechanics (LEFM)

For brittle materials LEFM can be used to describe fracture. The origins of fracture mechanics lie in Criffith's energy criterion for the catastrophic propagation of pre-existing cracks in a material. According to Griffith, a crack will propagate in a brittle material when the decrease in elastic strain energy is at least equal to the energy required to create the new crack surface.

The application of LEFM provides a full description of the stress and strain fields in the vicinity of the crack. Using linear elastic theory, it can be shown that the stresses at the region of the crack tip are described by

$$\sigma_{ij} = \frac{K}{(2\pi r)^{1/2}} f_{ij}(\theta), \tag{2.2}$$

where r and θ are the cylindrical polar coordinates of a point with respect to the crack tip and K is called the stress intensity factor. For a thin sheet containing an edge crack a (or equivalently an internal crack of $2a$), the stress intensity factor is given by

$$K = \sigma(\pi\alpha)^{1/2} f(\frac{\alpha}{W}), \tag{2.3}$$

where $f(\frac{\alpha}{W})$ is a dimensionless parameter whose value depends on the geometry of the specimen. Fracture occurs when K reaches a critical value K_C, which is called "critical stress intensity factor" or "fracture toughness". K_C depends on the material and the stress field around the crack tip. For the Mode I plane strain case, K_C is considered to take its lower value, K_{IC}, which can be considered material property. To ensure plane strain conditions the following restrictions apply: $\alpha = B = \frac{1}{2}W > 2.5(K_{IC} / \sigma_Y)^2$, where α is the crack length, B the thickness and W the width of the specimen [9], [10].

2.4 Elasto-plastic fracture mechanics (EPFM)

Linear elastic fracture mechanics can be usefully applied as long as the plastic zone is small compared to the crack size. This is usually the case in materials where fracture occurs at stresses appreciably below the yield stress and under conditions of plain strain. Under conditions of general yield the plastic zone spreads through the entire cracked region. The crack will propagate if the plastic strain at the crack tip exceeds a critical value. Assuming negligible strain hardening the stress at the crack tip hardly increases after general yield. Consequently, the fracture condition gets strain controlled. A measure for the plastic strain at the crack tip is the crack tip opening displacement (CTOD). Therefore, it can be argued that fracture occurs at the exceedance of a critical CTOD [10].

Using a model derived by Dugdale (1960), which assumes a crack with a tip plastic field replaced by a crack with an effective length and no plasticity, it turns out that the CTOD δ is given by

$$\delta = \frac{8\sigma_y \alpha}{\pi E} \ln \sec\left(\frac{\pi\sigma}{2\sigma_Y}\right). \tag{2.4}$$

Here α is the real crack length, σ_Y is the yield strength and σ is the applied stress [9]. Crack extension or propagation is assumed to occur when the CTOD reaches a critical value δ_C. In the case of LEFM the CTOD is given by

$$\delta = \frac{4}{\pi}\frac{K_I^{\,2}}{E\sigma_Y} \tag{2.5}$$

and δ_C is equivalent to K_{IC} [10].

An alternative method to characterize EPFM is by the use of the J-integral. This integral is defined as:

$$J = \int_\Gamma \left(W dy - T\frac{\partial u}{\partial x} ds\right) \tag{2.6}$$

with

$$W = W(x,y) = W(\varepsilon) = \int_0^\varepsilon \sigma_{ij} d\varepsilon_{ij}\,. \tag{2.7}$$

Γ is a closed contour followed counter clockwise (figure 2.2) in a stressed solid, T is the tension vector (traction) perpendicular to Γ in the outside direction, $T_i = \sigma_{ij} n_j$, u is the

displacement in the x-direction and ds is an element of Γ. W is the strain energy per unit volume. Rice has shown that the J-integral, as defined along a contour around a crack tip, is the change in potential energy for a virtual crack extension da:

$$J = -\frac{\partial V}{\partial a}, \tag{2.8}$$

where V is the potential energy. This relationship holds whether loading takes places under fixed displacement or constant load. For the first case eq. (2.8) can be written as

$$J = -\left(\frac{\partial V}{\partial a}\right)_u = -\int_0^P \left(\frac{\partial P}{\partial a}\right)_v dv \tag{2.9}$$

This case is shown diagramatically in figure 2.3. Crack initiation occurs when J reaches a critical value J_{IC}. At steady state stable crack growth is described by

$$J \geq J_R, \tag{2.10}$$

where J_R represents the fracture resistance of the material [10].

2.5 Dynamic fracture

There are fracture problems where time is an important variable. The most general case of dynamic fracture involves three features not included in LEFM and EPFM : inertia forces, rate-dependent material behavior, and reflected stress waves. Determining a fracture characterizing parameter, such as the stress intensity factor, for rapid loading can be very

difficult. For the case where the size of the plastic zone around the crack tip is small a Mode I near tip stress field can be given by

$$\sigma_{ij} = \frac{K_I(t)}{(2\pi r)^{1/2}} f_{ij}(\theta, V), \tag{2.11}$$

where (t) denotes function of time and V the crack speed. From recent work done by Nakamura et al. it was found that there is a transition time, above which inertia and stress waves effects may be neglected and a quasistatic approach may be applicable [11].

If the effects of inertia and reflected stress waves can be ignored, the feature that is left is the rate-dependent material response. High strain rates tend to elevate the flow stress of that material. The effect of the loading rate on the fracture toughness of a material depends on the failure mechanism. If failure occurs by cleavage, which is stress controlled, the fracture toughness decreases as the strain rate increases. If the failure is strain controlled, the higher flow stress results to larger energy absorption, which is translated to increased fracture resistance [11].

Drar [12] proposed a model that predicts the fracture toughness of plain carbon steels for different temperatures and strain rates. According to Drar, the increase in loading rate shifts the quasistatic transition curve to higher temperatures, reduces the cleavage fracture toughness both on the lower shelf and in the temperature-dependent regime and increases the crack growth resistance. The main difference between impact and slowly applied load can be explained by the greater volume of metal deforming at low rates. However, the sensitivity to strain rates varies for different materials, being largest for BCC

metals and smallest for FCC metals. The rate sensitivity arises from the fact that a high rates there is not enough time for the thermal energy caused by the plastic deformation to assist the dislocation movement.

2.6 Fatigue

If a structural component is subjected to repeated stress cycles, it may fail at stresses well below the tensile strength and often below the yield strength of the material. As the applied stress increases the number of cycles to failure decreases and vice versa. This failure process, which is termed fatigue, is considered responsible for the 50 to 90 percent of all mechanical failures [13].

Fatigue is considered to occur as a result of plastic deformation that takes place at the microscopic and macroscopic level of the material. This reduces its ability to withstand stress and initiates cracks. The cracks, initially microscopic, propagate, leading to a (monotonic) final fracture. The fatigue process is strongly influenced by microscopic and macroscopic notches, surface characteristics and environment.

2.6.1 High cycle fatigue

Fatigue is considered to be high-cycle, if failure occurs at a number of cycles larger than 10^3. Otherwise the process is considered low-cycle high stress fatigue. High-cycle fatigue can not be avoided because it usually occurs under service loading. This has led to

considerable research on the subject, in order to get able to predict the life of structural components. The currently used life assessment methods are based on the cumulative damage (Miner's rule) and the LEFM approach (Paris law).

Miner's rule is based on the tests of uncracked coupons which are subjected to cyclic loading at different stress amplitudes. Their life is determined as the cycles needed for crack initiation, which is defined as the failure condition. Those cycles are plotted against the corresponding stress amplitude and the famous S-N curves are created. Each curve can be described by a relationship of the form

$$\log(S) = A + B\log(N), \tag{2.12}$$

where S is a stress amplitude parameter and N the number of cycles to failures. Miner's rule states that, in the case of a loading spectrum, failure occurs when

$$\sum_{i=1}^{B} \frac{n_i}{N_i} = 1, \tag{2.13}$$

where B are the number of stress blocks, n_i the number of stress cycles at block i and N_i the number of cycles to failure at constant stress range S_i.

In the LEFM approach the stress range is expressed as a stress intensity factor range ΔK, which simultaneously takes into account geometry and current crack size. The crack growth rate is given by

$$\frac{d\alpha}{dN} = C(\Delta K)^m, \tag{2.14}$$

where α is the crack depth and C and m are parameters that come from fracture mechanics. Failure occurs when the crack length reaches a critical value which corresponds to the K_C of the component under monotonic loading.

Those approaches are applicable when the applied stresses are still in the elastic range and therefore cannot be considered under extreme loading. On the other hand it must be noted that small cracks that exist in a structure due to fatigue can affect its residual resistance to overloading.

2.6.2 Low cycle fatigue

In the case of low cycle fatigue extensive plastic deformation occurs mainly in the notch area. However, this area remains contained in an elastic manner, both by the less deformed adjacent areas and by the elastic strain component in the strongly plastically deformed area itself. Quantitatively, this type of fatigue is also described by a cumulative damage law [13]. Since plastic deformation is involved the process has been considered strain controlled. Therefore, for the evaluation of low-cycle fatigue, strain-life curves have been plotted similar to the S-N curves of the high-cycle fatigue. Failure criteria for strain-lives curves have not been consistently defined. Failure may be considered a small detectable crack, a certain percentage decrease in load amplitude, or fracture.

The total strain amplitude involved in low-cycle fatigue can be resolved to an elastic and plastic part,

$$\frac{\Delta\varepsilon}{2} = \frac{\Delta\varepsilon_e}{2} + \frac{\Delta\varepsilon_p}{2} \tag{2.15}$$

where $\Delta\varepsilon/2$ is the total strain amplitude, $\Delta\varepsilon_e/2$ the elastic strain amplitude and $\Delta\varepsilon_p/2$ the plastic strain amplitude. For the elastic part Basquin has proposed the relationship

$$\frac{\Delta\varepsilon_e}{2} = \frac{\sigma_f'}{E}(2N)^b \tag{2.16}$$

where σ_f' is a fatigue strength coefficient and b is fatigue strength exponent.

For the plastic part the Manson-Coffin relationship has been proposed which is given by

$$\frac{\Delta\varepsilon_p}{2} = \varepsilon_f'(2N)^c \tag{2.17}$$

where ε_f' is a fatigue ductility coefficient and c is a fatigue ductility exponent. Using a universal slopes method Manson has obtained a modified relationship where

$$\Delta\varepsilon = 3.5\frac{\sigma_{UTS}}{E}(N)^{-0.12} + \varepsilon_f^{0.6}(N)^{-0.6} \tag{2.18}$$

σ_{UTS}, E, and ε_f are all obtained from a monotonic tensile test.

2.6.3 Very low cycle fatigue

Very low cycle fatigue is referred to the case when extensive alternating plasticity occurs. This type of failure is considered important for the case of the deferred damage on a grounded ship [6] or at extreme weather conditions [7]. Since the plastic zone is not contained anymore, low-cycle fatigue considerations cannot be applied without being reevaluated.

Extremely low cycle fatigue is accompanied by such large deformations that by themselves correspond to a failure mode of the structure. This means that very low cycle fatigue is applied on components that, literally, have already failed. Perhaps that is the reason why little investigation has been conducted on that subject. On the other hand there are situations where the main issue is fracture rather than plastic deformation. This can be the case of a marine vehicle where localized extensive plasticity may not be as damaging as a local fracture, that may cause flooding of an internal compartment or (in the tanker case) spilling of oil in the sea.

In the few articles found in the literature it is mainly concluded that extremely low cycle fatigue is a process more similar to the monotonic ductile fracture than to fatigue. It is a bulk rather than a surface process and fracture initiates internally from second phase particles or inclusions. The validity of a cumulative damage approach has been investigated with good results and some modified Manson-Coffin type laws have been proposed. A

complete list of related articles with a summary of their content is submitted in Appendix A [7],[14]-[22].

2.7 Fillet welds

Fillet welds represent about 75% of the welded joints used in a typical hull construction [23]. An "anatomic" cross section of a fillet weld can be seen in figure 2.4. Loading on the fillet welds is generally applied in two ways: in longitudinal shear or in transverse shear as shown in figure 2.5. In the longitudinal shear case, the weld needs only to develop the ultimate shear strength of the intercostal member, whereas in the transverse shear case, the weld must develop the ultimate tensile strength of the intercostal member [24].

Considering the importance of fillet welds, the classification societies have introduced specific standards that should be met during matine construction. Current design standards for fillet welds ensure the safe operation of a ship under normal service conditions by requiring a fillet weld stronger than the structural material. They also establish some limits with respect to the magnitude of the weld defects that can be allowed for a specific structure, according to its importance [24]. Although some defects may not be very important under "normal" loading, they may significantly reduce the ability of the structure to withstand extreme conditions without fracture.

At such conditions two fracture modes have been identified from data taken from previous accidents. The first one is peeling fracture (tearing) of the fillet weld and the second one fracture of the base plate at the toe of the fillet weld [6]. Those failure modes can be seen in figure 2.6.

2.7.1 Fillet weld defects

Through the construction of a ship, maintaining a fillet weld that would exactly represent the ideal design standards is impossible. Small defects are usually created that reduce the strength of the welded joint. This happens because their presence not only reduces the sectional areas but also creates stress concentrations.

The defects that may be identified in a fillet weld and can be seen in Figure 2.7 are [6], [25]:

- Porosity
- Inclusions
- Incomplete fusion
- Inadequate penetration
- Concavity-convexity
- Undercut
- Cracks

- Arc strikes

The extent to which weld defects affect the structural strength depends on their nature and extent, the material properties and the type of the loading to which the structure is subjected.

2.7.2 Tearing of fillet welds

Using slip line field theory the plastic failure path of a two-sided fillet weld may be predicted. Slip lines represent the orientations of maximum shear in a stress field, along which deformation is expected to occur. Considering a T-joint in tension and using the upper bound theorem a limit transverse load that will ensure the weld deformation can be calculated.

Such solutions have been obtained for homogeneous, non-hardening fillet welds with arbitrary crack tips and weld angle [26]. For the special case of the 45^o weld angle the limit load per unit length is given by

$$P_L = 2kd \tag{2.19}$$

where k is the shear strength of the weld and d is the minimum leg length (figure 2.4). In fracture mechanics, k is approximated by: $k = TS / \sqrt{3}$, where TS is the tensile strength of the weld metal. Experimental results have shown that a value of $k = 0.75 \cdot TS$ gives a better approximation in the case of the fillet welds, reflecting the effect of plastic instability absence [24].

The tearing resistance of a fillet weld can be described by the work required by a transverse load to cause separation of the web from the base plate, normalized per unit length of the fractured weld. Assuming negligible elasticity effects, the ideal work per unit length can be estimated as

$$R_{ideal} \approx 1/2\, P_L d = kd^2 \tag{2.20}$$

This work is ideal since, besides plastic sliding, fracture also takes place and slip occurs at an angle to the vertical. Assuming that cracking initiates at a displacement u_i and fracture is completed at a displacement u_f, the fracture work per unit length ("tearing resistance") can be approximated by

$$R_C = P_L(u_i + u_f)/2 \equiv P_L u_C \tag{2.21}$$

where u_C is defined as an effective critical displacement (figure 2.8) [26].

Regarding the peeling fracture of a double sided fillet weld the control volume of figure 2.9 can be considered. Assuming that a critical bending moment M_C is applied, resulting to a critical curvature κ_C, then as an element material moves by δL the slope changes by $\delta\theta$. The work that the moment does is $M_C\delta\theta = M_C\kappa_C\delta L$. Assuming that there is little interaction between the work to bend the plate and that to tear the weld then [26]

Total work = Plate bending work + Weld tearing work,

$$M_C\kappa_C\delta L = \left(\int_0^{\kappa_C} M d\kappa\right)\delta L + R_C\delta L\ ;\ M_C\kappa_C = \int_0^{\kappa_C} M d\kappa + R_C\ . \tag{2.22}$$

From this the tearing resistance can be found

$$R_C = M_C\kappa_C - \int_0^{\kappa_C} M d\kappa = \int_0^{M_C} \kappa dM \tag{2.23}$$

Peeling fracture has been investigated on the idea of an elastic-perfectly plastic beam glued on a rigid block. Chang et al. [27] consider an end force loaded beam (figure 2.10), whereas Atkins and Mai [28] assume an end-couple loading (Figure 2.11). Both of those works result to closed form solutions of the fracture work which can be adapted to the case of peeling fracture.

The tearing resistance of a fillet weld for an end loaded beam is

$$R = \left[\begin{array}{l} \dfrac{\sqrt{2}(1-\nu^2)b^{1/2}\sigma_Y^{3/2}Pl}{3E\sqrt{6\sigma_Y bh^2 - 3Pl}} - \dfrac{\sqrt{2}(1+8\nu^2)b^{3/2}\sigma_Y^{5/2}h^2}{6E\sqrt{6\sigma_Y bh^2 - 3Pl}} - \\ \\ -\dfrac{\sqrt{2}(11+16\nu^2)}{36E}\sqrt{6\sigma_Y bh^2 - 3Pl}\,b^{1/2}\sigma_Y^{3/2} + \dfrac{(1+2\nu^2)b\sigma_Y^2 h}{E} \end{array} \right], \tag{2.24}$$

where P is the end load, l is the length of the beam plus the crack length, b is the half beam width, h is the half beam height and σ_Y, E and ν the flow stress (yield strength), Young modulus and elastic Poisson's ratio of the beam material. The formula is valid when

$$2\sigma_Y bh^2 > Pl \geq \frac{4}{3}\sigma_Y bh^2 \tag{2.25}$$

For the moment loaded case, which actually corresponds to that described also by McClintock [26], fracture occurs under a critical moment

$$M_C = \left(Bh^2\sigma_Y\right)\left[1-\frac{3}{4}\left(1-RE/{\sigma_Y}^2h\right)^2\right] \tag{2.26}$$

so

$$R_C = \left(Bh{\sigma_Y}^2/E\right)\left[1-\sqrt{\frac{4}{3}\left(1-M_C/B\sigma_Y h^2\right)}\right], \tag{2.27}$$

where B is the full beam width. This formula is valid for

$$M_C \le B\sigma_Y h^2 = M_L . \tag{2.28}$$

Here M_L represents a limit bending moment where plastic collapse of the base plate precedes fracture.

2.7.3 Fracture at the fillet weld toe

The Japan Welding Engineering Society (JWES) standard WES2805 has been widely used to evaluate the fracture safety of structures. It is based on elastic-plastic fracture mechanics (CTOD criterion), because most brittle fracture incidents may occur from a defect at a structural stress concentration where plastic zone is generally greater than the defect size. This approach has been used for the fracture strength assessment of the fillet welds and its validity has been accepted [29],[30]. The condition for fracture is expressed by,

$$\delta \ge \delta_C \tag{2.29}$$

where, δ is the applied CTOD and δ_C is the fracture toughness of the material. δ_C can be determined by a three-point CTOD test in accordance to existing testing standards.

In this approach, the applied CTOD is taken from a CTOD design curve which is formulated by

$$\delta = \begin{cases} 2e_Y \bar{a}(e/e_Y)^2 & : \ e/e_Y \le 1.0 \\ e_Y \bar{\alpha}(3.5e/e_Y - 1.5) & : \ e/e_Y \ge 1.0 \end{cases} \tag{2.30}$$

where e is the applied local strain, e_Y is the yield strain and $\bar{\alpha}$ is LEFM-based equivalent through-thickness crack flaw.

In eq. (2.30) an "average local strain" $\tilde{e}$ is defined and used as applied strain. $\tilde{e}$ is the strain value averaged over the cracked area and is given by

$$\tilde{e} = \tilde{K}_\varepsilon e_{nom} \tag{2.31}$$

where $\tilde{K}_\varepsilon$ is the average local strain concentration factor. In the case of $\sigma_{net} < \sigma_Y$ the nominal strain is given by

$$e_{nom} = \sigma_g / E \tag{2.32}$$

where σ_g is the gross stress at the crack area and σ_{net} is the stress without considering the crack. Assuming a power hardening stress strain relation $\tilde{\sigma} = F\tilde{e}^n$ the nominal strain e_{nom} for the case that $\sigma_{net} > \sigma_Y$, is given by

$$\tilde{\sigma} = F\tilde{e}^n \exp(-\tilde{e}), \qquad \tilde{e} = \ln(1 + e_{nom}) \tag{2.33}$$

The strain hardening exponent n can be expressed as a function of the yield stress of the material σ_Y:

$$n = 0.121\ln(1392/\sigma_Y), \qquad \sigma_Y\text{: MPa} \tag{2.34}$$

The average local strain concentration factor $\tilde{K}_\varepsilon$ can be estimated from the average elastic stress concentration factor

$$\tilde{K}_\varepsilon = \begin{cases} \tilde{K}_t & \tilde{K}_t\sigma_g \le \sigma_Y \\ \tilde{K}_t + A(\sigma_g/1.125\sigma_Y - 1/\tilde{K}_t) & \sigma_{net} \le \sigma_Y \le \tilde{K}_t\sigma_g \\ \tilde{K}_t^{\,2/(1+n)} & \sigma_{net} \ge \sigma_Y \end{cases} \tag{2.35}$$

where $A = \alpha(\tilde{K}_t^{\,2/(1+n)} - \tilde{K}_t)/(1-\alpha/\tilde{K}_t)$ and $\alpha = \sigma_{net}(\text{no crack})/\sigma_g$. The average stress concentration factor $\tilde{K}_t$ is the value of the elastic stress concentration factor K_t averaged over the crack area, and it can be estimated by elastic stress analysis.

That kind of analysis has been performed for two-dimensional T-joints and empirical formulas have been constructed, in order to evaluate stress concentration factors that they could be used for brittle fracture and fatigue assessment [31], [32]. Considering the geometry in figure 2.11 the stress concentration factor for bending is given by

$$K_t = 1 + 0.5121 \cdot \alpha^{0.572}\left(\frac{t}{\rho}\right)^{0.469} \tag{2.36}$$

for $\frac{\pi}{6} \le \alpha \le \frac{\pi}{3}$ and $\frac{1}{50} \le \frac{\rho}{t} \le \frac{1}{15}$ [32].

The effect of a defect such as an undercut is to magnify K_t. The amount of this magnification for an undercut with 1 mm radius of curvature at the toe of a 45^o weld has been calculated by Onozuka et al. for various undercut depths [31]. It was found that the stress concentration factor increases greatly until the depth of 0.1 mm, slower until the 0.3 mm and gradually over 0.3 mm. The stress concentrations that they calculated for a 10 mm thick beam under bending were about 2.63 at depth=0.1mm, 3.0 at depth=0.3 mm and 3.58 at depth=1 mm. Without the undercut, the stress concentration can be calculated from eq. (2.36) and is equal to 2.58. Therefore, it can be said that the existence of an undercut with 1 mm depth magnifies the stress concentration by a factor of 1.39.

2.8 Ship structural steels

Ship steel is classified into four grades A, B, D and E, differentiated by deoxidation practice, heat treatment, chemical treatment and Charpy V notch energy, which corresponds to a fracture toughness requirement. Although grade A steel has no toughness requirement is the most commonly used ship-building material.

Under "normal" service loading, modern mild steel has adequate toughness, but it is questionable whether it will perform in a ductile or brittle manner under high strain rates and relatively low temperatures [33]. In November 1986 the Kowloon Bridge grounded off the South West coast of Ireland and broke amidships. By examining a piece of the wreckage

it was found that at high loading rate (3 ms to yield) cleavage jumps occurred even at 30°C [34].

The primary effect of changing the loading rate is to change the mechanical properties of steel. According to Shoemaker [35] collision loading times can be of the order of a millisecond or less, making them comparable to impact loading. In most cases the extremely small loading times will be confined to very local areas of a ship, since stress wave transmission will be dampened by the massive structure. Once an appropriate loading rate has been established for a specific ship detail, determination of the fracture behavior of the steel can be obtained provided the mechanical properties at the same loading rate and temperature are used. Usually an increase in the loading rate will cause embrittlement by elevating the yield strength and decreasing the plastic zone size at stress concentrations, imperfections, actual cracks or, more often, in welds.

Sumpter and Caudrey have come up with the conclusion that grade A steel is unsuitable for use in ship hulls. They propose testing of welded pre-cracked specimens at temperatures between -40°C and $+20^{\circ}$C and loading rates between 10 and 50000 MPa $m^{1/2}/s$. They conclude that a minimum fracture toughness requirement for ship steels should be 125 MPa $m^{1/2}$ at a loading rate of 10000 MPa $m^{1/2}/s$ and a temperature of 0°C. An equivalent δ_C is 0.15 mm [36].

An alternative way to characterize ship hull steels, is the dynamic fracture toughness K_D. This value, which may be considered a material property, has been calculated by

various researchers and used to evaluate the crack propagation and arrest of stiffened ship structures [37], [38].

2.9 Ship structural loads

2.9.1 General

Loads on a ship can be classified by either the level of structure at which they act or according to how they vary with time. Using the first classification ship loads can be distinguished to [8]:

- Hull girder loads
- Hull module loads
- Principal member loads
- Local loads
- Combination of the above

Using the second classification we have:

- Static loads
- Slowly varying loads
- Rapidly varying loads

The second classifying method is the most important one because it defines the kind of the analysis which must be used to investigate the behavior of the structure under the corresponding load. These types of analysis are respectively:

- Static
- Quasi-static
- Dynamic

A quasi-static analysis is simply a static analysis in which the motions are estimated and their effect on the structure is accounted for by including some inertia forces. Therefore static and quasi-static analysis can be considered together [8].

The static loads consist of all the "stillwater" loads such as weights and buoyancy. Dry-docking and thermal loads are also in this category. Their calculation and incorporation in the design process is the most easy and straightforward.

The slowly varying loads include the pressure distribution on the hull under the combined wave and ship motion, the sloshing of the liquid cargoes and the green seas on the deck. Also the inertia loads from ship structures on their attachment points, the launching and berthing loads and the ice-breaking loads are considered in this category.

Rapidly varying loads can be considered the forced mechanical vibrations and the pressure pulses from the propeller, ice impact, collision or grounding loads , under water explosion loads and slamming. Slamming can be divided in bottom slamming and bow flare slamming. Bottom slamming occurs when the ship pitching causes emergence and impact

reentry of her bottom. Bow flare slamming is the plunging of the upper flared portion of the bow deeper into the water. Both phenomena result to rapid increase in local pressure in the bow area which can overload the structure both locally and globally.

Most of the loads mentioned above are normal service loads which are taken into account during the structural response analysis. Strength analysis and fatigue analysis can be made in either a deterministic or probabilistic way, using appropriate load spectra . Consequently design optimization and material improvement made it very unusual for a catastrophic failure to occur under normal operational conditions. Most failures come from extreme loading conditions resulted from extremely heavy seas, collisions and groundings.

2.9.2 Past studies on collision, grounding and extreme loading

A large number of articles have been published on various aspects of the structural strength of ships during collisions since Minorsky's [39] pioneering paper on the protection of nuclear powered ships. Less attention had been paid on the grounding problem until recently when the grounding of the Exxon Valdez into Prince William sound resulted to a spillage of 11 million gallons of oil. The public pressure and the cost, both economic and environmental, associated with this incident, have forced a significant research effort on the ship structural response during grounding.

Jones in 1979 conducted a literature survey on the collision and grounding protection of ships [40]. In that report the problem and the approaches that are taken by various researchers is described giving special emphasis on the results obtained by the

various research activities. Jones proposes a classification of the collisions to major and minor ones, according to whether fracture has occurred or not, respectively. He argues that a protection scheme, either of resistance or energy absorption type for an oil tanker might be feasible only for minor collision protection. Trying to investigate the validity of scale testing for collisions and groundings, he has found references according to which complete scaling is not possible considering the non-linear effects of the inelastic material behavior, fracture and strain rate sensitivity. Full scale tests have proved that the failures modes involved in a collision are the same whether the process takes place statically or dynamically, with greater energy absorption at the dynamic case.

Complementary to Jones' work is that of Mater and Giannotti [41] [42], whose scope was the critical evaluation of the existing low-energy collision studies and the determination, in each case, of their validity and range of application. Also all the associated experiments were checked for relevance and completeness. The ultimate objective was to determine whether or not one or a combination of those methods could provide a design methodology for minimizing collision damage. In their report the existing damage assessment theories in comparison with experiments are presented but they clearly state the assumptions that were used and their limitations.

A correlation between the damage predictions and observations on an actual grounding of a membrane tanker indicate satisfactory damage predictions by the Minorsky and Vauhan methodologies [43]. Those methodologies are semiembirical and use the damaged material volume in order to characterize the response of the structure. Although

they work well for major collisions and groundings they are inadequate at the low energy range.

Jones [44] examined the static and dynamic plastic behavior of plates and beams, trying to estimate the ship's structural performance in case of collision, grounding and slamming or ice damage. An application of the plastic design on a longitudinally framed oil tanker structure was performed by McDermott [45] for the case where no rupture occurs. The failure modes identified in this model are: bending and stiffener buckling of the stiffened hull plating followed by membrane stretching and web frame failures up to hull rupture. A similar model considering more failure modes for the grounding case was introduced by Wierzbicki et al. [46].

Egge and Bockenhauer [47] have proposed the classification of the ships according to their resistance against collision and the use of standardized collision cases, solved by computer, that could be correlated to the classified ships.

Pedersen [48] has analyzed the effect of grounding on the hull girder strength of the ship. He has found that the longitudinal strength of ship hulls may not be sufficient to withstand a severe grounding causing total structural failure, instead of local at the grounding area.

Examining the load rate effect on structures Jones [49] identified three failure modes of a beam clamped at the ends. For non strain hardening materials at low rate there is only plastic deformation. at intermediate rate there is tearing close to the supports. At high rate shear failure at the supports occurs. For strain-rate sensitive mild steel shear failures were

dominant under impact loading at midspan, whereas tensile tearing occurred when the loading was applied near a support.

Duffey [50] has extended that work to shell structures concluding that an equivalent plastic strain failure criterion is inadequate for the case of the shear failure near the supports (hard points). Alternatively, a hard point shear failure criterion is suggested. He has also found that as the stiffness of the hard points decreases, the critical velocity for shear failure near the supports increases.

Gifford and Dally have proposed a new two-parameter criterion for the fracture resistance of metals, which is based on simple formulation [51]. Their formulation predicts a critical limit for crack depth below which failure will take place by crack extension, regardless of load. They also show that under combined tension and bending, unstable crack growth starts at a small crack depth and arrests and a larger one concluding that failure occurs by other mechanism than unstable crack growth.

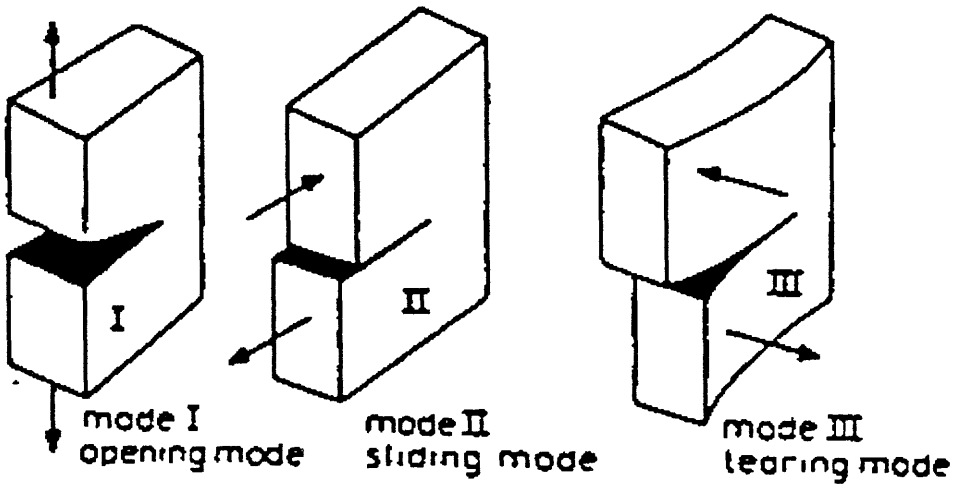

Figure 2.1 : The three modes of fracture [9]

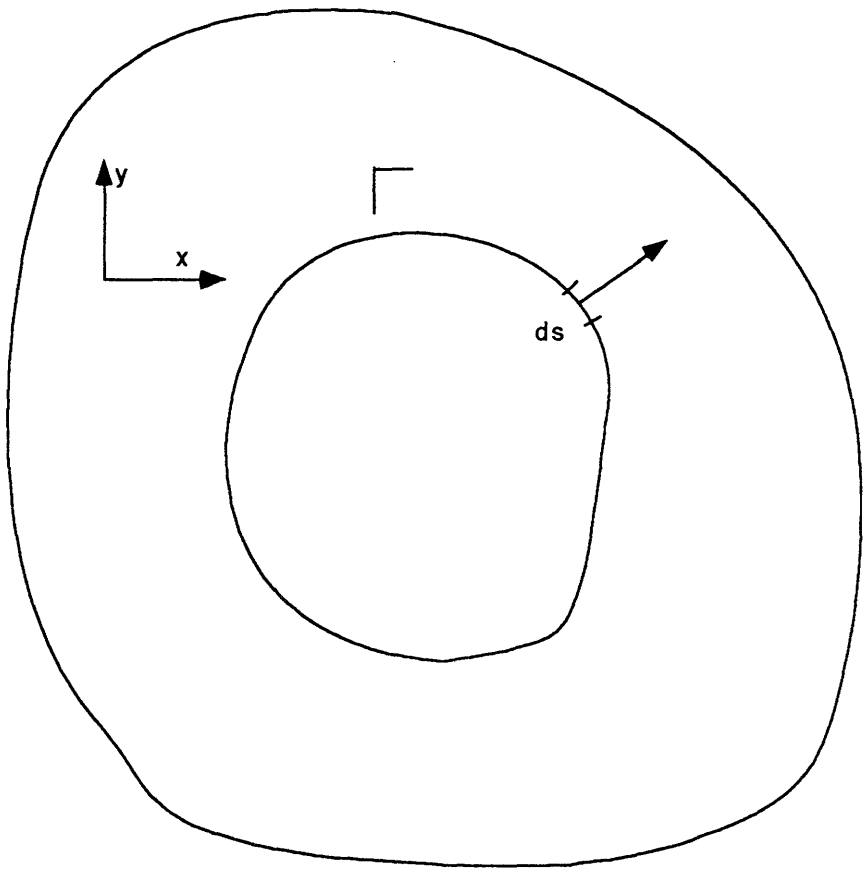

Figure 2.2 : Definition of J-integral

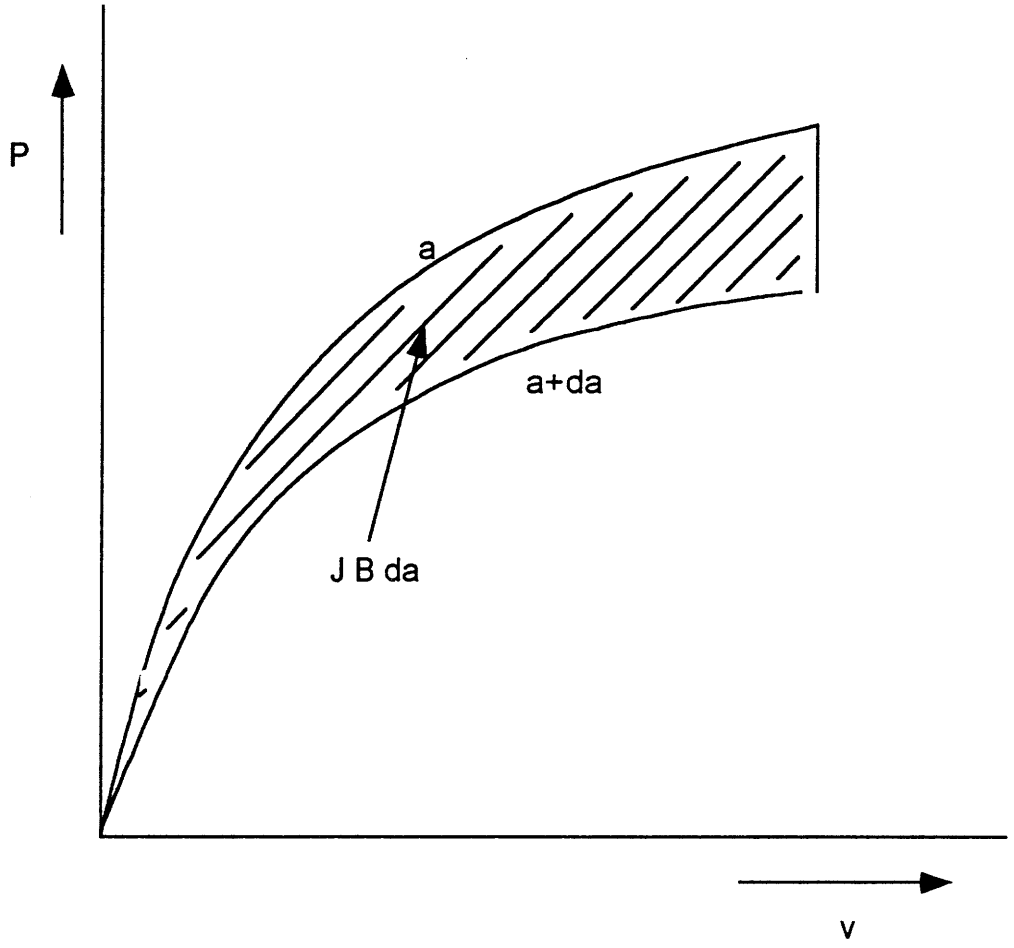

Figure 3.3 : Load displacement diagram for cracked body of non-linear elastic material

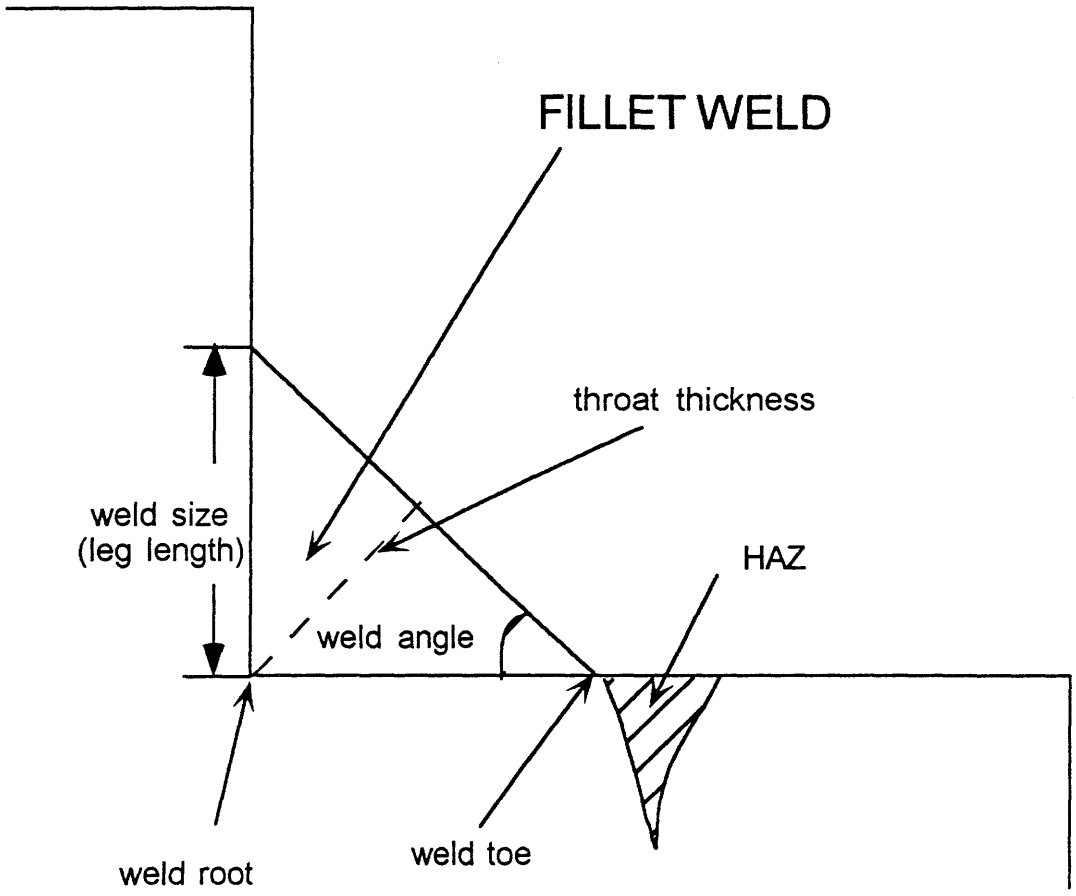

Figure 2.4 : Geometry and definitions of fillet welds

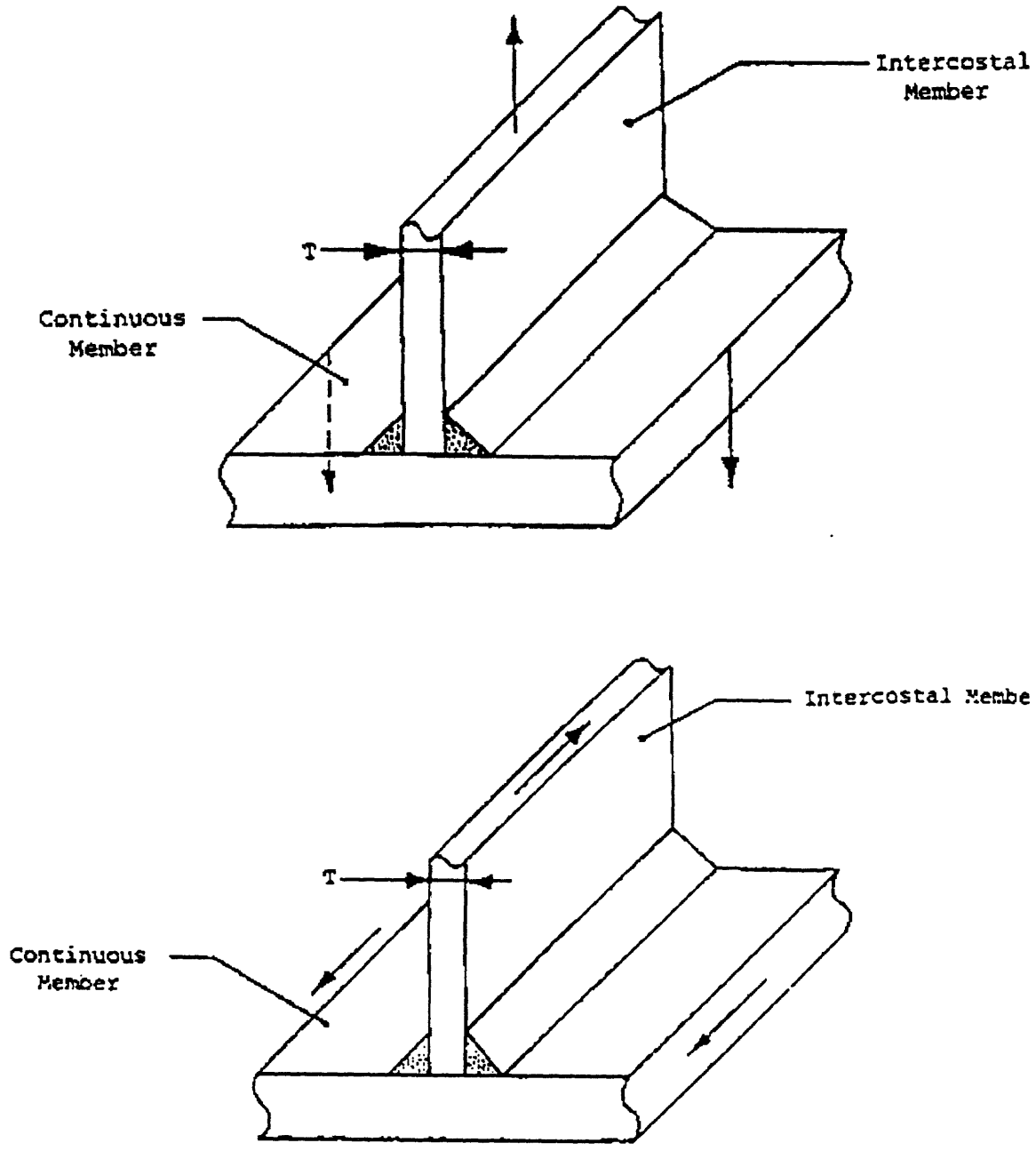

Figure 2.5 : Fillet weld loading

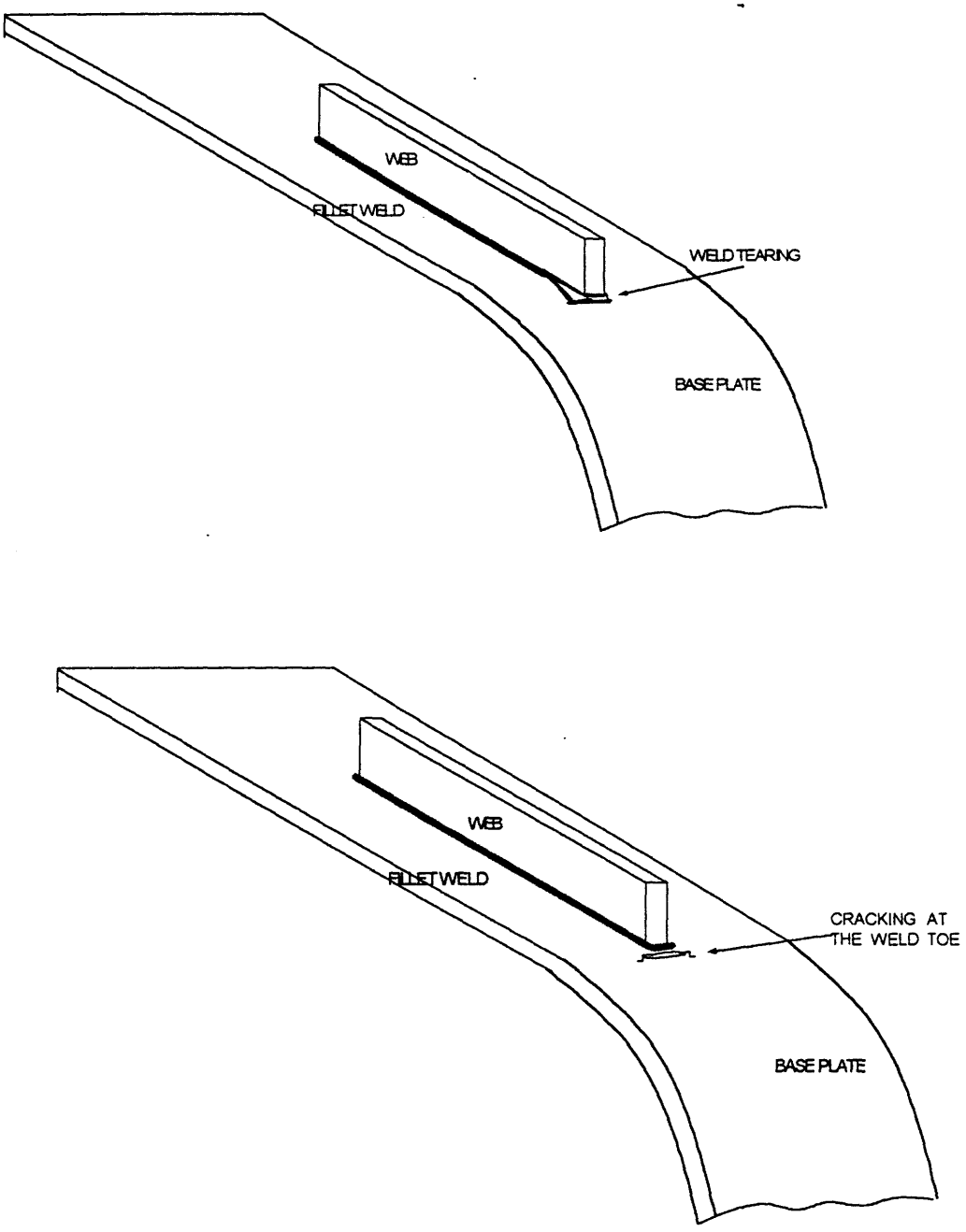

Figure 2.6 : Fracture modes of fillet welds

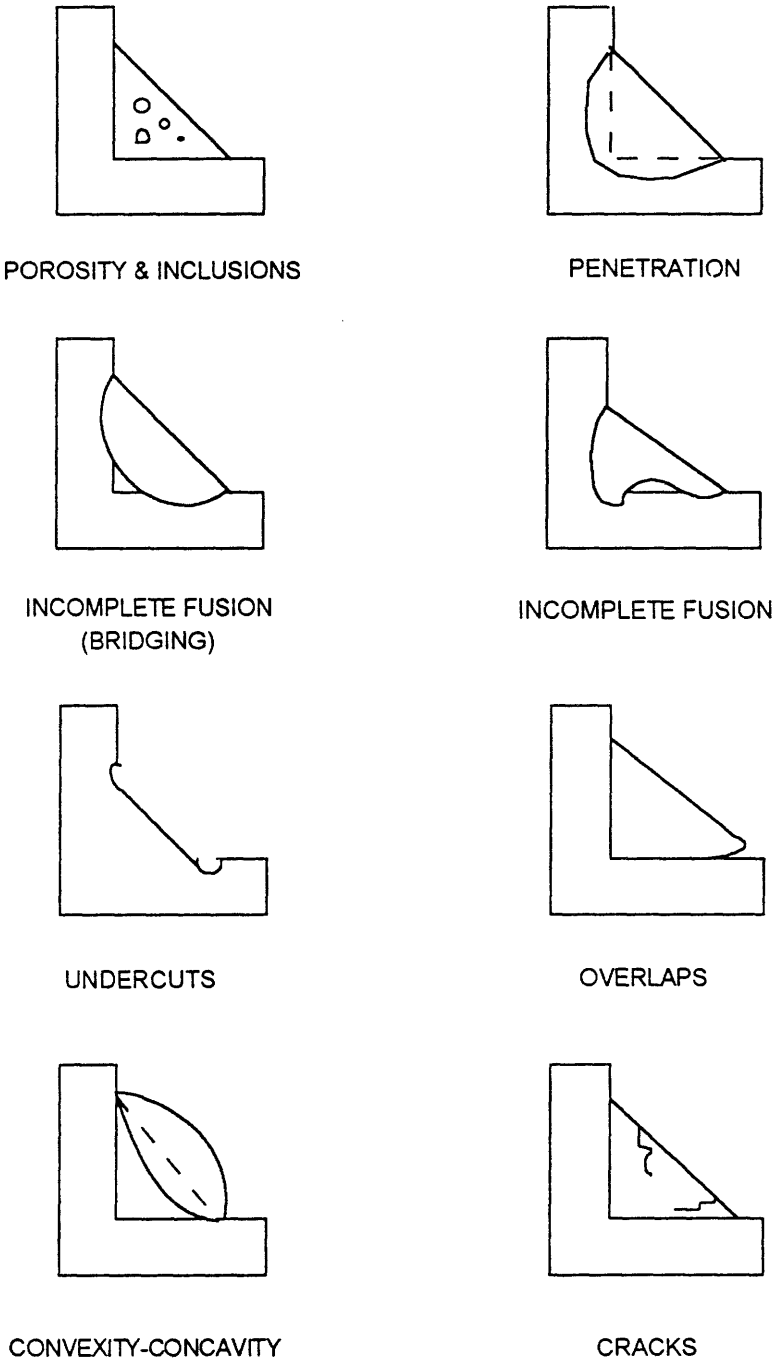

Figure 2.7 : Defects of fillet welds

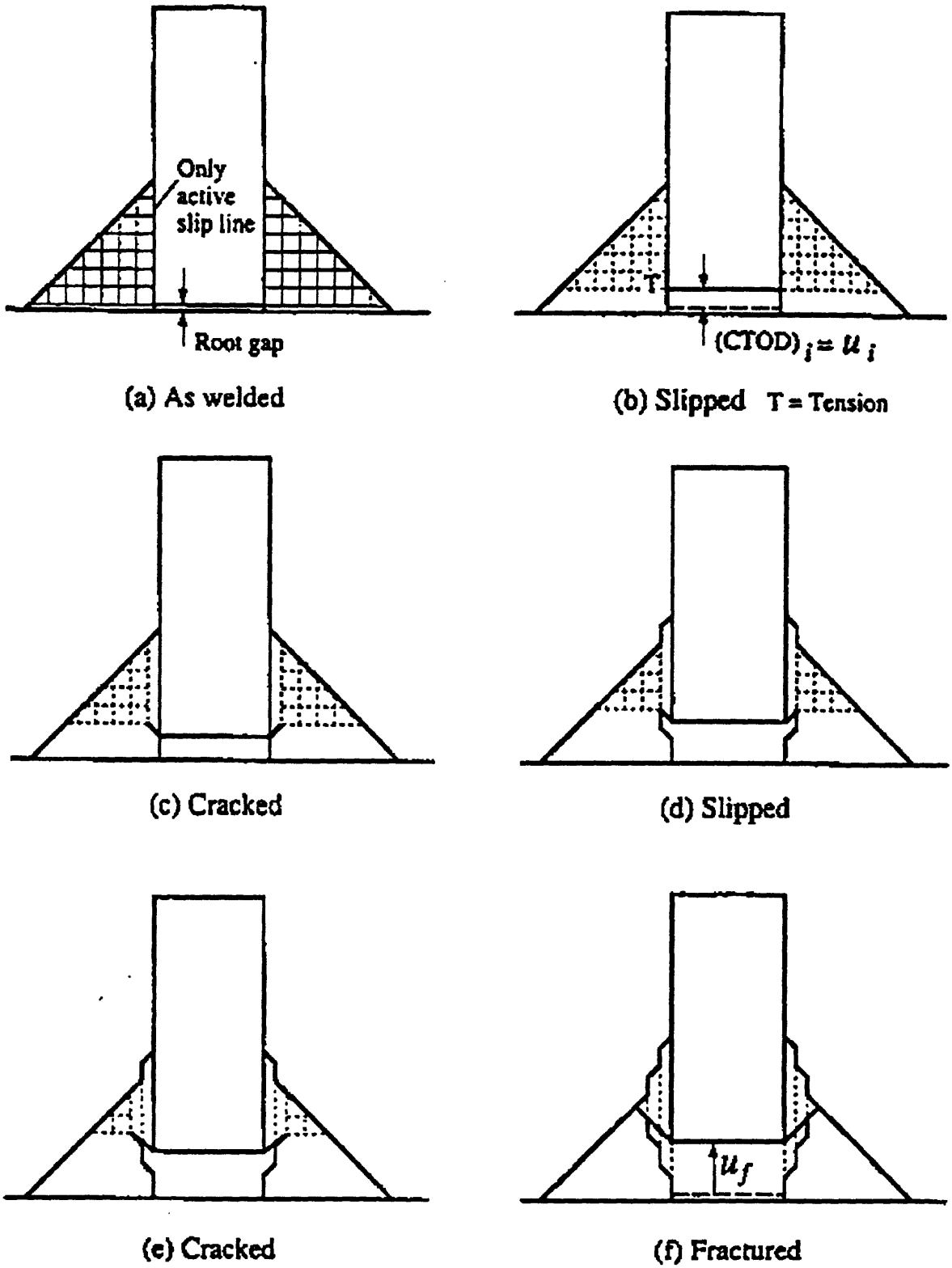

Figure 2.8 : Crack tip opening displacement for initiation u_i and alternating cracking and sliding off during crack growth to final separation at u_f [26].

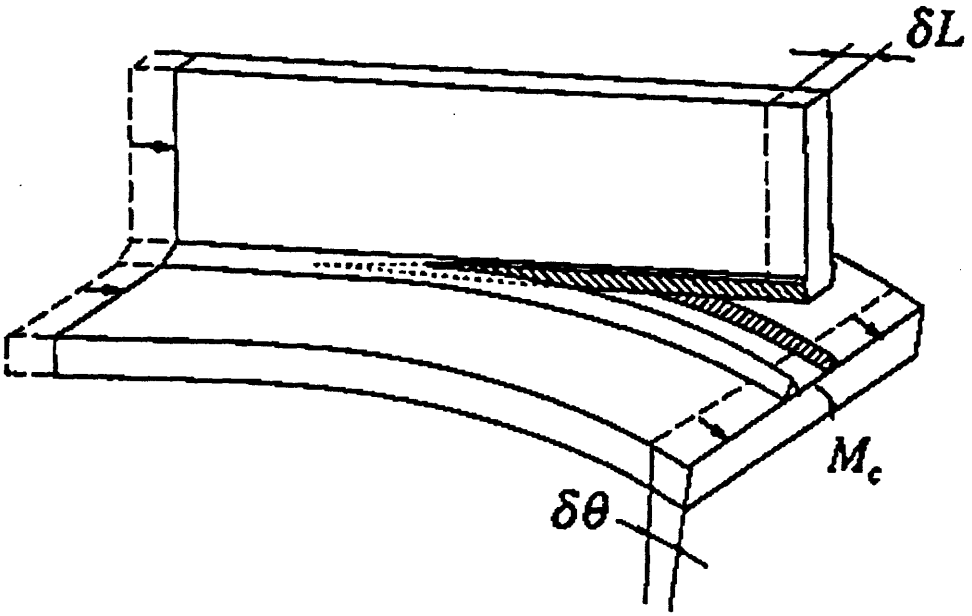

$$M_c(\delta\theta = \kappa_c \cdot \delta L = \delta L / \rho_c)$$

Total work = Plate bending work + Weld tearing work (little interaction)

$$M_c \kappa_c \delta L = (\int_0^{\kappa_c} M d\kappa)\delta L + R_c \delta L$$

Figure 2.9 : Control volume for the critical tensile tearling work per unit length R_c in a peeling test [26].

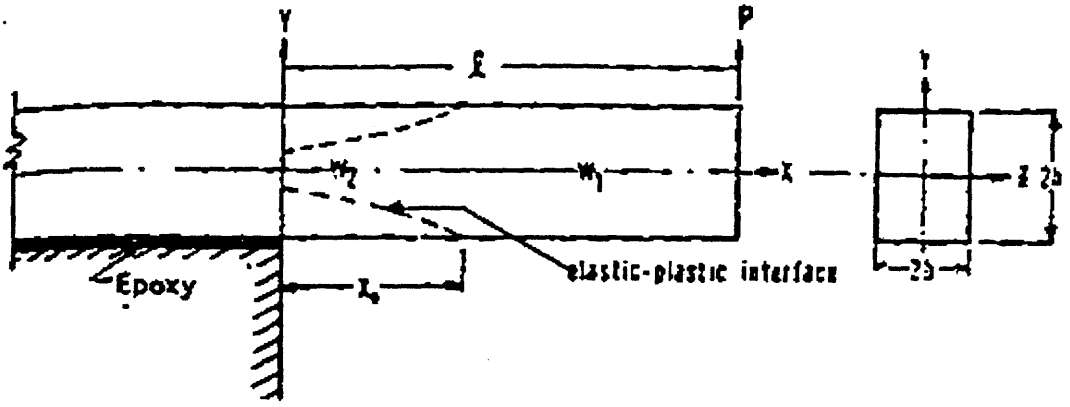

Figure 2.10 : Peeling of an elastoplastic metal epoxy joint by an end force [28].

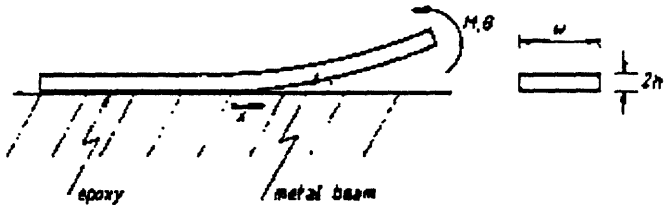

Figure 2.11 : Peeling of an elastoplastic metal-epoxy joint by an end couple [27].

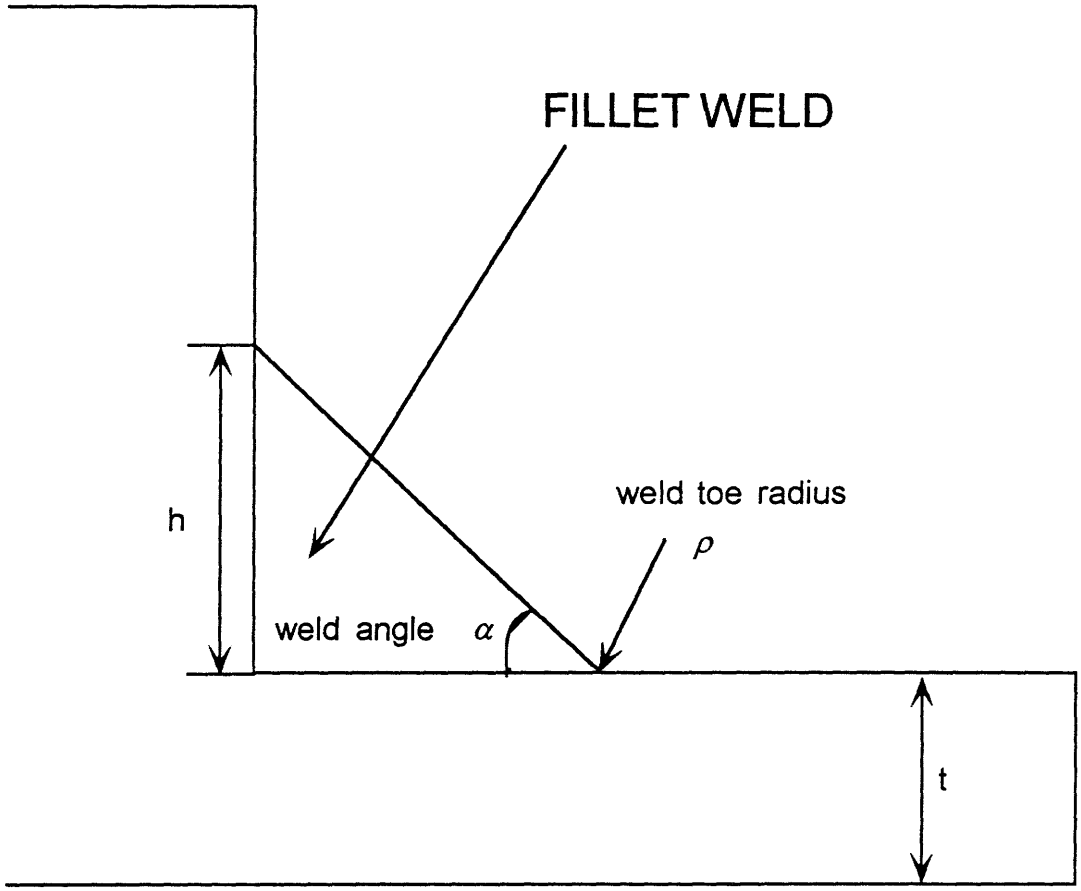

Figure 2.12 : Geometry of a fillet weld

3. Experimental Procedure

3.1 Overview

There are several points associated with this investigation:

1. One point is the use of the video microscope as a tool for the inspection of weldments at structural components under service. The microscope was extensively used to visualize the surface of the weld in order to identify potentially harmful defects.

2. The video microscope was used to investigate real time material behavior during the experimental procedure. The weldments were being observed, while substantial plastic deformation of the specimen was taking place. Crack initiation and growth were recorded.

3. The performance of a structural detail, where large discontinuity and weldment exist simultaneously, was investigated. Large plastic deformation was applied to the specimens, simulating extreme loading caused by a collision or grounding.

4. The effect of notches at the weld toe was investigated for the case where extensive plasticity of the material was taking place. Those notches represented weld defects caused during the welding procedure, such as undercuts.

3.2 Materials

Mild steel, as the most common structural material for ship construction, was used as a baseplate and web metal. Welding of the web on the baseplate was performed using the gas tungsten arc process (GTAW) and TGS-50 (AWS A 5.18 ER70S-G) rods with a diameter of 2.4 mm, as filler metal. The characteristics of the base and the weld metal are summarized in the following Table 3.1:

Table 3-1: Material characteristics

	BASE METAL	WELD METAL
$\sigma_y (N/mm^2)$	281	340
$\sigma_{TS} (N/mm^2)$	346	470
Reduction in area (%)	61.1	36
Charpy energy absorption (−30° C) (Joules)	Not assigned	220
C (%)	0.29 max	0.080
Si (%)	-	0.700
Mn (%)	0.60-0.90	1.310
P (%)	-	0.011
S (%)	-	0.010

3.3 Specimen design

3.3.1 General considerations

The requirement to investigate the performance of a structural detail, under extreme loading, was the primary driver for the specimen design. During the ship structural design process, it is common to decompose a structural component to multiple "T" sections, with an appropriate effective plate width. Therefore, it was assumed to be valid to use a wide beam specimen as a representation of a stiffened plate panel.

The structural details at ships are mostly fillet welded plate combinations. They create large discontinuities in the structure that work as stress and strain concentrators. Fillet welding introduces possible weld defects and "damaged" material at the HAZ. Those unfavorable conditions were simulated on the specimen by welding a web on a wide beam (figure 3.1).

The end of the web, where welding and three-dimensional discontinuity coexist, was the area of focus. In order to avoid having two such areas (one for each web end), the web was welded asymmetrically on the plate. As a result, the one end was in more severe conditions than the other (larger stresses and strains) and it was expected to be the site of failure initiation.

A 3-point bend test fixture was used for the specimen testing. Free space below the specimen was essential not only because large deformations were expected, but also because it would facilitate the maneuvering of the videoscope. This requirement added some special considerations to the design of the experimental setup. The setup is shown in figures 3.2 and 3.3.

3.3.2 Geometry and Fabrication

The base plate samples were prepared from mild steel plate stock, that was roughly 9.5 mm (3/8 in) thick. From each 16X16 inches plate, three base plate samples, 130 mm wide, were able to be cut with a saw. The area where welding was going to be applied was thoroughly cleaned with a power metal brush. The cleaning was performed in order to remove mill scale, that might affect the quality of the weld.

Two of the webs were also made from the 9.5 mm mild steel plates. Their dimensions (130 mm length, 50 mm height) were the same but one of them had a 3 mm bevel at the end, in order to achieve controlled penetration (figure 3.4). Four more webs were made from 20 mm thick plates. They had the same dimensions (130 mm length, 35 mm height) but three of them were beveled. The web surface, expected to be involved in the welding process, was cleaned in order to remove mill scale.

Each web was fillet welded on a base plate. A current density of 180 A was used for the welding. GTAW was preferred because :

- According to the Navy rules the fillet size should be approximately 4.37 mm [24]. This size was easier to achieve with GTAW welding than shielded metal arc welding (SMAW) or gas metal arc welding (GMAW), which are used for ship construction.
- It created smooth and clean weld beads, which facilitated the recognition of cracking initiation and advance using the video microscope.
- The investigation was not focused on the welding process but rather on the effects of the geometry and the strength of the weld.
- A disadvantage of using GTAW was the difficulty to control welding at the ends of the web, where the focus point of the research was. Consequently weld defects were being created at those points, during the welding procedure. Although undesirable in practice those defects were important for the project itself from the point of view of whether they would affect the performance of the weld under extreme loading.

Six specimens were prepared. Two of them, which were constructed using thick beveled webs, were notched at the weld toe. The reason for using beveled webs for the notched specimens, was to ensure the avoidance of peeling fracture initiation. The weld beads at the web end of those specimens were machined, in order to control the weld angle. The notches, which were 1 mm deep and 10 mm wide, were cylindrical with a 0.8 mm radius of curvature (figure 3.5).

The geometry of the six specimens is shown in figure 3.6. Their main characteristics are summarized in Table 3-2. For the first 4 specimens the weld bead and the end of the

web was not machined. Since the welding of the specimens was done manually the geometry of the weld bead was not perfect. Therefore the ideal shape shown in figure 2.4 was not achieved. For this reason measuring the weld angle was not considered practical.

Table 3-2: Specimen Characteristics

SPECIMEN #	1	2	3	4	5	6
Plate length (mm)	400	400	400	400	400	400
Plate width (mm)	130	130	130	130	130	130
Plate thickness	9.5	9.5	9.5	9.5	9.5	9.5
Web length (mm)	130	130	130	130	130	130
Web height (mm)	50	50	35	35	35	35
Web thickness (mm)	9.5	9.5	20	20	20	20
Weld angle (deg.)	AW	AW	AW	AW	57	42
Beveled	No	Yes	No	Yes	Yes	Yes
Notched	No	No	No	No	Yes	Yes

3.4 Equipment

The "Hirox Hi-Scope Video Microscope" was extensively used during the experimental procedure. Detailed information on the characteristics and use of the videoscope is submitted in Appendix B.

The three point tests were performed on a Baldwin testing machine with a maximum load capacity of 60000 lbfs. The specimen was supported on rollers which were part of a

fixture appropriately designed to provide considerable clearance below the specimen. The clearance was needed to allow for large specimen deformations and the maneuvering of the microscope. The rollers were positioned inside grooved metal blocks that were bolted on parts made from a large square metal column. Those two parts were bolted on a beam at a distance determined by the length of the specimen. Since the specimen length was 400 mm, the length between the supports was designed to be 300 mm. The compact design of the specimen support was adapted in order to prevent any lateral movement of its parts during the loading. This was essential because the large bending angles could create significant lateral force resultant. The supporting fixture can be shown in figures 3.2 and 3.3. The upper part of the set consisted of a roller same as the other ones, in a grooved metal block.

A load cell integral to the test machine sensed loads which were displayed on a big dial. The displacements were measured with a micrometer attached on the moving lower part of the testing machine. Both the load and the displacement had to be recorded manually since the particular testing machine was not electronically controlled and automatic data saving ability was not available.

3.5 Experimental procedure

Each specimen was tested using the following procedure:

1. Prior of applying any load to the surface, video images of the specimen were recorded using the video microscope. The area of interest was the fillet weld at the

end of web, near the center of the specimen. At that point failure was expected to occur because of the stress concentration caused by the existing discontinuity.

2. While the video microscope was recording, displacement was being applied. That displacement was the independent variable while the resulting load was the dependent variable. Periodically loading was paused, in order to write down the load and displacements readings obtained by the machine.

3. The specimens were loaded deeply into the plastic regime until slipping at the supports occurred. While loading, continuous video recording of the material behavior at the observed point was sustained. By the moment slipping started to take place the load was released and the specimen was removed.

4. When fracture did not occur during the first loading sequence, the specimen was straightened up by inverting the load and then reloaded again.

5. The video tapes obtained by the experiments were reviewed and processed with the Sony Mavigraph color video printer, in order to obtain still photos.

6. At the cases where tearing of the fillet weld occurred, the peeled portion of the web was cut off to facilitate observation of the fracture surfaces.

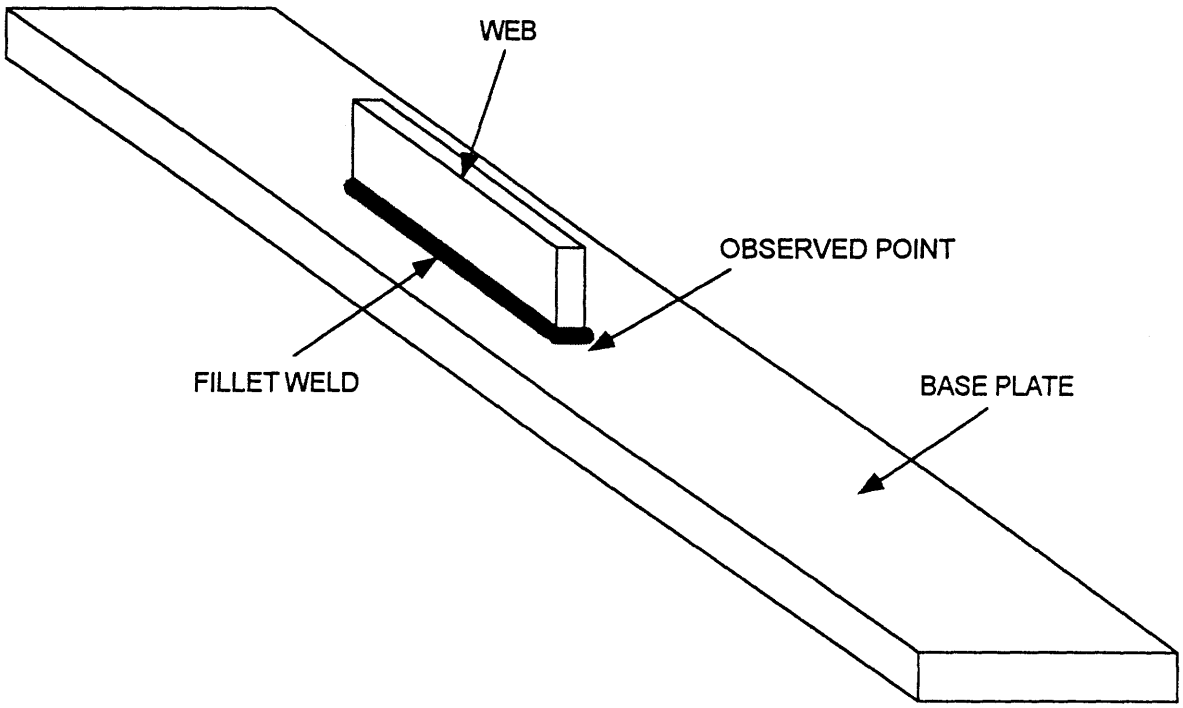

Figure 3.1 : Specimen general view

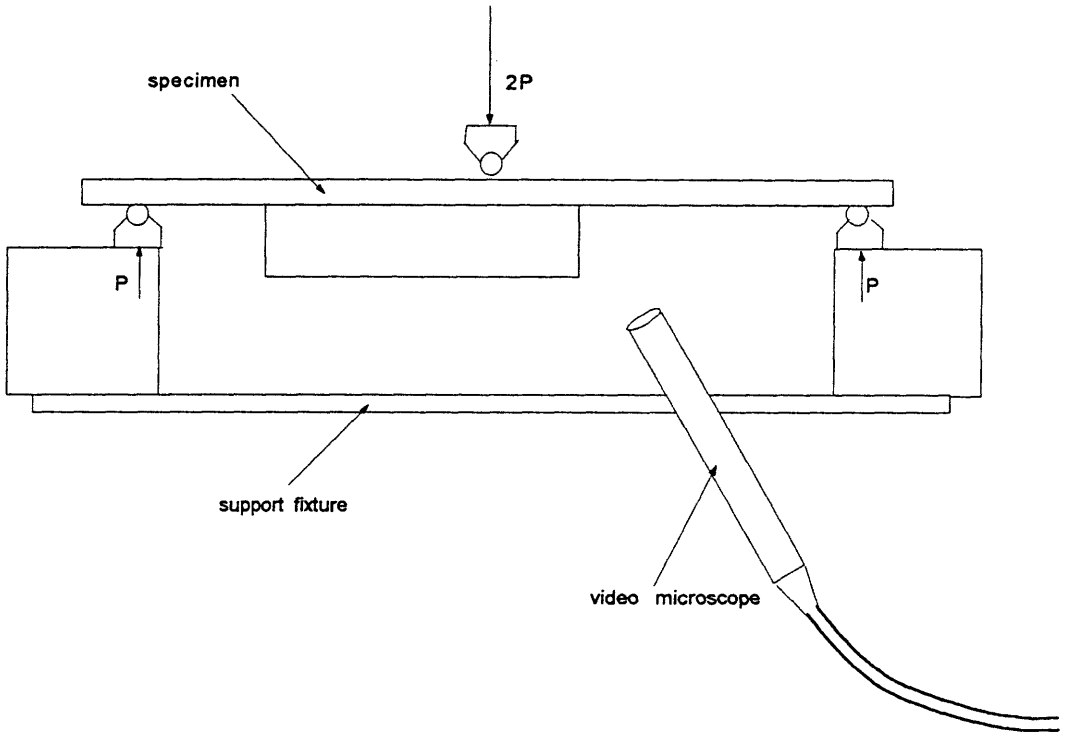

Figure 3.2 : Drawing of experimental setup

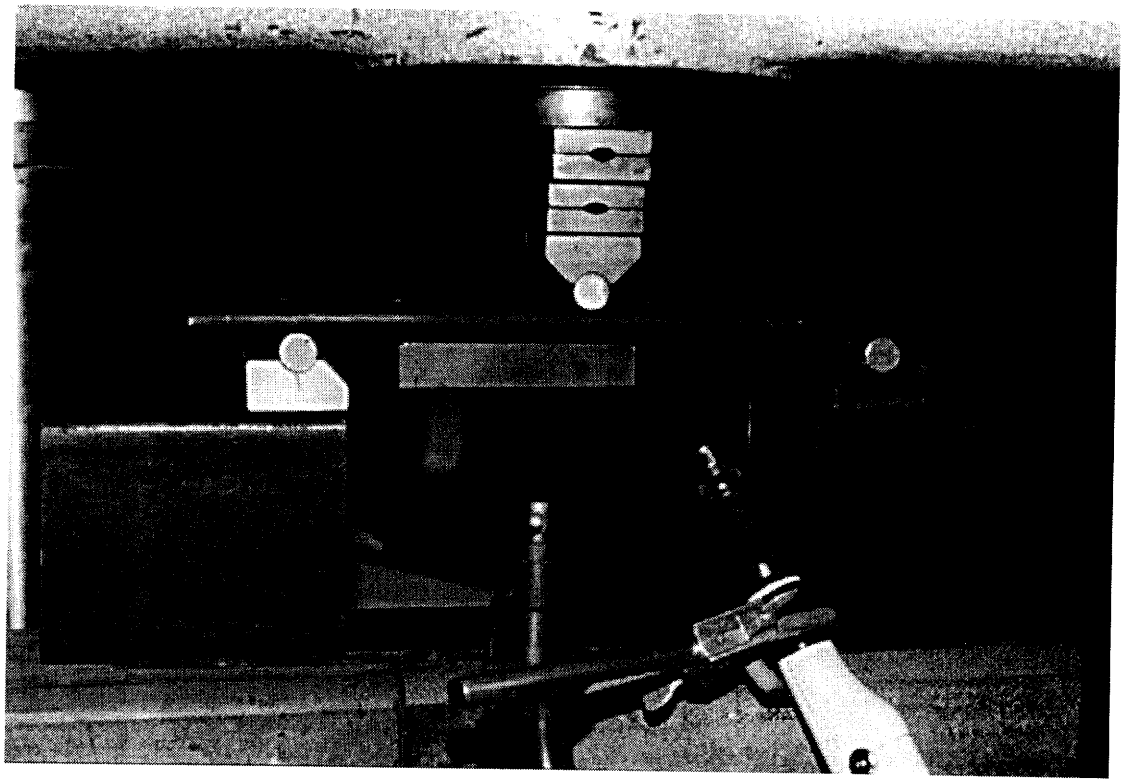

Figure 3.3 : Picture of experimental setup

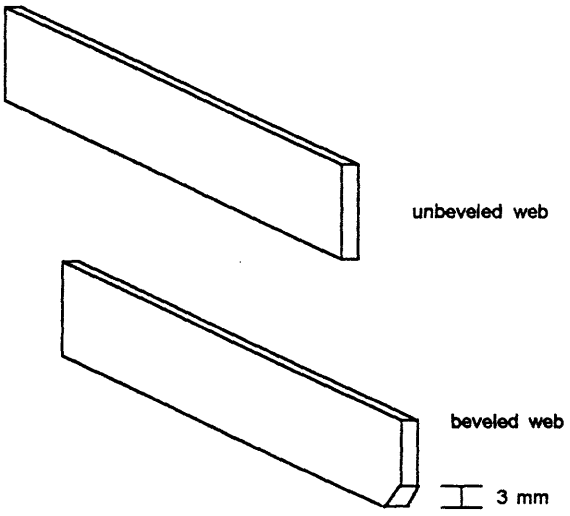

Figure 3.4 : Beveled vs unbeveled web

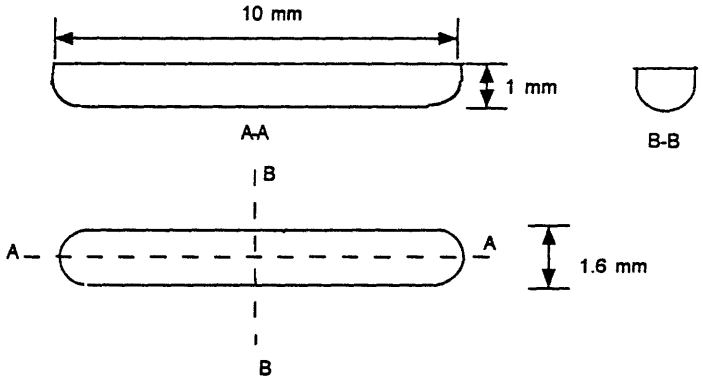

Figure 3.5 : Notch geometry

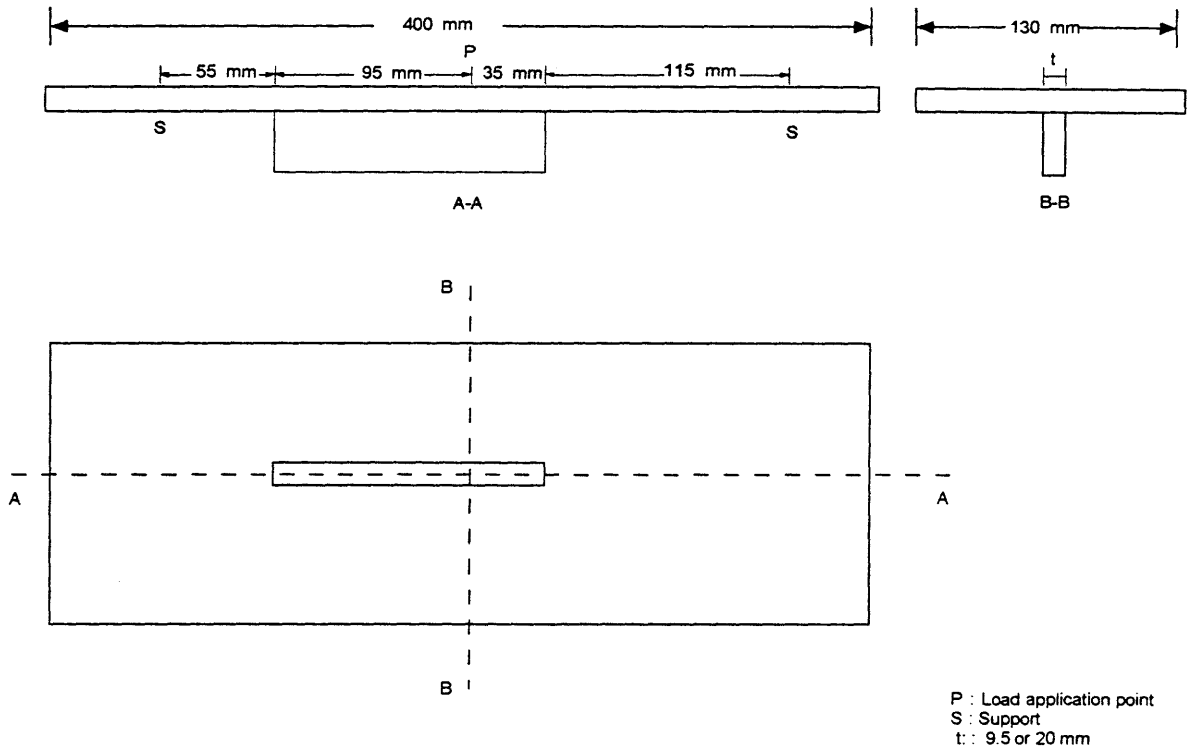

Figure 3.6 : Specimen geometry

4. Results and Discussion

4.1 General

The recorded load-displacement data appear in tabular form in Appendix C and graphically in figures 4.1 through 4.6. Each figure corresponds to a different specimen and shows its response to the different loadings that it was subjected to. The straightening of the specimens after the first loading has not been recorded.

During the experiment, the part of the specimen, where the web had been welded, did not develop any observable curvature. This part of the specimen was much stiffer than the sole plate and therefore could sustain larger loads. Yielding occurred firstly at the base plate and subsequent deformation was localized at a small region (plastic hinge).

Consequently, it can be concluded that, under large plastic deformation, the part of the specimen where the web is welded, behaves as a rigid body and therefore, consumes no work. (It actually consumes some work which stores as elastic energy but is negligible compared to the plastic work dissipated at the rest of the specimen). This means that, in the absence of fracture, the load-displacement curves for all the unnotched specimens should be the same.

Specimen 4 exhibited no fracture even after three cycles. Additionally its load-displacement behavior remained approximately the same at all those loadings (figure 4.4).

Consequently, it can be assumed that at the specific specimen no damage had occurred, at least until the third cycle. Some small deviations can be attributed to the difference between the monotonic and cyclic stress-strain relationship of the mild steel (figure 4.7). As a result, the curves derived from specimen 4 were used as a reference for comparison with the response of the other unnotched specimens.

From Atkins and Mai [27], it is stated that the difference in the loaded work areas between two loading lines, for two specimens with crack areas A and $(A+\Delta A)$, represents the J-integral, provided that no unloading occurs. For the case where elastic effects can be considered negligible, which can be assumed for the case of the large deformations incorporated in the experiment, a rigid-perfectly plastic material behavior can be considered. Then it follows that

$$J = R + \frac{d\Gamma}{dA}, \tag{4.1}$$

where R is fracture work per unit of crack area and $d\Gamma$ is the remote plastic work, associated with a dA increase in the crack area. Then the area between the loading curves of a specimen with a crack A and a specimen with a crack $(A+\Delta A)$ will be

$$\Delta W = J \cdot \Delta A = R \cdot \Delta A + \Gamma, \tag{4.2}$$

where Γ represents the total plastic work accompanying crack propagation.

4.2 Fracture at the weld toe (Specimen 1)

Specimen 1 is the specimen that has a 9.5 mm thick web with no beveling at the end. Its load-displacement behavior can be seen in figure 4.1.

The observation of the weld toe with the video microscope, during the application of the load, revealed material popping out as soon as loading started to be applied. This indicates that fracture initiated very early at the toe of the weld. For this reason the stiffness of the specimen was reduced. This can be seen, when comparing the load displacement curve of specimen 1 with the reference curve of specimen 4 (figure 4.8).

An interesting point was the fact that, although there were cracks on the weld metal near the weld toe, fracture took place at the base metal exactly at the fusion line (figure 4.9). The reason for this are the low toughness characteristics of the HAZ and the large strain concentration at that area, which was caused by a convex weld profile. In the absence of a strain concentration the effect of the HAZ on the safety of a structure is less important. This results from the fact that the high hardness of the HAZ prevents straining in it, since deformation is redirected to the surrounding softer material [33]. But if a geometric configuration or defect introduces a large strain concentration at the HAZ, compared to the rest of the material, fracture may take place.

In specimen 1 the crack propagated along the weld toe at a distance equal to the thickness of the web and was arrested. Even under the subsequent large plastic deformation additional propagation did not occur. The reason for this is both the absence of stress

concentration far from the web and the adequate toughness of the mild steel, under static loading at room temperature.

Under dynamic loading conditions, it is possible that the crack would have propagated across the base plate. The strain rates occurring during collision and grounding correspond to those of the Charpy impact test. A minimum Charpy energy requirement for grade A steel is considered to be 27 Joules at 20^{o} C, but at areas where welding is involved that requirement may not be fulfilled [34]. The Charpy V-notch energy and the critical stress intensity factor can be related with:

$$K_{IC} = 21.6(CVN)^{0.17}, \tag{4.3}$$

where CVN is given in Joules and K_{IC} in $\text{MPa}\sqrt{\text{m}}$. Therefore, a minimum requirement for the critical stress intensity factor of grade A steel under dynamic loading is 37.8 $\text{MPa}\sqrt{\text{m}}$ at 20^{o} C. At very high strain rates the yield strength of A-36 steel may reach a value of 82 ksi (565 Mpa) [53]. Under those conditions brittle plain strain behavior is expected for a plate with thickness

$$t \geq 2.5 \cdot \left(\frac{K_{IC}}{\sigma_Y}\right)^2 = 2.5 \cdot \left(\frac{37.8}{565}\right)^2 = 0.011 \text{ m} = 11 \text{ mm}. \tag{4.4}$$

This result means that brittle behavior will be expected by that steel even at 20^{o} C if dynamic loading is applied. If we consider the specimen configuration under dynamic loading and with a base plate thicker than 11 mm then the crack, originating at the toe of the weld, may propagate through the entire thickness of the specimen. This depends on the

crack size at the time that it clears the web end area. If this size is greater than the critical one, brittle fracture will occur.

From this we can conclude that the thinner the web the greater is the possibility for crack arrest. Therefore, considering this failure mode, it appears to be preferable to use thin stiffened webs in ship structural components than thick unstiffened ones. The concept can be extrapolated to other structural details, accordingly. For example in figure 4.10, the type "a" configuration has the smaller weld width on the base plate and eventually a smaller initial crack size. The K_{s0} values on that figure correspond to structural stress concentration factors, used for fatigue assessment. It can be seen that preferring the type "a" configuration does not compromise the fatigue resistance of the structure.

The "crashworthiness" of the specimen can be described by the work that is needed to obtain a specific deformation, which is represented by the area below the corresponding load-displacement curve. This can be compared with the work required to deform similarly the reference specimen. Those works can be calculated by numerically integrating the corresponding curves.

Refer to figure 4.8. It has been found that, the work that was consumed during the experiment by specimen 1 is $W_1 = \text{Area(OBC)} = 883500\ \text{N} \cdot \text{mm}$. The reference work is $W_{ref} = \text{Area(OAC)} = 1079500\ \text{N} \cdot \text{mm}$. Their difference represents the J-integral by the relationship $J \cdot \Delta A = R \cdot \Delta A + \Gamma = \text{Area(OAB)} = 196000\ \text{N} \cdot \text{mm}$. This value is geometry dependent, mainly by the contribution of the plastic work Γ, that occurs at the uncracked part of the plate. It can be observed that W_1 is approximately 82 % of W_{ref}. This number is

close to the ratio of the uncracked plate ligament to the full width of the base plate which is approximately 88 %.

It appears that the length of the crack, which equals the width of the weld at the end of the web, affects directly the ability of the specimen to absorb energy. This observation leads to the same conclusion for the "crashworthiness" of a structure as the one obtained for brittle fracture: short welds are better. Therefore the proposed design implementation favors both the static and dynamic loading case.

4.3 Peeling fracture (Specimens 2 and 3)

4.3.1 Observations and analysis

Specimen 2 has a 9.5 mm thick web with a beveled end. Specimen 3, on the other hand, has a 20 mm web with no beveling. Both specimens were subjected to deep plastic deformation twice. The first loading was stopped when slipping at the supports started. Then, reversed load was applied until the curvature of the specimens reached a zero value. After that, the specimens were reloaded . The load-displacements curves are shown in figures 4.2 and 4.3, for each specimen respectively.

During the first cycle no observable damage seemed to occur at both specimens. An indication that a damage mechanism was being in progress, is the difference of their response compared to the reference one (figures 4.11). At the elastic range the two curves

are almost identical, implying no crack initiation. The difference that appears between the two curves in the plastic range is caused by the plastic deformation of the weld metal at the end of the web. The base plate, which originally could be thought clamped at the web end, now gets a rotation at that point. This reduces the stiffness of the system, which now requires less work for a given deformation. On the other hand, an amount of work is needed to deform the weld at the end of the web. The balance of those two mechanisms determines whether single flow at the base metal is more favorable than flow at both the base and weld metal. The same concept is described by Atkins and Mai [27] who determine the conditions under which flow is more favorable than flow and adhesive fracture together.

During the second loading, fracture initiation occurred at the end of the web. After a transition state, fracture propagated along the weld in a steady state tearing mode. In figures 4.12 and 4.13, the load displacement curves of specimens 2 and 3 are plotted in comparison with the second loading curve of the reference specimen. The points of those curves are related to pictures where crack initiation and propagation are shown. These pictures are shown in Appendix D. The crack length at different loading stages has been measured from those photos. The results are shown in Table 4.1 for specimen 2 and table 4.2 for specimen 3.

Table 4.1 : Specimen 2 crack lengths and loads for sustaining constant moment

Point	Load (lbs)	Displacement (mils)	Crack length (mm)	Constant moment load (lbs)
D	4620	1753	4	4620
E	4240	1855	6.5	4525
F	4020	1905	8.5	4452

Table 4.2 : Specimen 3 crack lengths and loads for sustaining constant moment

Point	Load (lbs)	Displacement (mils)	Crack length (mm)	Constant moment load (lbs)
D	4440	1258	2	4440
E	4360	1340	4	4365
F	3860	1440	10.5	4145
G	3700	1588	12.5	4074

For specimen 2, initiation of cracking took place at the second cycle and specifically at the time that corresponds to the point B of figure 4.12. From point B to C the crack propagated along the thickness of the web. The time interval from point C to D

corresponds to a period, during which transition from lateral to longitudinal cracking took place. The rest of the points are the steady state tearing mode.

For specimen 3, cracking initiation corresponds to point B of figure 4.13. The crack propagation along the web thickness corresponds to the (BC) interval while transition from lateral to longitudinal cracking is represented by the line segment (CD). The points from D to G correspond to the steady state tearing of the fillet weld.

Cracking at the second loading is closely related to the fact that plastic deformation of the weld took place during the first cycle. It has been noted that low cycle fatigue is a cumulative damage mechanism. For specimen 2, the plastic deformation of the weld metal, during the first cycle, caused a form of material degradation that was stored and added to the damage occurred at the second loading . In the case of high and low cycle fatigue this would correspond to the propagation of a crack. In the case of very low cycle fatigue of low carbon steel, the case is the reduction of the concentration of uncracked pearlite in the metal matrix [19]. That means that a portion of the pearlite of the weld metal broke during the first cycle which created an amount of microvoids. This reduced the ductility of the weld metal and weakened its fracture resistance.

From that it can be concluded that, if plastic deformation of the weld metal is avoided at the first cycle, the fatigue mechanism will not be able to take place. Therefore, if the end weld were strong enough to avoid plastic straining, peeling fracture could be avoided, even under subsequent loading. Apparently this was the case for specimen 4, which had large width and penetration at the end.

Specimen 2 was intended to have a strong weld with penetration but post-fracture examination revealed a defect, which substantially reduced its ability to avoid straining. This examination was done using the video microscope. A general view of that surface at the end of the web is shown in figure 4.14. It can be seen that the beveled part of the web was not filled with weld metal,, which created a large void a the root of the weld. This corresponds to an incomplete fusion type of defect, which is termed "bridging" (figure 2.7). A closer view of the fracture surface reveals a typical microvoid growth and coalescence fracture mechanism (figure 4.15).

A similar fractographic examination was performed for specimen 3. A general view of the fracture initiation site at the end of the web can be seen in figure 4.16. Such an examination would lead to a false result without the information gathered by the video microscope. It shows that fracture initiated at the center of an arc strike that was created on the weld bead during welding. A chevron pattern is visible at that area converging at the center of the arc strike (figure 4.17). Indeed crack propagation across the arc strike surface occurred in a brittle manner and started in the middle of the defect. But this occurred after the initiation of the ductile fracture. This can be seen from the pictures in Appendix D. When the tip of the ductile crack reached the hard defect area, it was momentarily arrested. Then brittle fracture occurred, until the two cracks joined together. After that, the ductile fracture mechanism continued.

Fracture initiation took place by a microvoid growth mechanism, which was favored by the high stress triaxiality at the area around the centerline of the web. Although

the arc strike created many small cracks on the surface of the weld, the material at the defect area was not strained, since it was harder than the rest of the weld metal. It can also be argued that, since fracture occurred at the second cycle the residual stress field created by the arc strike had been degraded. Therefore, it can be generally concluded that the existence of the defect on the surface of the weld metal did not affect its performance under very low cycle fatigue.

Comparing the two specimens it can be seen that at the second cycle fracture at specimen 3 takes place at smaller deformation compared with specimen 2. This can be attributed to the effect of the thickness of the web on the stress-strain field of the weld metal. The material constraint, at the centerline of the thick web, imposes higher triaxiality conditions than at the case of the thinner web of specimen 2. Therefore it appears that under low cycle fatigue conditions fracture initiation will be delayed at a weld with small width. This conclusion is the same as the one derived for the case of fracture at the weld toe. Consequently, similar design proposals can be stated.

4.3.2 Calculations

At the steady state of peeling fracture, the tearing resistance R_C of the weld has been calculated. From eq. (2.23) R_C is determined as the difference of the work done by the critical moment and the plate bending work. Referring to figure 2.9, it can be seen that the first term corresponds to the work under a constant moment curve, while the second one corresponds to the work obtained by, an experimentally derived, moment-curvature

relationship. Similarly the tearing work of the weld can be found from the load displacement curve obtained for specimens 2 and 3.

Specimen 2

In order to calculate the tearing resistance of the fillet weld at specimen 2, the steady state portion of the load-displacement curve must be identified. This portion starts when the tip of the propagating crack clears the end of the web and reaches a geometrically homogeneous area. Examining the crack propagation during the experiment, indicated that steady state peeling fracture started at the time which corresponds to the point D of the curve in figure 4.12. The bending moment at this point is the critical one and is given by $M_C = P(L+a)/2$, where P is the load measured at that point, L is the distance of the web from the support and a the crack length. At subsequent loading times (i.e. points E, F), the crack length changes. In order for the moment to stay constant, the load P should be reduced, accordingly. The loads that give constant moment at the *ith* point of the steady state can be found by $P_i = 2M_C/(L+a_i)$, where a_i is the crack length at that point.

The crack lengths were known for the points D, E and F (Table 4.1). Using that information, the load that corresponds to M_C can be derived for each of those points. The results are shown in Table 4.1. The area (DEFG) corresponds to the fracture work needed for a crack propagation of $\Delta a = a_F - a_D$, where a_F and a_D are the crack lengths at the points F and D respectively. The fracture work will be R_C = Area(DEFG)/Δa.

For specimen 2 the critical moment M_c is found to be equal to 1223 N m. The tearing resistance was calculated:

$$R_c = \text{Area(DEFG)}/\Delta a = 3667\ \text{N}\cdot\text{mm} / 4.5\ \text{mm} = 815\ \frac{\text{N}\cdot\text{mm}}{\text{mm}}. \qquad (4.5)$$

A tearing resistance value can be calculated using the material properties, the geometry of the weld and eq. (2.21). The sum $u_i + u_f$ in that equation is the displacement of the web with respect to the base plate at the crack tip. By cutting the web at the point where the crack tip has reached, this displacement can be approximately measured using the video microscope. That displacement has been measured to be approximately 0.53 mm (figure 4.18). From figure 4.20 the weld lengths can be measured. It can be seen that they have different size at each side of the fillet. An average value has been taken to be 4.5 mm. Therefore

$$R_c = P_L(u_i + u_f)/2 = 2kd(u_i + u_f)/2 = 2 \times 0.75 \times 470 \times 4.5 \times 0.53/2 = 841\ \frac{\text{N}\cdot\text{mm}}{\text{mm}}, \quad (4.4)$$

which is very close to the value calculated from the experiment.

The applicability of eq. (2.24) and (2.27) in determining the fracture work of the fillet weld has been investigated. A subtle point associated with those formulas is the determination of the flow stress that should be used. The yield or even the tensile strength of the mild steel can not be used since eq. (2.25) and (2.28) are not satisfied. This means that fracture should not have occurred. The fact that tearing of the fillet weld took place during the experiment, comes from the cyclic strengthening of the mild steel. During the

second cycle the concept of flow stress is lost as it can be seen from figure 4.7. The material obeys a power law stress-strain relationship. Since very large deformations took place during the experiment the maximum stress should have reached quite high values. An average value for the flow stress is taken to be $450\ \mathrm{N/mm^2}$.

Applying eq. (2.24) and (2.27) on the data that correspond to the initiation of steady state, result to tearing resistance values of 432 and 416 $\frac{\mathrm{N \cdot mm}}{\mathrm{mm}}$, respectively. The difference between those numbers and those calculated earlier can be attributed to the fact that those equations have been derived for elastic perfectly plastic material and for one loading cycle. Since at the second cycle the material behavior resembles better a power hardening law, strain hardening becomes important. That problem has been partially solved by using a larger flow stress, which accounts for the increased amount of strain energy dissipated in the base metal. This assumption overestimates that energy because assigns the larger flow stress to all the material. R_C is calculated by eq. (2.24) and (2.27) as the difference between the applied external work and that dissipated at the base plate. Therefore overestimation of the latter results to underestimation of R_C, which is proven in our case.

Specimen 3

The steady state tearing resistance of the fillet weld has been calculated for specimen 3 using the same procedure as for specimen 2. The initiation of steady state has been recognized to be at point D. The critical moment M_C has been found to be equal to 1155

$\mathrm{N}\cdot\mathrm{m}$. The crack lengths that correspond to the points D, E, F and G of figure 4.13 and the corresponding loads that would give a constant moment M_C are shown in Table 4.2.

The area (DEFGH) represents the fracture work needed for a crack propagation $\Delta a = a_G - a_D$, where a_G and a_D are the crack lengths at the points F and G, respectively. Then the tearing resistance will be:

$$R_C = \text{Area(DEFGH)}/\Delta a = 6900\ \mathrm{N}\cdot\mathrm{mm} / 10.5\ \mathrm{mm} = 657\ \frac{\mathrm{N}\cdot\mathrm{mm}}{\mathrm{mm}}. \qquad (4.5)$$

Alternatively R_C can be calculated using eq. (2.21). The sum $u_i + u_f$ which is the displacement of the web with respect to the base plate at the crack tip has been measured similarly as it has been performed for specimen 2. Using a magnified view, obtained with the video-microscope (figure 4.20), it has been found to be 0.4 mm. From figure 4.21 the weld lengths can be measured. Since they have different size at each side of the fillet, an average value equal to 4.5 mm has been taken. Therefore

$$R_C = P_L(u_i + u_f)/2 = 2kd(u_i + u_f)/2 = 2 \times 0.75 \times 470 \times 4.5 \times 0.4/2 = 630\ \frac{\mathrm{N}\cdot\mathrm{mm}}{\mathrm{mm}}, \qquad (4.6)$$

which is very close to the value calculated from the experiment.

The fracture work has been calculated using eq. (2.24) and (2.25). The values have been obtained are 349 and 359 $\frac{\mathrm{N}\cdot\mathrm{mm}}{\mathrm{mm}}$, respectively. The underestimation of R_C occurs for the same reasons that have been stated for the case of specimen 2.

A summary of the tearing resistance results obtained with the different methodologies for both specimens is shown in Table 4.3. The fillet weld in specimen 2 exhibited larger values because it had larger average size.

Table 4.3 : Tearing resistance calculation results $(\frac{N \cdot mm}{mm})$

Methodology	Specimen 2	Specimen 3
Equation 2.23	815	657
Equation 2.21	841	630
Equation 2.24	432	349
Equation 2.27	436	359

4.4 Effect of weld defects (Specimens 5 and 6)

4.4.1 Observations and analysis

Specimens 5 and 6 are those with a notch at the toe of the weld and their design characteristics are shown in Table 3.2. They were both loaded twice in the same way as it

had been performed for the other specimens. Their response to the loadings are shown in figures 4.5 and 4.6 respectively.

In figure 4.22 the load displacement curves of specimen 5 are plotted independently and they indicate points that are related to photos in Appendix D. Point A1 corresponds to the crack initiation, while point C1 corresponds to the final stage of crack propagation at the first cycle. Initiation took place at the tip of the notch, where the strain concentration is large. Another site with large strain concentration is the end of the notch at the surface of the base plate. For the current experiments, the notch end had a large radius which reduced the severity of that concentration.

Referring to the photographs we can see that, for specimen 5, one of the notch ends coincides with an area where the toe of the weld has a discontinuity. This increases significantly the stress concentration. For this reason cracking initiated very early at that point, whereas the other side of the notch did not show any indication of cracking. At that side fracture started at the second cycle and specifically at point A2 of figure 4.22.

Figure 4.23 shows the load displacement curves for specimen 6 with reference to points that correspond to photos shown in Appendix D. The identification of crack initiation was very difficult for specimen 6. Many small surface cracks were created (point A1). Those cracks became clearly visible only at large deformations (points B1, C1). At point C1 multiple cracking appeared also at the notch end at the surface of the base plate.

Multiple cracking occurs because the existence of flow stress distributes strain to a large area. Referring to figure 4.7, it can be seen that this does not happen at the second

cycle. The power law material behavior, during that cycle, caused strain concentration at points where stress concentration existed. For that reason only one crack grew during the second cycle in specimen 6 (points B2 through D2).

This observation indicates the importance of the second cycle in a structure subjected to large deformation. Fracture in the case of very low cycle fatigue is strain controlled. Weld defects and geometric discontinuities can cause large stress concentrations which can be interpreted to strain concentrations. Research on methods that could be used to reduce stress concentration in a structure has been extensively performed for the case of high cycle fatigue [52]. It can be concluded that any design practice that reduces the stress concentration, used for fatigue prevention, will favor the resistance of a structure to very low cycle fatigue.

4.4.2 Calculations

The JWES approach mentioned in 2.7.3 can be applied for the geometry of the specimen in order to investigate the case where fracture at the fillet weld toe will initiate. At large strains the effect of a small surface crack on the stress profile is negligible and it can be assumed that $\sigma_{net} = \sigma_g$ for $\sigma_{net} \geq \sigma_Y$. Then the applied CTOD will depend on $\tilde{K}_\varepsilon = \tilde{K}_t^{2/(1+n)}$.

Although the average stress concentration factor $\tilde{K}_t$ for the whole cross section of the plate is not known the local K_t at the toe of the weld can be given by eq. (2.36). This

result must be multiplied by a factor that will take into account the influence of the undercut. For the case of a 45^o weld, the magnification factor is 1.39 for an undercut depth of 1 mm. We may assume that the same magnification occurs at specimens 5 and 6. The radius of curvature at the toe of the of weld is taken equal to the radius of curvature of the notch, which is 1/32 of an inch. It has been assumed that eq. (2.36) can be extrapolated for the case of $t/\rho = 12$. The values of K_t that were calculated for specimens 5 and 6 are 3.66 and 3.32, respectively.

Using K_t instead of $\tilde{K}_t$ will underestimate the total fracture resistance of the base plate but it will represent the case for fracture initiation at the toe of the weld. Whether the fracture will propagate to catastrophic failure depends on the fracture properties of the material under the specific loading conditions and the size of the initial crack. The case is the same as that analyzed in 4.2.

The relationship between the actual flaw geometry and the LEFM-based equivalent through thickness crack flaw can be found from figure 4.24 [54]. If we assume an initial flaw with depth 0.1 mm it will be found that $\overline{\alpha}$ is approximately 0.1 mm also. Using eq. (2.30) for large deformations, the critical strain to fracture will be given by

$$e_f = \frac{\left(\frac{\delta_c}{\overline{\alpha}} + 1.5 \cdot e_Y\right)}{3.5 K_t^{2/(1+n)}}, \tag{4.7}$$

where δ_c is the critical CTOD and e_Y is the yield strain.

It has been mentioned that fracture takes place in the base metal, rather than in the HAZ. The case differs from that of specimen 1 because the strain concentration is not any more in the toe of the weld. The wide notch causes strain concentration in the base metal, which deforms more easily. For this reason δ_c values that correspond to the base metal must be used, instead of values that correspond to the HAZ. For mild steel typical δ_c value can be taken to be 0.15 mm. The strain hardening exponent was taken equal to 0.24 [55]. Using those numbers, we find that the critical strain is 0.054 for specimen 5 and 0.063 for specimen 6.

LiLiang has performed a finite element modeling of the experiments. From that model the relationship between the applied displacement and the nominal strain at the toe of the weld has been found (figure 4.25). During the experiments, the displacements at which cracking initiated were approximately 17 mm for specimen 5 and 20 mm for specimen 6. Those displacements correspond to nominal strain values of 0.057 and 0.067 respectively.

It can be seen that there is a good agreement between the predicted critical strain range and the experimental results. This supports the validity of the JWES method for fracture assessment and therefore the validity of eq. (4.7), for the case of large strains. This formula proves the strong influence of the stress intensity factor on the value of the critical strain to fracture. It also shows the reason why alternating plasticity may become catastrophic. After each cycle the equivalent crack length $\overline{\alpha}$ increases which reduces the e_f. If the cyclic loading is displacement controlled, reduction of e_f will result to increase of the crack growth per cycle.

Another parameter that changes with alternating plasticity is the strain hardening exponent n. For mild steel it has been found that the cyclic strain hardening exponent is equal to 0.19 [17]. The smaller value of n results to larger strain concentrations for the same stress concentration at the second cycle than at the first. Consequently, the ability of the structure to sustain large deformations without fracture is reduced during cyclic loading.

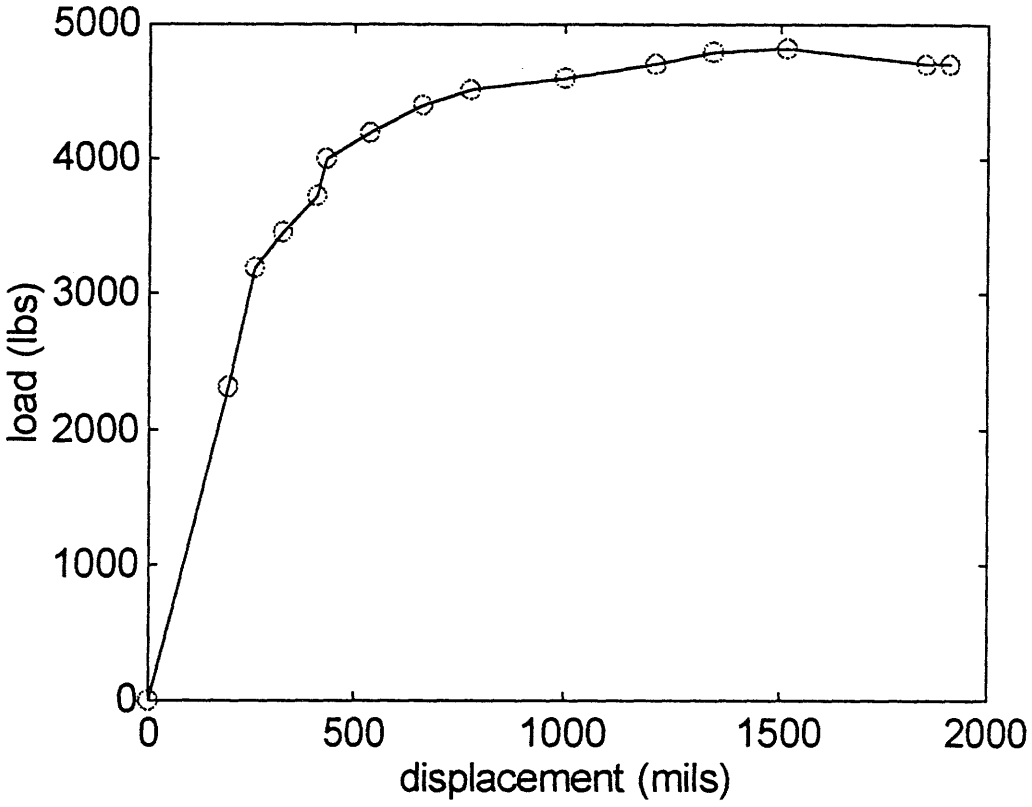

Figure 4.1 : Specimen 1 load-displacement curve.

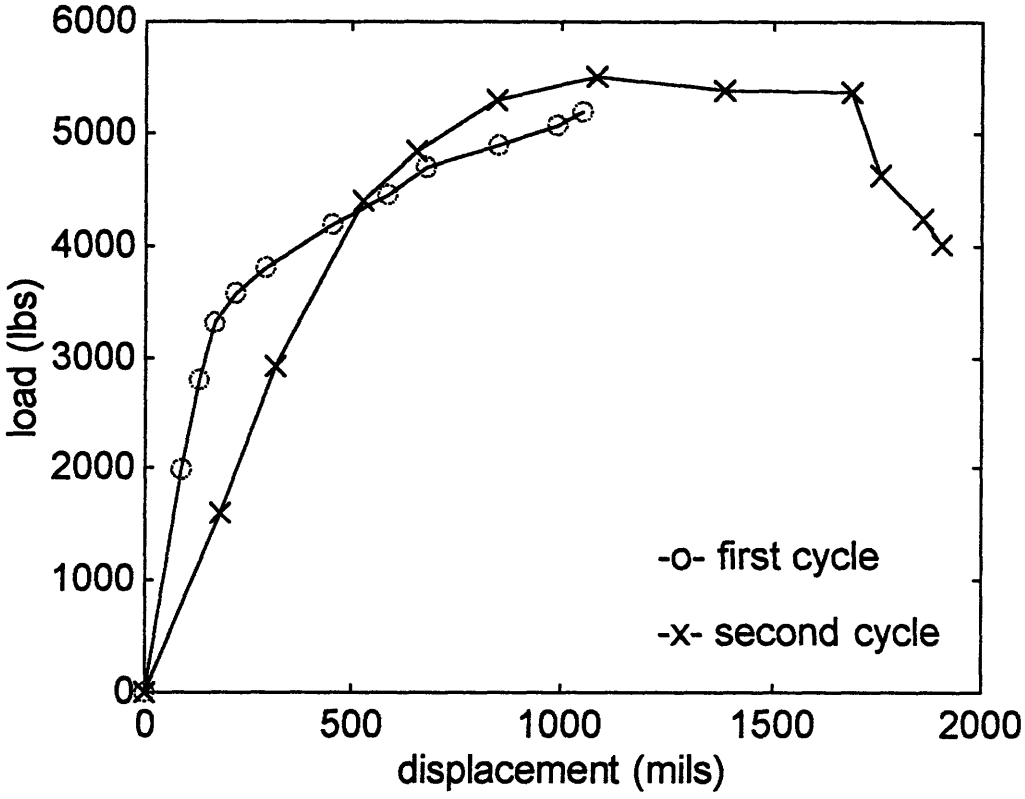

Figure 4.2 : Specimen 2 load-displacement curves.

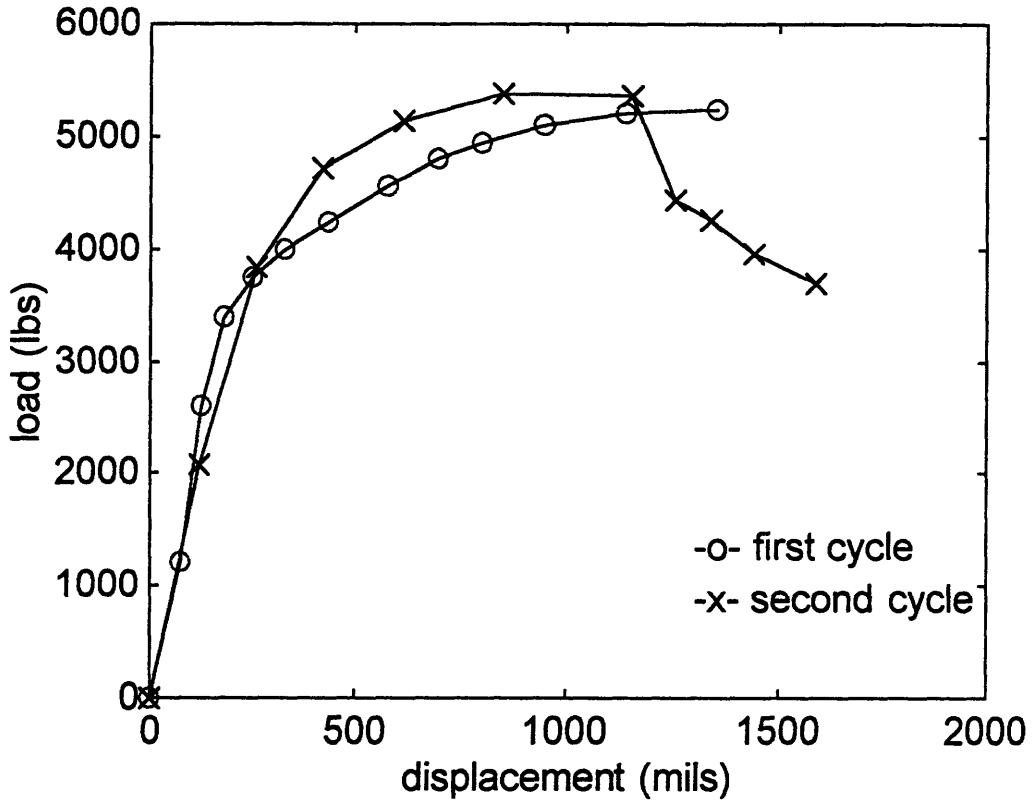

Figure 4.3 : Specimen 3 load-displacements curves.

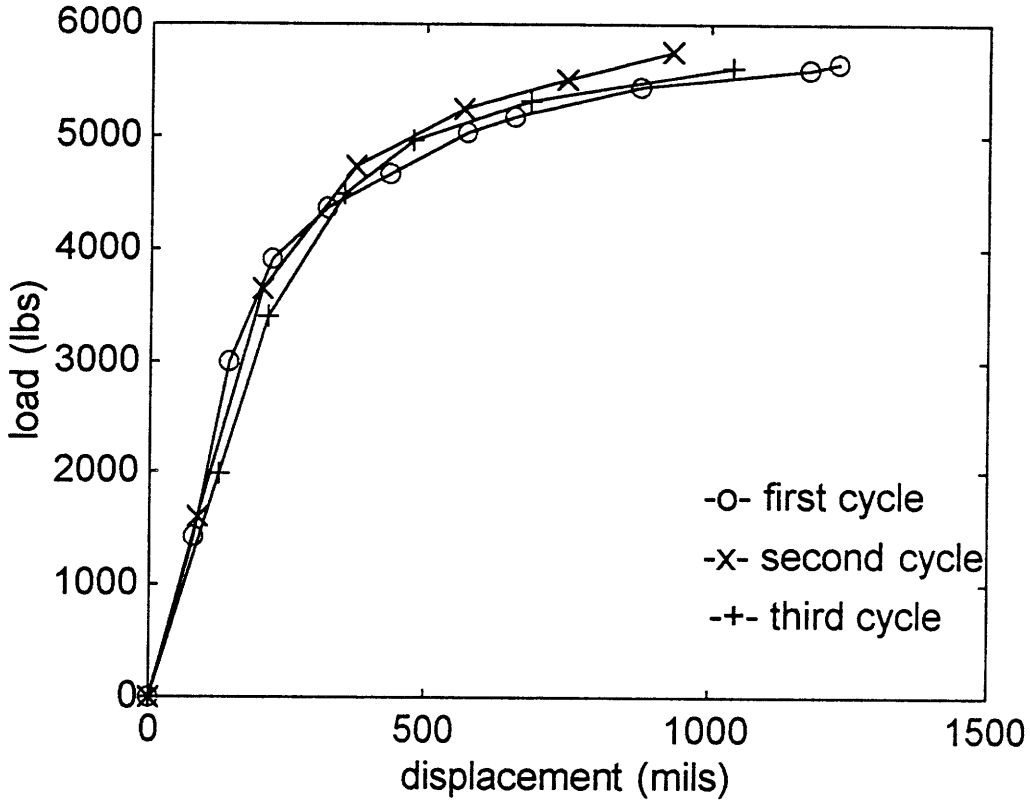

Figure 4.4 : Specimen 4 load-displacement curves.

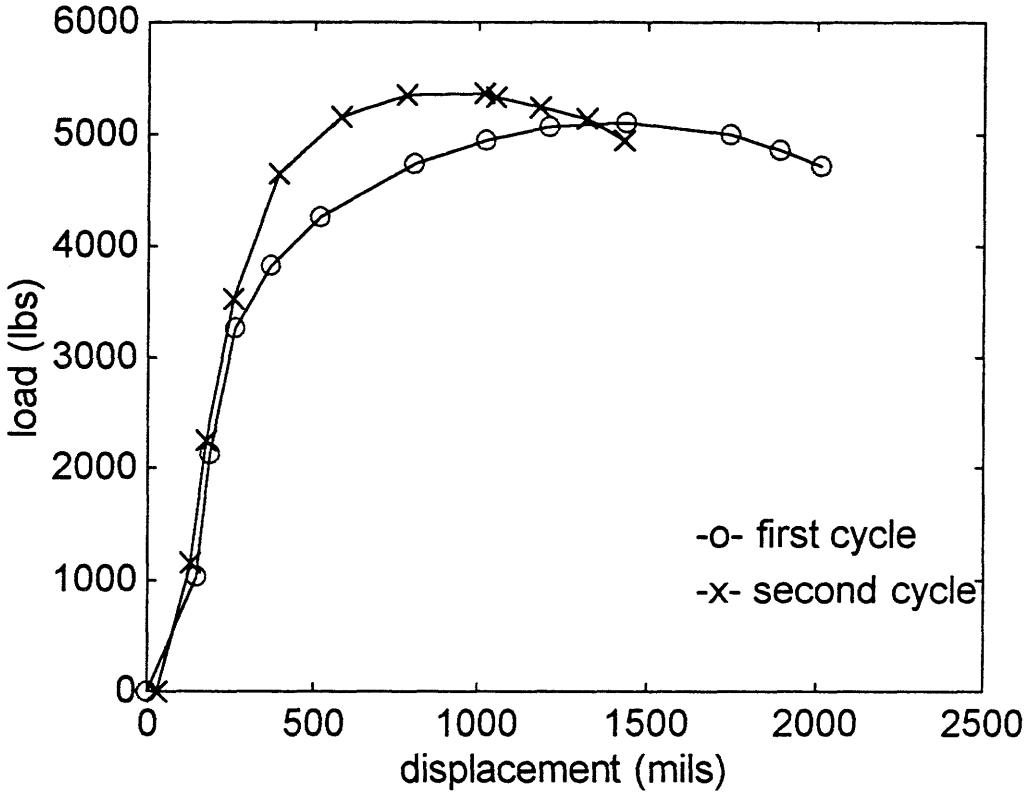

Figure 4.5 : Specimen 5 load-displacement curves.

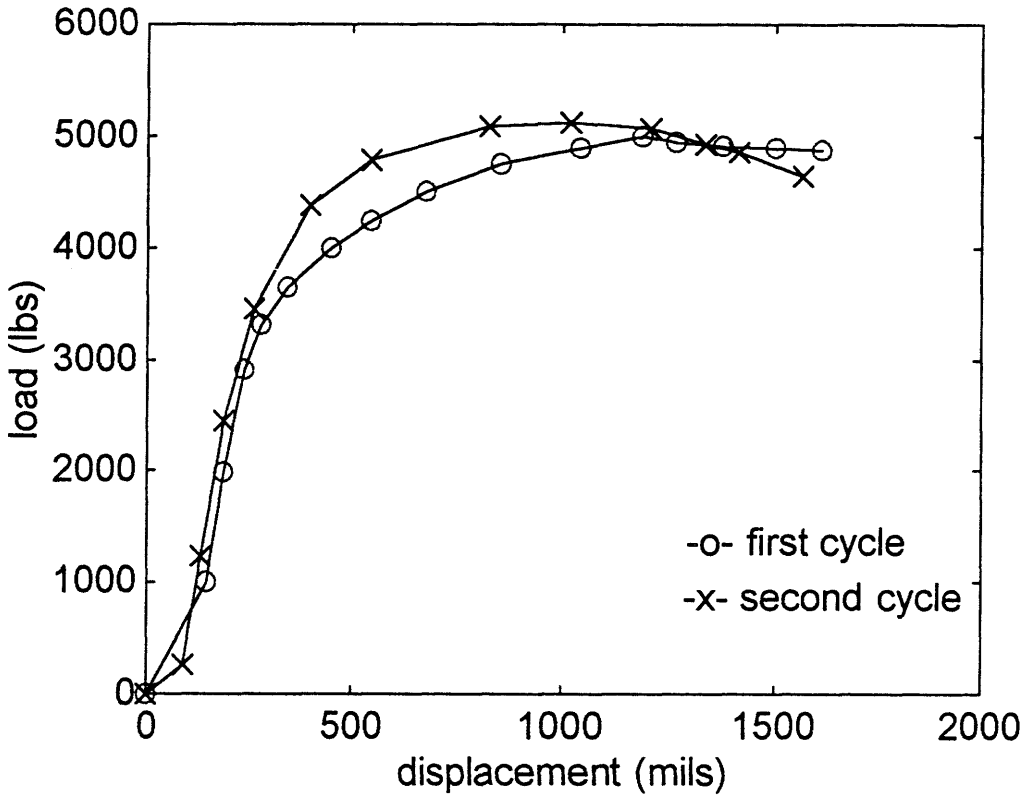

Figure 4.6 : Specimen 6 load-displacement curves.

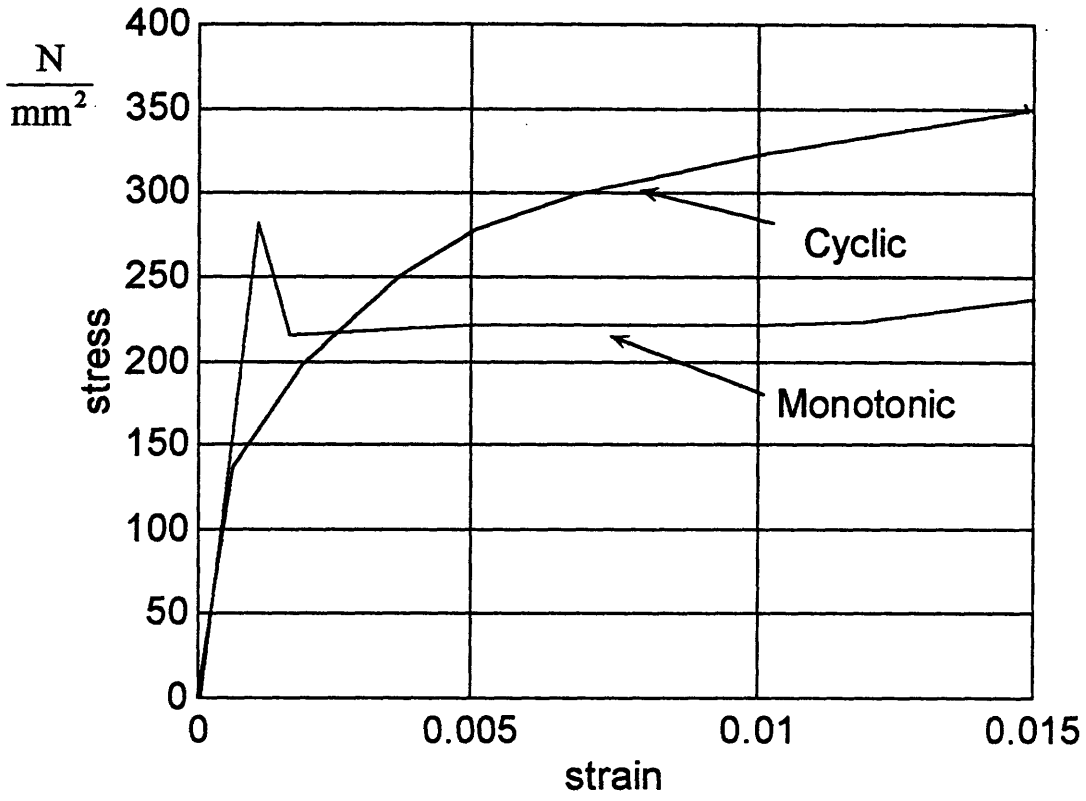

Figure 4.7 : Comparison between monotonic and cyclic stress-strain curves for ASTM A-36 structural steel [52].

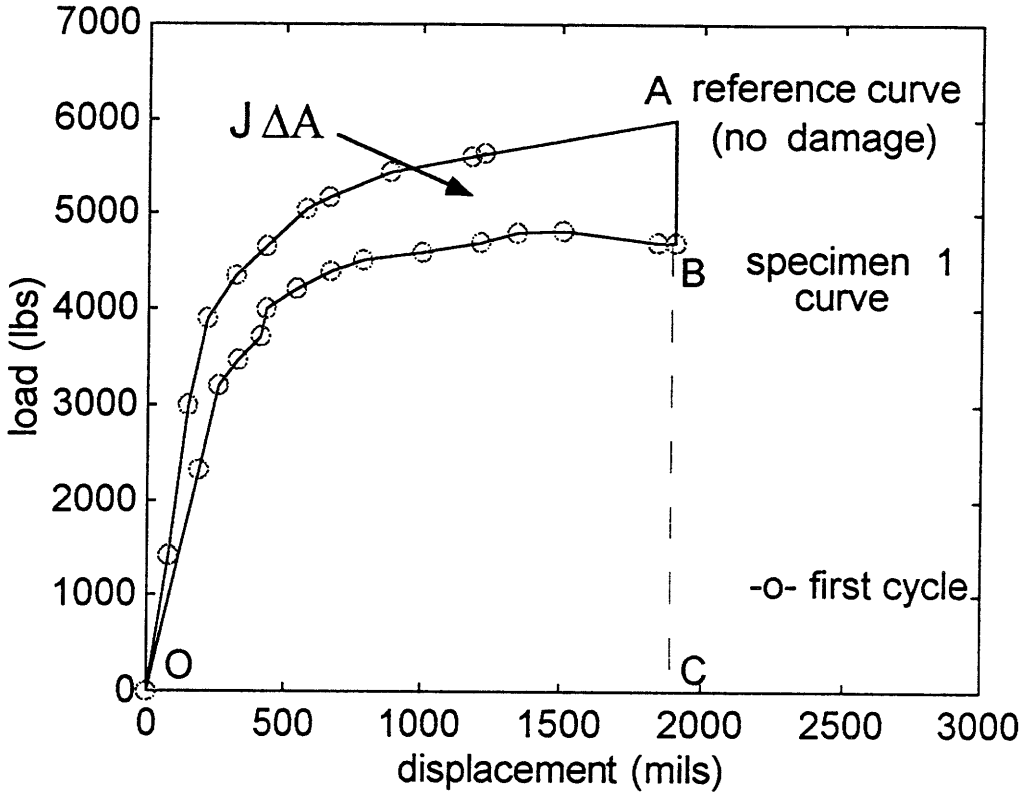

Figure 4.8 : Comparison of specimen 1 and specimen 4 load-displacement curves

Figure 4.9 : Specimen 1 fractured weld toe.

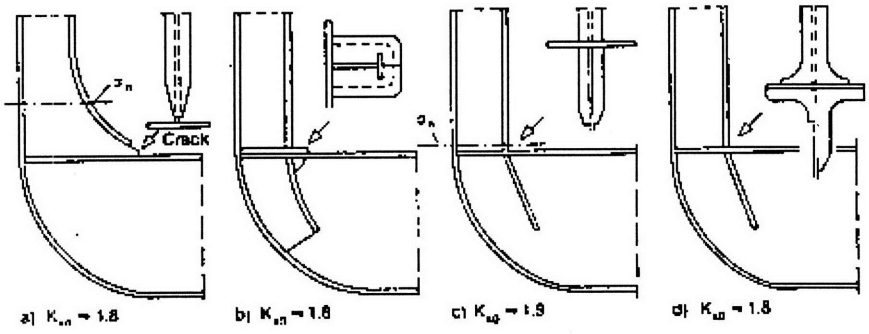

Figure 4.10 : Different configurations of a structural detail.

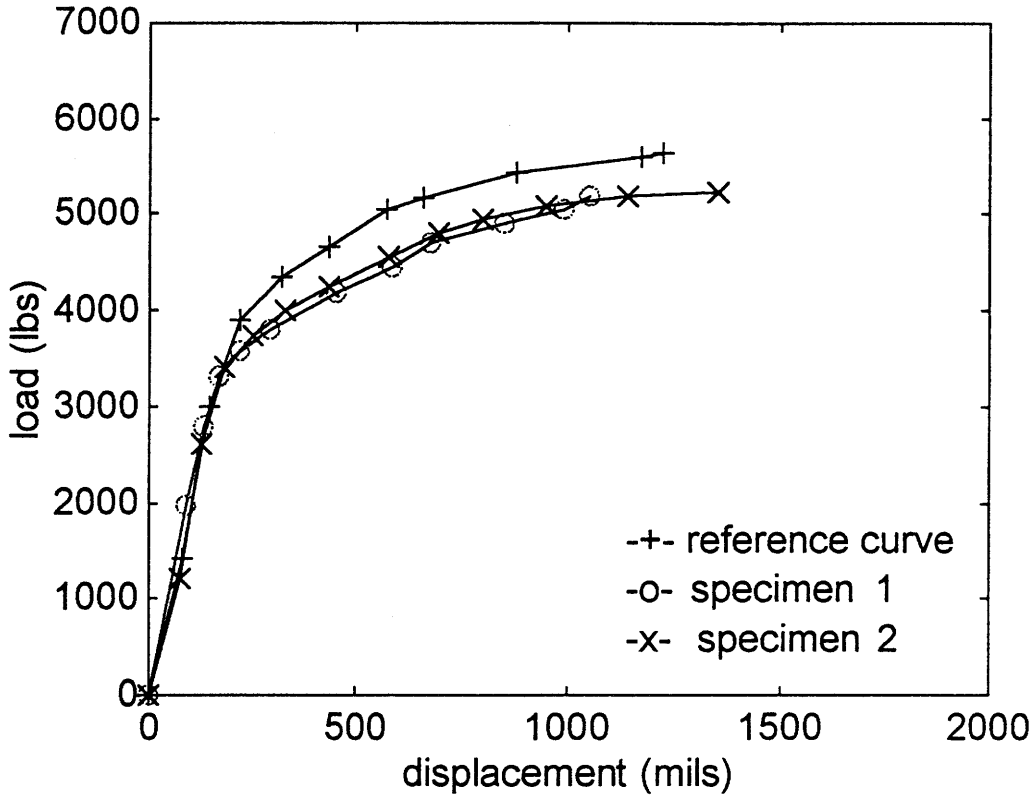

Figure 4.11 : Specimens 2 and 3 first cycle load-displacement curves compared with the reference response

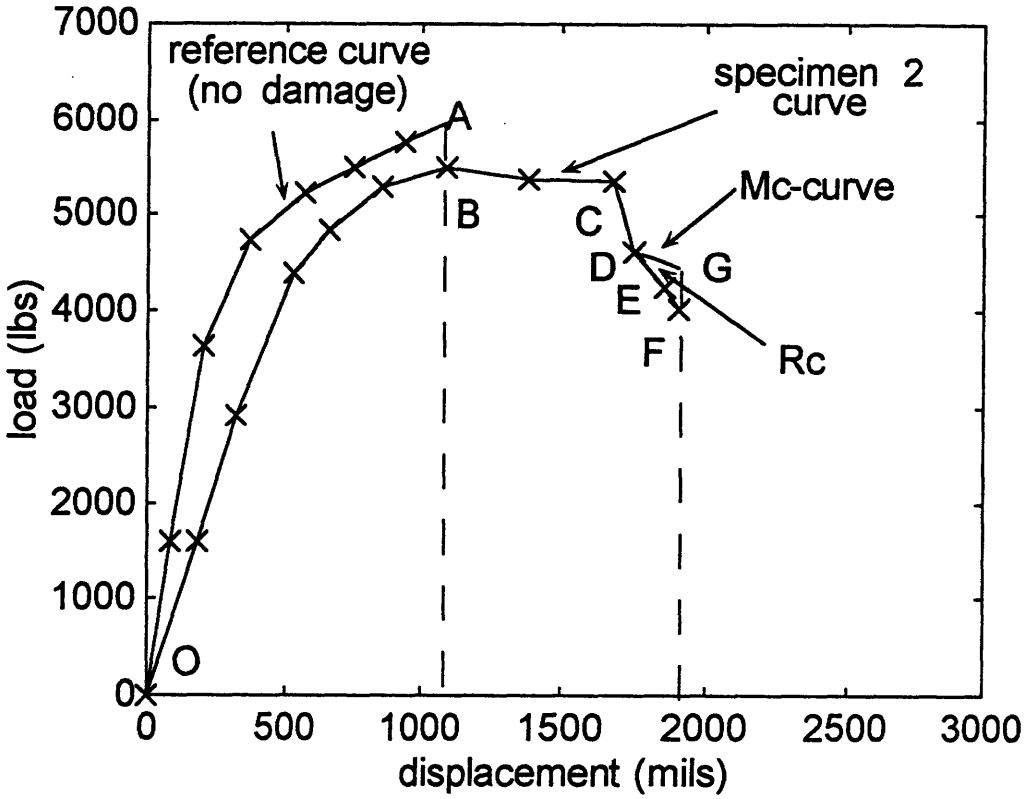

Figure 4.12 : Specimen 2 second cycle load-displament curve plotted together with the reference curve and the steady state constant moment curve.

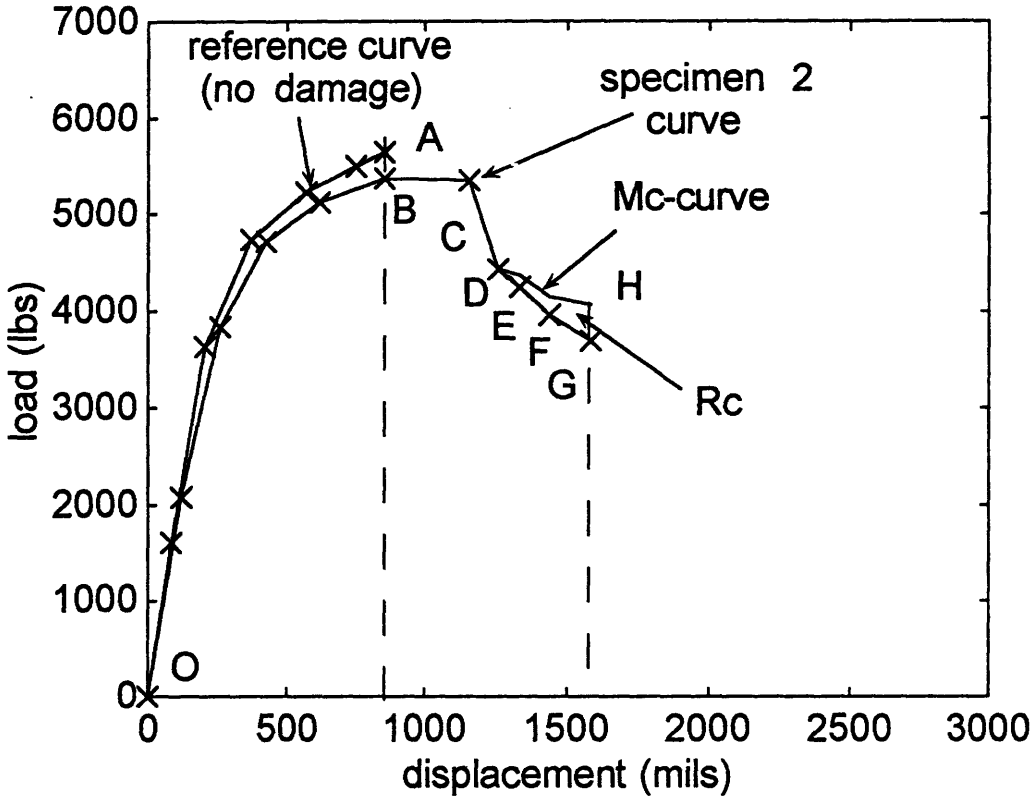

Figure 4.13 : Specimen 3 second cycle load-displament curve plotted together with the reference curve and the steady state constant moment curve.

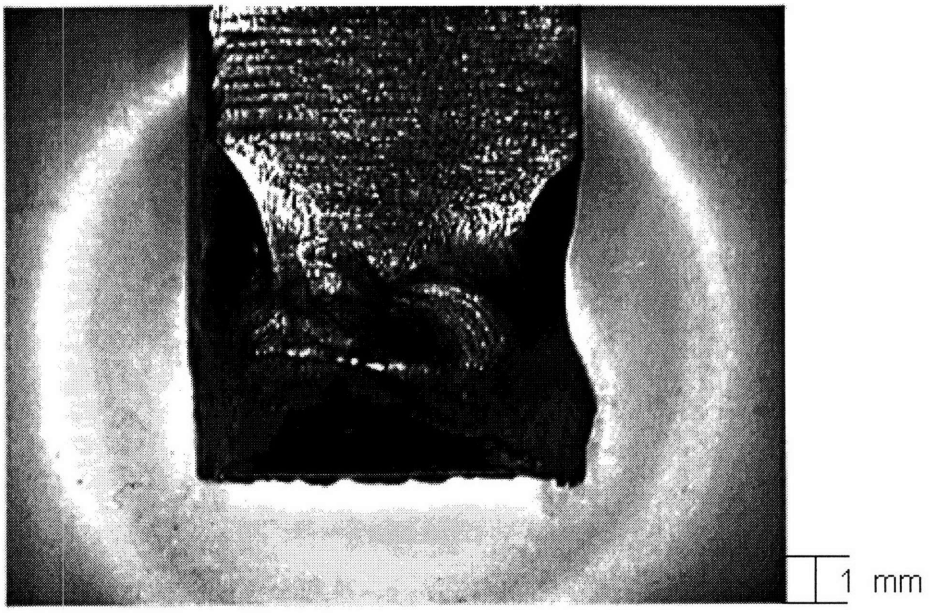

Figure 4.14 : General view of specimen 2 weld fractured surface.

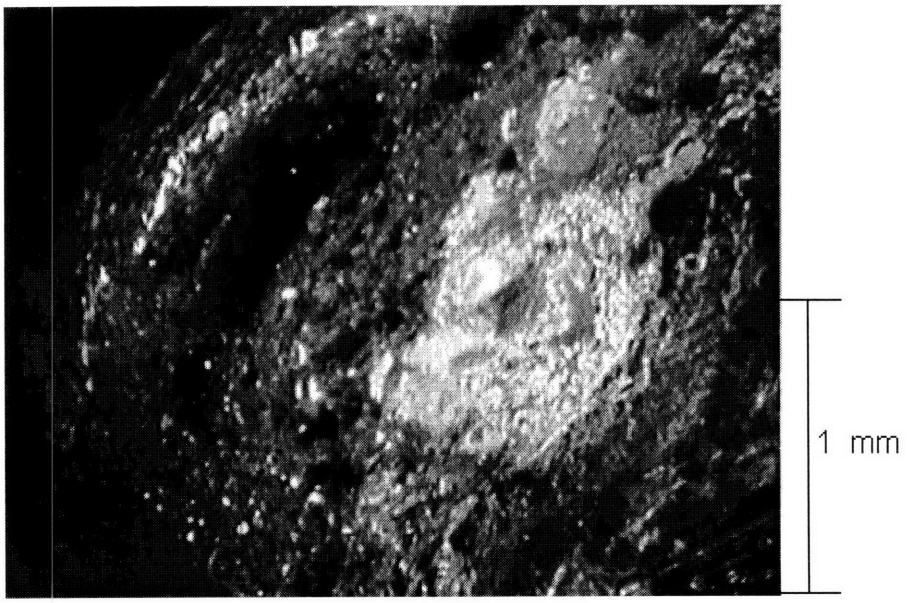

Figure 4.15 : Close view of specimen 2 weld fractured surface

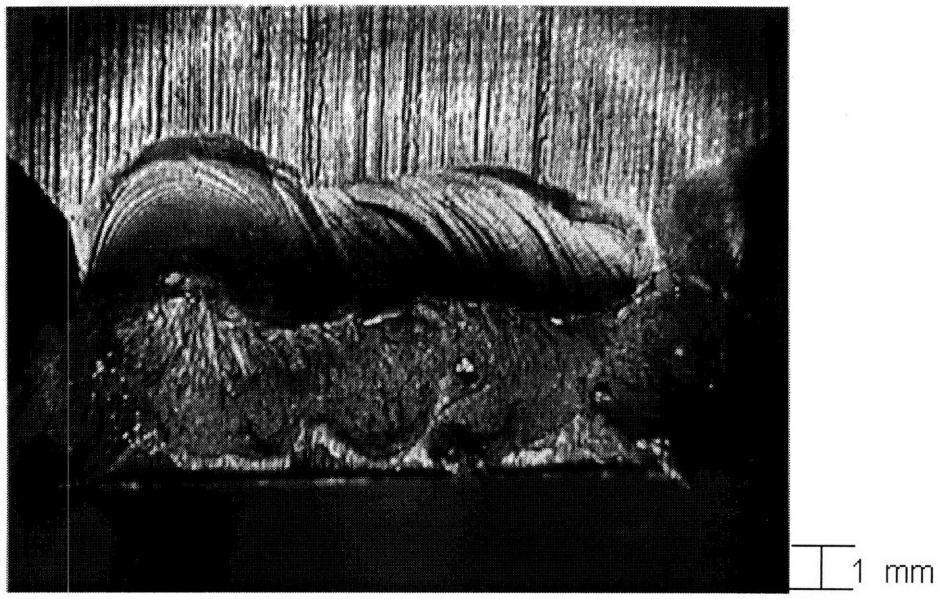

Figure 4.16 : General view of specimen 3 weld fractured surface.

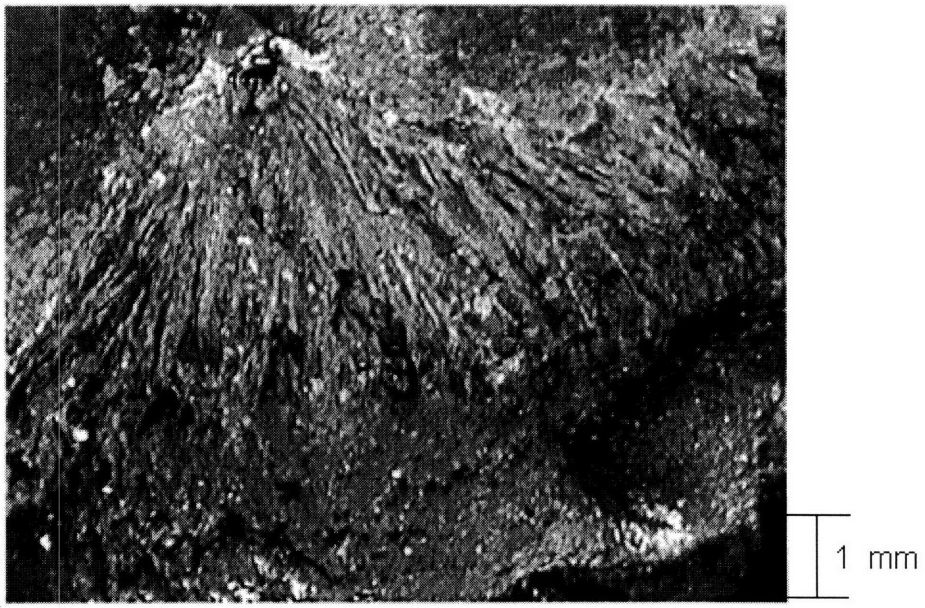

Figure 4.17 : Close view of specimen 3 weld fractured surface.

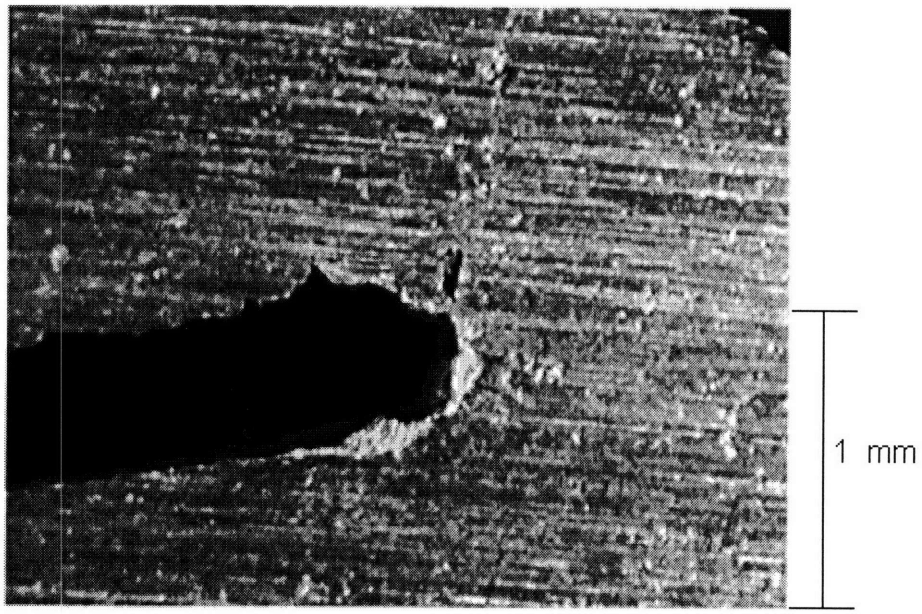

Figure 4.18 : Displacement of the web from the base plate for specimen 2.

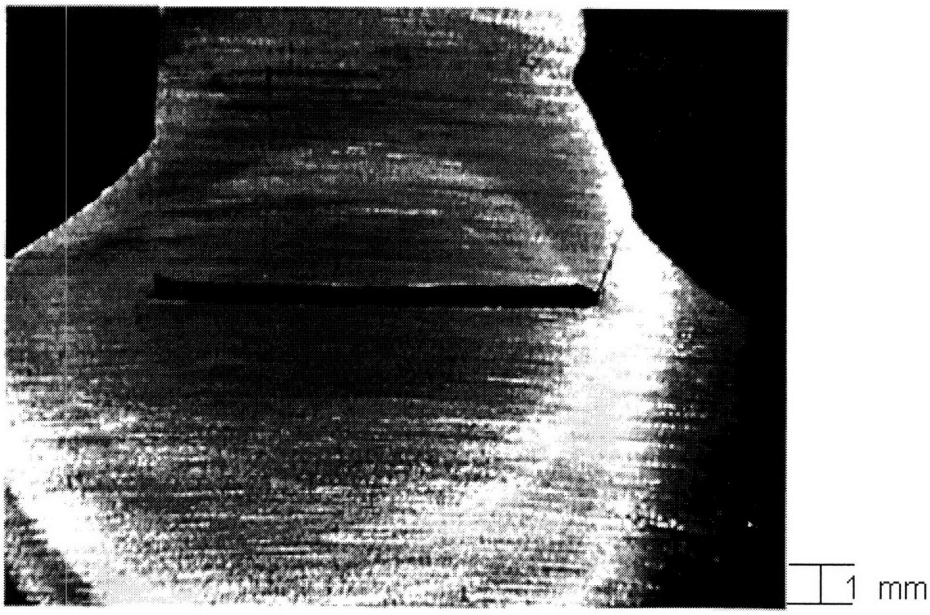

Figure 4.19 : Specimen 2 cross sectional view of the fillet weld after fracture

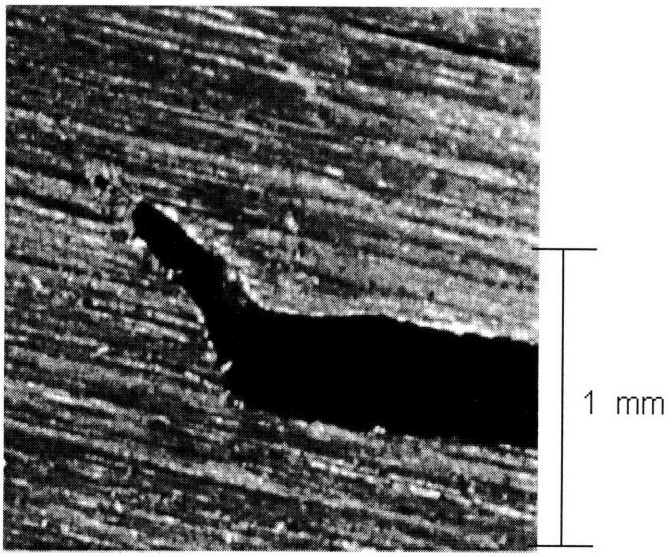

Figure 4.20 : Displacement of the web from the base plate for specimen 3.

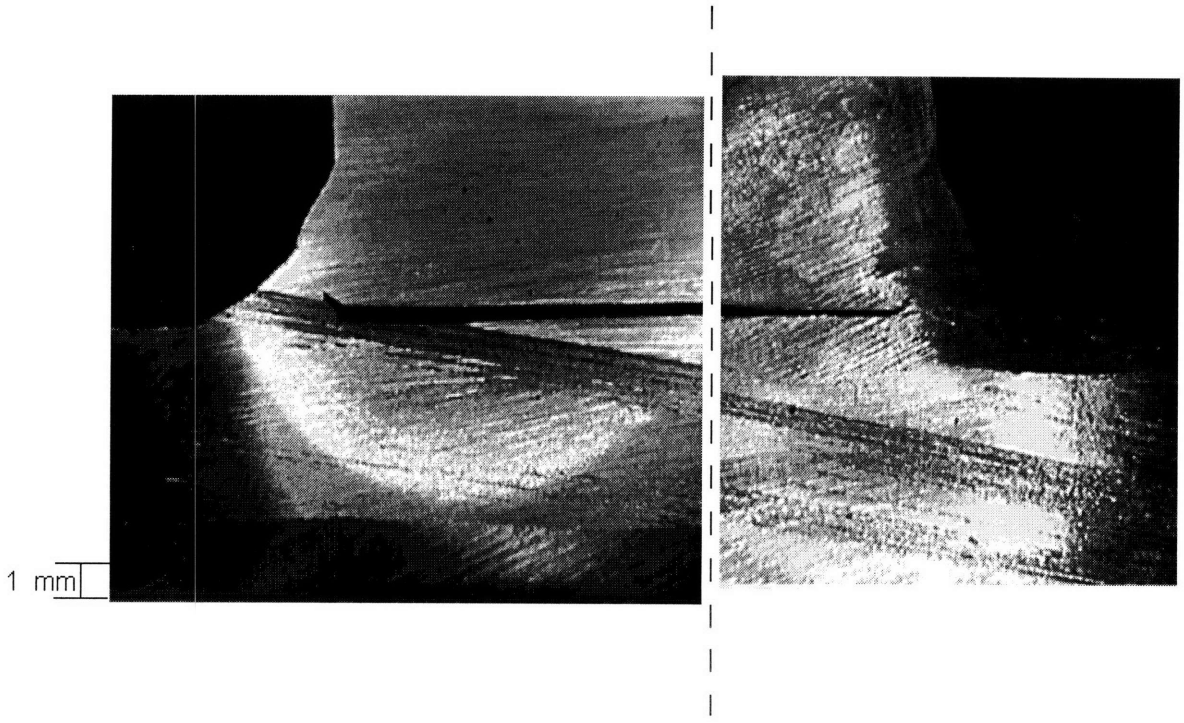

Figure 4.21 : Specimen 2 cross sectional view of the fillet weld after fracture.

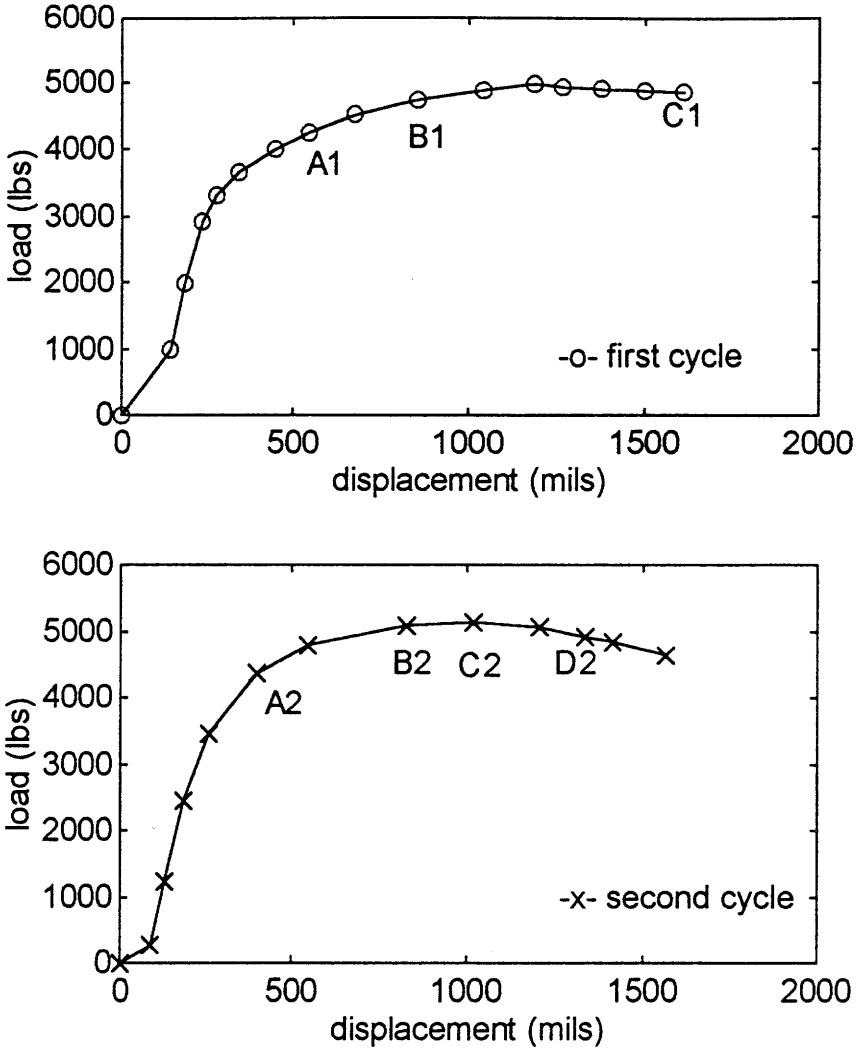

Figure 4.22 : Specimen 5 load-displacement curves

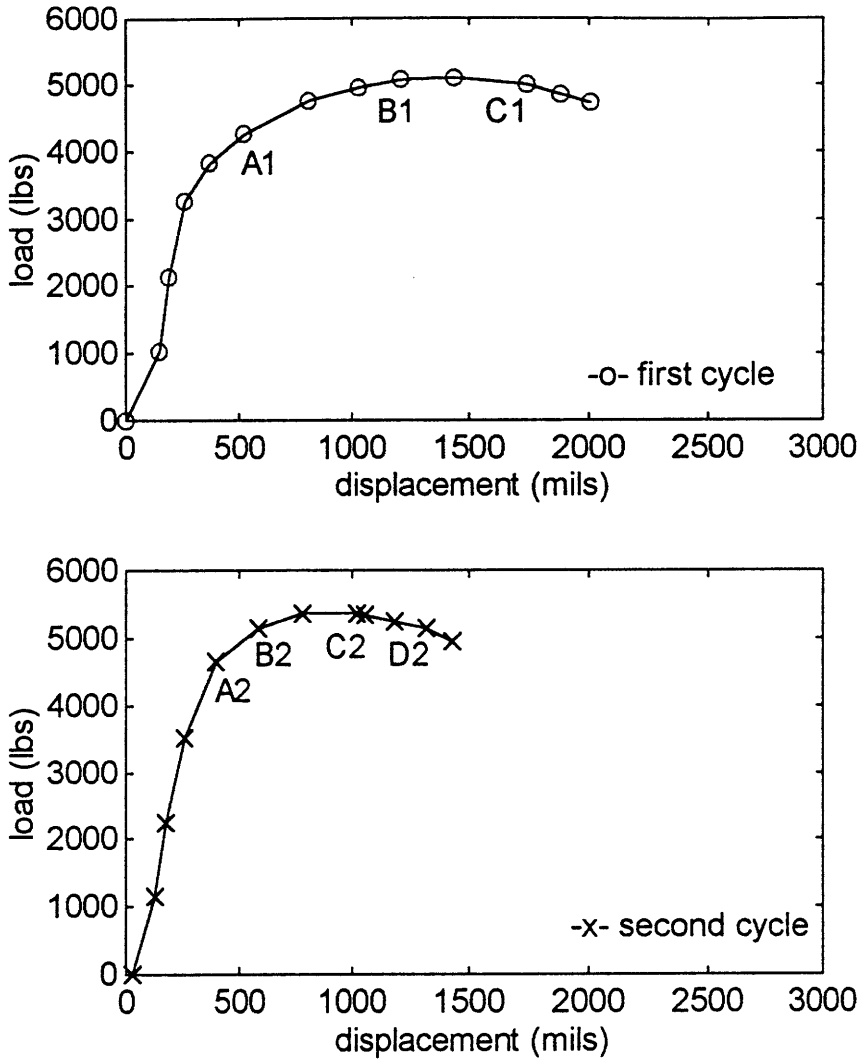

Figure 4.23 : Specimen 6 load displacement curves

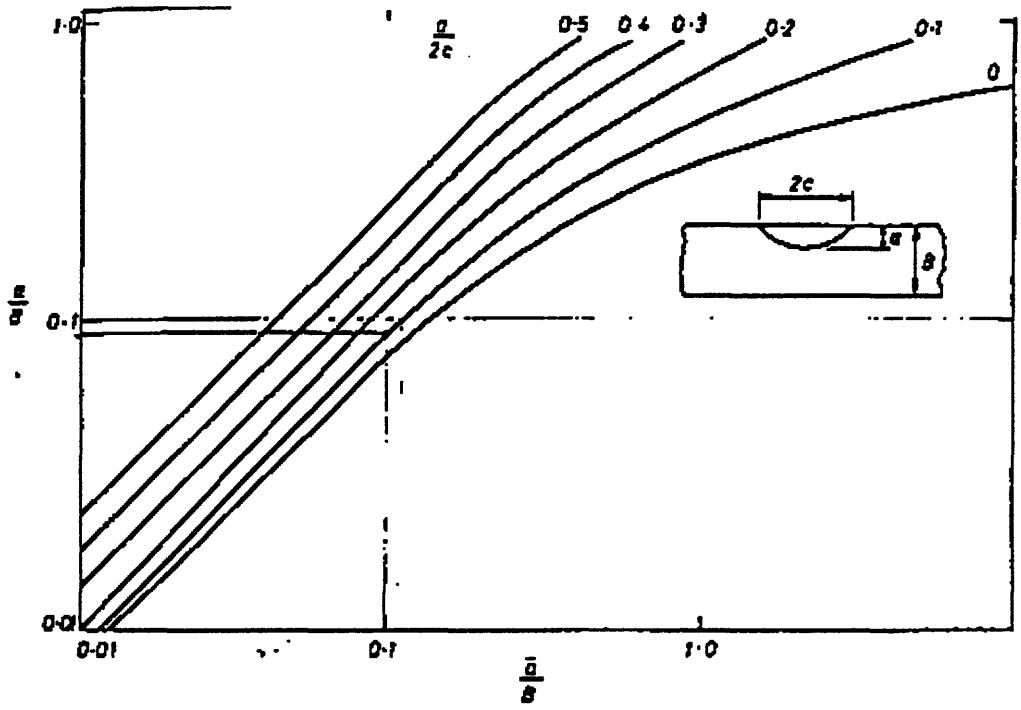

Figure 4.24 : Relationship between a surface crack dimensions and equivelant through thickness crack dimension [54].

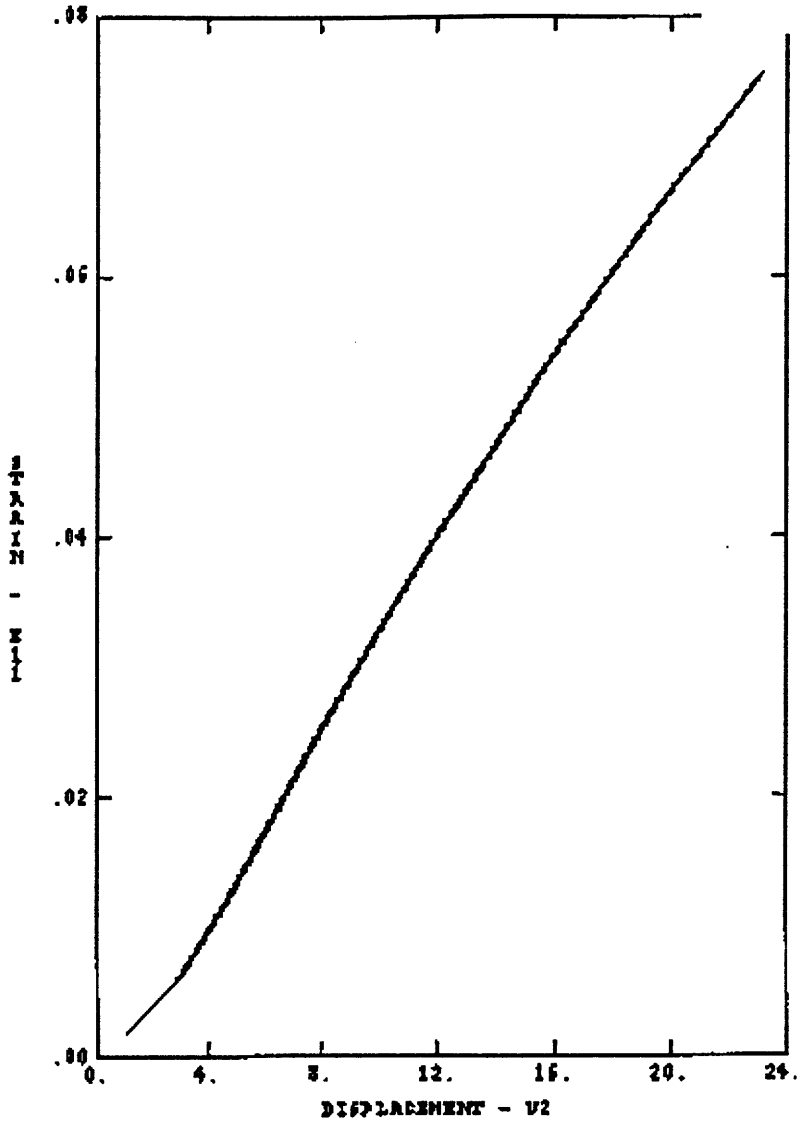

Figure 4.25 : Displacement vs nominal strain for the geometry of the experiments [56]

Conclusions and Future Work

From this work the following conclusions can be derived :

1. Two fracture modes can be identified to structural components with fillet welds when they are subjected to extensive plastic deformation: fracture of the base metal at the weld toe and peeling fracture of the fillet weld.

2. A structural component may withstand monotonic plastic deformation without fracture. This happens because the existence of a material flow stress does not permit strain concentration. Fracture will probably take place at the second cycle when the material exhibits a power law stress-strain behavior.

3. Strain concentration is created at the areas of stress concentration. Geometric configurations and weld defects that cause stress concentration reduce the ability of a structure to withstand alternating plasticity. Structural detail designs, that are adapted for better high cycle fatigue performance, will also exhibit high fracture resistance to very low cycle fatigue.

4. Considering the web-plate configuration, peeling fracture can be avoided, provided the weld at the end of the web remains always in the elastic range, even under repeated plastic deformation. Avoiding the initiation of fillet tearing, by making a strong weld only at that point, may permit the use of smaller fillet sizes at the rest of the web.

5. Surface cracks created during the welding procedure do not affect the fracture resistance of the structure, under extensive plasticity. Defects like undercuts and convexity are important for fracture at the toe of the weld because they cause strain concentration. Lack of fusion and incomplete penetration are important for the initiation of peeling fracture because they reduce the amount of weld metal at the fillet and consequently its strength.

6. As far as fracture remains ductile, crack arrest occurs outside the strain concentration area. Under impact loading, which takes place during a collision, brittle fracture is possible to occur when grade A steel is used. Structural designs that reduce the size of the stress concentration area will have smaller initial cracks and consequently smaller possibility for unstable fracture.

7. The capability of the video microscope to record real time fracture initiation and propagation, makes it an important tool in examining the material behavior and opens opportunities to the establishment of new experimental techniques. The information, obtained from the images taken by the video-microscope, was used to measure experimentally the tearing resistance of the fillet welds with satisfactory results. The use of existing formulas, for the calculation of the fracture work, failed because they are based on the assumption that the base plate material is elastic-perfectly plastic. This is not true for the case of cyclic loading.

8. The video-microscope has proven that it is portable, easily maneuverable in small spaces and needs no special skills to use. Therefore it can be used for on-site

structural inspections enhancing the capability of detecting small cracks. Fracture mechanics based life predictions and inspection intervals are based on the smallest detectable initial crack size. The use of the video-microscope would reduce that initial crack size and increase the time intervals between inspections. Moreover the ability to record the inspection would give the opportunity to a team rather than a person to evaluate a situation, which reduces the possibility for error.

The next steps that must be followed as a continuation of this work are :

1. Investigation of the importance of the membrane stresses. At real structures large membrane stresses are created at large plastic deformation. This happens because the supports at those structures resemble more the clamped boundary conditions. Therefore, it is believed that further investigation should be done using clamped specimens.

2. The effect of the strain rate on the performance of the fillet welds needs to be assessed. The difficulty to impose impact loading can be overcome by performing the experiments at equivalent low temperatures.

3. A numerical analysis of the experiment can be done, in order to calculate the size of the weld at the end of the web that is needed to avoid peeling fracture initiation.

References

1. Robert Taggart. *Ship Design and Construction.* SNAME, 1980.

2. Jordan, C. R., Cochran, C. S., *In-Service Performance of Structural Details.* SSC-272. Ship Structure Committee, 1978.

3. O. H. Burnside, S. J. Hudak, E. Oelkers, K. Chan, R. J. Dexter. *Long Term Corrosion Fatigue of Welded Marine Steels.* SSC-326. Ship Structure Committee, 1984.

4. Petershagen, H., Fatigue problems in ship structures. *Advances in Marine Structures.* C. S. Smith, R. S. Dow. Elsevier Applied Sciences, 1986.

5. Munse, W. H., Fatigue Criteria for Ship Structure Details. *Extreme Loads Response Symposium.* SNAME, 1981.

6. H. A. McDonald. *Required Strength and Tear Resistance for Fillet Welds in Ships Exposed to Grounding or Collision Loads.* M.S. Thesis, M.I.T. Department of Ocean Engineering, May, 1993.

7. Kunihiro Iida. Very low cycle fatigue life influenced by tensile or compressive prestrain. *Low Cycle Fatigue.* ASTM STP 942. H. T. Solomon, G.R. Halford, L. R. Kaisand, B. N. Leis. American Society for Testing and Materials, 1988.

8. Owen F. Hughes. *Ship Structural Design.* SNAME, 1988.

9. Bradley Dodd, Yilong Bai. *Ductile Fracture and Ductility*. Academic Press, 1987

10. D. Broek. Elementary Engineering Fracture Mechanics. Kluwer Academic Publishers, 1991.

11. T. L. Anderson. *Fracture Mechanics*. CRC Press, 1995.

12. Drar, H., On predicting the temperature and strain rate dependences of the fracture toughness of plain carbon steels. Materials Characterization, 31, 91-97. Elsevier Science Publishing Co, 1994.

13. H. O. Fuchs, R. I. Stephens. *Metal Fatigue in Engineering*. Wiley, 1980.

14. Djiubinski J. , Adamiec P., Brunne W. A Welded joint microstructure effect on low-cycle fatigue. *Low Cycle Fatigue and Elastoplastic Behavior of Materials*. K.-T.Rie. Elsevier Applied Science, 1987.

15. K. Shimada, J. Komotori, M. Shimizu. Fracture mode transition and damage in extremely low cycle fatigue. *Low Cycle Fatigue and Elastoplastic Behavior of Materials*. K.-T.Rie. Elsevier Applied Science, 1987.

16. Havas I., Czoboly E.. Effect of low-cycle fatigue on the brittle characteristics of a structural steel. *Low Cycle Fatigue and Elastoplastic Behavior of Materials*. K.-T.Rie .Elsevier Applied Science, 1987.

17. M. Schwartz, J. C. Crespi. Fracture of pearlite under conditions of high deformation fatigue. *Low Cycle Fatigue*. ASTM STP 942. H. T. Solomon, G.R. Halford, L. R. Kaisand, B. N. Leis. American Society for Testing and Materials, 1988.

18. B. N. Leis. A nonlinear history-dependent damage model for low cycle fatigue. *Low Cycle Fatigue.* ASTM STP 942. H. T. Solomon, G.R. Halford, L. R. Kaisand, B. N. Leis. American Society for Testing and Materials, 1988.

19. T. Kunio, M. Shimizu, N. Ohtani, T. Abe. Microstructural aspects of crack initiation and propagation in extremely low cycle fatigue. *Low Cycle Fatigue.* ASTM STP 942. H. T. Solomon, G.R. Halford, L. R. Kaisand, B. N. Leis. American Society for Testing and Materials, 1988.

20. T. Nakatsuji, T. Fujimori. A study on engineering critical assessment of weld defects in steel building constructions-Behavior of welded joints including weld defects under ultra-low cyclic large strain deformations. *Criteria For preventing Service Failure in Welded Structures.* The Third International Symposium of the Japan Welding Society, 1978.

21. Taijiro Nonaka, Satoshi Iwai. Failure of bar structures under repeated loading. *Structural failure*. Thomasz Wierzbicki, Norman Jones. Wiley, 1988.

22. Helmut Krawlinkler, Mahmud Zohrei. Cumulative damage in steel structures subjected to earthquake ground motions. Computers & Structures. Vol. 16, No 1-4. Pergamon Press, 1983.

23. Tsai, C. L., Itoga, K., Malliris, A. P., McCabe, W. C., Masubuchi, K., *Review of Fillet Weld Strength Parameters for Shipbuilding.* SSC-296. Ship Structure Committee, 1980.

24. R. P. Krumpen, Jr. and C. R. Jordan. *Updating of Fillet Weld Strength Parameters for Commercial Shipbuilding*. SSC-323. Ship Structure Committee, 1983.

25. Koichi Masubuchi. *Analysis of Welded Structures*. Pergamon Press, 1980.

26. Frank A. McClintock. *Fully Plastic Mechanics of Welded T-Joints*. Report 26, Joint MIT-Industry Program on Tanker Safety, 1994.

27. A. G. Atkins, Y.W. Mai. Residual strain energy in elastoplastic adhesive and cohesive fracture. *International Journal of Fracture*, 33:285-295, 1987.

28. Min Du Chang, K. L. Devries, M. L. Williams. The effects of plasticity in adhesive fracture. *Journal of Adhesion*. 4:221-231, 1972.

29. Yukito Hagiwara. Evaluation of brittle fracture strength from surface notch at fillet weld toe based on CTOD criterion. *J.S.N.A. Japan*. 157:223-232, 1985.

30. Susumu Machida, Hitoshi Yoshinari, Yukito Hagiwara. Study on fracture strength assessment. *J.S.N.A. Japan*. 171:113-126, 1992. Masakazu Onozuka, Osamu Ushirokawa, Yasushi Kumakura, Isamu Tsuji.

31. The influence of bead toe shapes on the fatigue strength of fillet welded joints-Fabrication acceptance criteria for undercut depth. *J.S.N.A. Japan*. 170,171:85-98, 1992.

32. X. Niu, G. Glinka. The weld profile effect on stress intensity factors in weldments. *International Journal of Fracture*, 35:3-20, 1987.

33. J. D. G. Sumpter. Fracture avoidance in submarines and ships. *Advances in Marine Structures-2.* C. S. Smith, R. S. Dow. Elsevier Applied Sciences, 1991.

34. J.D.G. Sumpter & A. J. Caudrey. Fracture toughness of Steel Plate from MV Kowloon Bridge. *Marine Structures.* Elsevier Science Limited, 6:443-460, 1993.

35. A. Kent Shoemaker. Fracture characteristics of steel under extremely high loading rates. *Extreme Loads Symposium.* SNAME, 1981.

36. J.D.G. Sumpter & A. J. Caudrey. Recommended fracture toughness for ship hull steel and weld. *Marine Structures.* Elsevier Science Limited, 8:345-357, 1995.

37. Takeshi Kanazawa, Susumu Machida, Hiroshi Yajima, Hajime Kawano. Study on brittle crack propagation and arrest behavior in plate and beam structures. *J.S.N.A. Japan*, 149:217-225,1981.

38. Hiroshi Yajima, Hajime Kawano, Yoshio Urabe. Study on brittle crack propagation and arrest behavior in plate and beam structures (Report II). *J.S.N.A. Japan*, 153:170-176, 1983.

39. Minorsky, V. U. An Analysis of Ship Collisions with Reeference to Protection of Nuclear Power Plants. *Journal of Ship Research*, 1959, 3, 1.

40. Jones, N. *A Literature survey on the Collision and grounding protection of ships.* SSC-283. Ship Structure Committee, 1979.

41. P. R. Van Mater, Jr., and J. G. Giannotti. *Critical Evaluation of Low-Energy ship Collision-Damage Theories and Design Methodologies. Vol I : Evaluation and Recommendation.* SSC-284. Ship Structure Committee,1979.

42. P. R. Van Mater, Jr., and J. G. Giannotti. *Critical Evaluation of Low-Energy ship Collision-Damage Theories and Design Methodologies. Vol II :Literature Search and Review.* SSC-284. Ship Structure Committee,1979.

43. J. Poudret, M. Huther, P. Jean, H. Vauhan. Grounding of a membrane tanker; correlation between damage predictions and observations. *Extreme Loads Response Symposium*. SNAME, 1981.

44. Jones N. Plastic Behavior of Ship Structures. *Trans. SNAME*, 84:115-145, 1976.

45. McDermott, J. F., Kline, R. J., Jones, E. L., Maniar, N. M., Chiang, W. P. Tanker Structural Analysis for Minor Collisions. *Trans. SNAME*, 82:382-414, 1974.

46. Wierzbicki, T., Peer, D.B., Rady, E., The Anatomy of Tanker Grounding. Marine Technology, 30,2 71-78, 1993.

47. Egge, E. D., Bockenhauer, M. Calculation of the collision resistance of ships and its assessment for classification purposes. *Marine Structures*, 4:35-56. Elsevier Science Publishers, 1991.

48. Preben Terndrup Pedersen. Ship Grounding and Hull-Girder Strength. *Marine Structures*, 7:1-29. Elsevier Science Publishers, 1994.

49. Jones, N., On the dynamic inelastic failure of beams. *Structural failure*. Thomasz Wierzbicki, Norman Jones. Wiley, 1988.

50. Duffey, T. A., Dynamic rupture of shells. *Structural failure*. Thomasz Wierzbicki, Norman Jones. Wiley, 1988.

51. Gifford, L. N., Dally, J.W., Dynamic fracture resistsnce of metal structures loaded into the plastic regime. *Advances in Marine Structures-2*. C. S. Smith, R. S. Dow. Elsevier Applied Sciences, 1991.

52. Dieter Radaj. *Design and Analysis of Fatigue Resistant Welded Structures*. Abington Publishing, 1990.

53. Daniel J. Maykuth, Ed. *Structural Alloys Handbook*. Mechanical Properties Data Center, Battelle Columbus Laboratories, 1980.

54. J. D. Harrison. Application of fracture mechanics in the prevention of service failures. *Criteria For preventing Service Failure in Welded Structures*. The Third International Symposium of the Japan Welding Society, 1978.

55. Kardomateas, G. A. *Mixed mode I and II fully plastic crack growth from simulated weld defects*. PHD thesis, MIT, 1985.

Appendix A

Literature survey in very low cycle fatigue

Djiubinski J. , Adamiec P., Brunne W. A Welded joint microstructure effect on low-cycle fatigue. *Low Cycle Fatigue and Elastoplastic Behavior of Materials*. K.-T.Rie. Elsevier Applied Science, 1987.

The effect of microstructure of joints welded by different methods is investigated. It has been found that low cycle fatigue strength of welded joints depends mostly on volume fraction of non-metallic inclusions which are stress concentrators lowering cyclic plasticity. The welded joint microstructure has a lesser effect on low cycle fatigue. The lowest cyclic plasticity is revealed by MMA joints, slightly higher by SA joints and the highest by ES joints.

K. Shimada, J. Komotori, M. Shimizu. Fracture mode transition and damage in extremely low cycle fatigue. *Low Cycle Fatigue and Elastoplastic Behavior of Materials*. K.-T.Rie. Elsevier Applied Science, 1987.

The study investigates the characteristics of the fatigue life of annealed low carbon steal and of pure iron at the extremely low cycle fatigue regime where transition from surface to internal fracture modes occur. Results show that in this regime the final fracture of the low carbon steel occurs at a strain cycle count less than that predicted by the Man-

son-Coffin law for an ordinary low cycle fatigue regime. The difference exists because in ordinary low cycle fatigue the fracture occurs from the development of small surface cracks whereas in the extremely low cycle regime fatigue life is reduced by the cracking of the pearlite inside the material. The applicability of the Manson-Coffin and Miner's laws is also investigated.

Havas I., Czoboly E.. Effect of low-cycle fatigue on the brittle characteristics of a structural steel. *Low Cycle Fatigue and Elastoplastic Behavior of Materials*. K.-T.Rie .Elsevier Applied Science, 1987.

By testing cylindrical notched specimens it was found that plastic pre-cycling can decrease substantially the fracture toughness of a material. The reason for this is believed to be the decreasing volume of plastically deformed material in the notch root.

M. Schwartz, J. C. Crespi. Fracture of pearlite under conditions of high deformation fatigue. *Low Cycle Fatigue*. ASTM STP 942. H. T. Solomon, G.R. Halford, L. R. Kaisand, B. N. Leis. American Society for Testing and Materials, 1988.

The aim of the work was to study the relationship between the stress and strain amplitudes under controlled strain conditions, the hardening and softening caused by fatigue and the fatigue life resistance properties of fully annealed SAE 1038 steel, and to attempt to apply the Kettunen and Kocks approach to polycrystalline materials where a second phase is present. Among other they found that at strain amplitudes greater than 0.37% instantaneous strain hardening is observed and a saturation value for the stress amplitude is not clearly defined.

B. N. Leis. A nonlinear history-dependent damage model for low cycle fatigue. *Low Cycle Fatigue.* ASTM STP 942. H. T. Solomon, G.R. Halford, L. R. Kaisand, B. N. Leis. American Society for Testing and Materials, 1988.

A nonlinear damage postulate that embodies the dependence of the damage rate on cycle-dependent changes in the bulk microstructure and the surface topography is examined. The major conclusion of this study is that the sequence dependence of damage is tied, through the bulk mechanical properties to the microstructure. History dependence in deformation response leads to history dependence of fatigue resistance. It follows then that damage mechanics and constitutive behavior are explicitly related, at least in the short-life domain controlled by the bulk.

Kunihiro Iida. Very low cycle fatigue life influenced by tensile or compressive prestrain. *Low Cycle Fatigue.* ASTM STP 942. H. T. Solomon, G.R. Halford, L. R. Kaisand, B. N. Leis. American Society for Testing and Materials, 1988.

The effects of excessive prestrain in tension or in compression upon very low-cycle fatigue life were investigated for two mild steels and two high strength steels as an aid for the analysis of a ship failure in service, in which the bow structure was broken off due to local buckling and by low cycle fatigue in extremely heavy sea conditions. It was found that the residual static fracture ductility decreases as a function of the amount of prestrain, showing much more loss in ductility in the case of compressive prestrain. Fairly good agreement between experimental data and Manson's and Iida's formulae was found. The failure life of the specimen subjected to prestrain showed remarkable de-

crease from the failure life of the original material depending on three parameters: amount of prestrain, direction of prestrain, and specimen surface conditions. The worst case at the tests performed was tensile prestraining directly followed by strain cycling.

T. Kunio, M. Shimizu, N. Ohtani, T. Abe. Microstructural aspects of crack initiation and propagation in extremely low cycle fatigue. *Low Cycle Fatigue.* ASTM STP 942. H. T. Solomon, G.R. Halford, L. R. Kaisand, B. N. Leis. American Society for Testing and Materials, 1988.

A study has been made of the crack initiation and propagation in a low cycle fatigue of annealed carbon steel including extremely short fatigue life ($N_f < 100$), with an emphasis on the establishment of the relation between the microfracture behavior and the damage accumulation process depending on the plastic strain range, $\Delta\varepsilon_p$, as well as the mean strain, ε_m. It was found that at the small $\Delta\varepsilon_p$ the surface damage due to the initiation and propagation of surface microcracks is predominant, while at the very large $\Delta\varepsilon_p$ giving life less than $N_f = 10$, the internal cracking originated from the fracture of a pearlite becomes a primary source of the damage which results in the reduction of the residual ductility, ε_{FR}. The transition from the surface damage to the internal one takes place when $\Delta\varepsilon_p$ becomes so large that the pearlite cracking may start inside the material at each level of ε_m.

T. Nakatsuji, T. Fujimori. A study on engineering critical assessment of weld defects in steel building constructions-Behavior of welded joints including weld defects under ultra-low cyclic large strain deformations. *Criteria For preventing Service Failure in Welded Structures*. The Third International Symposium of the Japan Welding Society, 1978.

This report is concerned with a test and analysis of crack propagation and total number of loading alternations including plane defects such as weld crack or incomplete penetration when they are subjected to a cyclic loading with large strain of a degree that they might suffer at the time of an earthquake. It was concluded that a welded joint having plane defects such as incomplete penetration is subjected to a large cyclic strain, cracks on it propagate from this defects, that may bring about failure of the weld joint by some to several tens of cycles. A crack propagation length calculated by using strain distribution ahead of the crack tip on the assumption that a crack propagates to the point that the accumulated equivalent strain reaches a certain amount, was in good agreement with a value obtained from the experiment.

Taijiro Nonaka, Satoshi Iwai. Failure of bar structures under repeated loading. *Structural failure*. Thomasz Wierzbicki, Norman Jones. Wiley, 1988.

Structural failure due to the repeated action of loads is discussed after classification into three types: continued plastic deformation, instability due to changes in geometry, and structural fatigue. Various aspects of plastic failure due to variable repeated loads are discussed on the basis of the classical theory of perfect plasticity as it applies to a simple-truss example. Next, consideration is given to an interactive phenomenon between

plasticity and geometrical change, causing hysteretic instability on an axially and repeatedly loaded bar member. Finally, a literature survey is presented on experimental aspects of low cycle fatigue from the point of view of overall structural failure behavior.

Helmut Krawlinkler, Mahmud Zohrei. Cumulative damage in steel structures subjected to earthquake ground motions. Computers & Structures. Vol. 16, No 1-4. Pergamon Press, 1983.

Experimental data are presented from low cycle fatigue tests of structural steel components. In these tests the failure modes of local buckling in beam flanges and fracture at weldments were studied in detail. Cumulative damage models are proposed which permit a life prediction for arbitrary cyclic loading histories. Crack propagation at weldments is modeled with a crack growth rate model based on the plastic strain range. Adequate predictions of lives were obtained from the analytical models.

Appendix B

HIROX-Hi-Scope Video Microscope

The Hi-Scope KH-2200 Video Microscope System is a combination of the long history of microscopy and the recent advances in CCD camera technology. The fusion of these optical fields allows the user to easily inspect minute details in ways not possible with conventional microscopes or visual inspection equipment.

The main control unit is the light source and controls the camera functions. The camera unit holds the camera and accepts interchangeable lenses. The lenses allow the user to change magnifications. The lenses accept adapters that vary the working distance , lighting style, and viewing angle. The main unit is connected to the camera via a fiber optic lighting cable and a camera cable. The main control unit also connects to a video monitor to display the image, and to other video devices for storage and manipulation. The versatility of the lenses and adapters that could be used enables the video microscope to be applicable and various fields such as:

- Dermatology
- Consumer goods
- Pharmaceuticals

- Biology
- Police Departments
- Metallurgy
- Mechanical Engineering
- Electrical Engineering
- Chemical Engineering

Especially in Metallurgy which is the application of our interest, the videoscope may give images of surface details comparable to those of a scanning electron microscope. Also it can be used to view metal with nearly perfect vertical lighting, thus doing the job as a metal microscope performing "bright field" imaging.

The main advantages of the video microscope are:

- **Hand-held.** With the Hi-Scopethe sample can be kept where it is, while the optical head is moved to the whole sample. Hi-Scope requires no slicing, polishing, or other processing preparation before viewing the sample.
- **Video System.** Hi-Scope is a video system and the image can be observed on a video monitor. This means the image can be easily saved, printed, or analyzed with suitable processing systems.
- **Continuously Variable Lighting Angle.** According to the application used the lighting angle can be changed for optimum results.

- **Great Depth of Field.** Hi-Scope's depth of field is 10 to 20 times that of a binocular microscope which allows almost a three dimensional viewing.

- **Wide Range of Lenses.** With the Hi-Scope System there is a choice of magnification lenses from less than true size to 1600x. There is also a zoom lens with continuous focus of 20 to 100x.

- **Wide Range of Adapters.** Various adapters are offered to fit the needs of any application.

- **Automatic Lighting Control.** The System features automatic lighting control to ensure optimum lighting instantly.

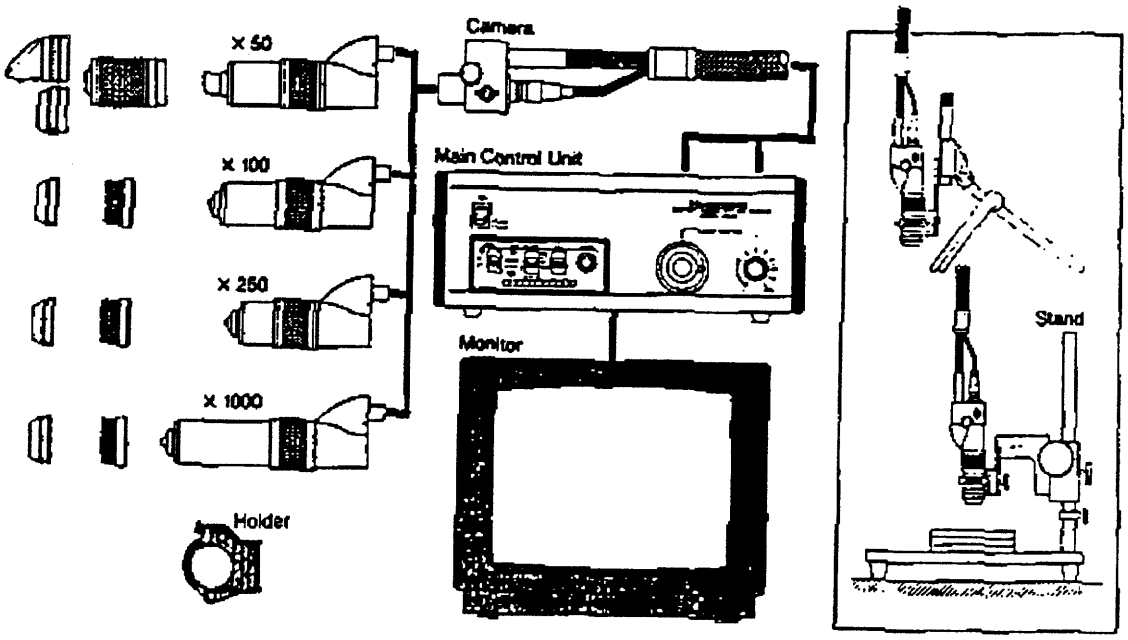

Video-microscope general set-up

Appendix C

Load-displacement data

Specimen 1

LOAD (LBS)	DISPLACEMENT (MILS)
0	0
189	2320
255	3200
323	3460
408	3720
429	4000
538	4200
667	4400
782	4520
1001	4600
1211	4700
1345	4800
1513	4820
1846	4700
1907	4700

Specimen 2

FIRST CYCLE

LOAD (LBS)	DISPLACEMENT (MILS)
0	0
1980	90
2800	129
3300	167
3580	219
3800	290
4180	452
4460	585
4700	679
4900	855
5060	995
5190	1052

SECOND CYCLE

LOAD (LBS)	DISPLACEMENT (MILS)
0	0
1600	180
2920	316
4400	525
4840	658
5300	850
5500	1085
5380	1385
5360	1685
4620	1753
4240	1855
4020	1905

Specimen 3

FIRST CYCLE

LOAD (LBS)	DISPLACEMENT (MILS)
0	0
1220	75
2600	126
3400	181
3740	248
4000	327
4240	433
4560	578
4800	698
4940	803
5100	950
5200	1143
5240	1352

SECOND CYCLE

LOAD (LBS)	DISPLACEMENT (MILS)
0	0
2080	120
3840	258
4720	420
5140	616
5380	853
5360	1155
4440	1258
4250	1340
3960	1440
3700	1588

Specimen 4

FIRST CYCLE

LOAD (LBS)	DISPLACEMENT (MILS)
0	0
1420	78
3000	143
3900	218
4360	320
4660	433
5040	575
5180	660
5440	880
5600	1175
5640	1225

SECOND CYCLE

LOAD (LBS)	DISPLACEMENT (MILS)
0	0
1600	85
3640	202
4740	370
5240	567
5500	750
5760	935

THIRD CYCLE

LOAD (LBS)	DISPLACEMENT (MILS)
0	0
1980	125
3400	212
4480	350
4960	473
5320	690
5620	1038

Specimen 5

FIRST CYCLE

LOAD (LBS)	DISPLACEMENT (MILS)
0	0
1000	144
1980	185
2910	237
3300	276
3650	340
3990	446
4235	543
4510	678
4750	860
4900	1045
5000	1189
4945	1267
4910	1376
4900	1499
4875	1614

SECOND CYCLE

LOAD (LBS)	DISPLACEMENT (MILS)
0	0
270	89
1230	128
2440	185
3450	258
4380	399
4780	545
5080	832
5125	1020
5070	1206
4925	1336
4850	1415
4650	1565

Specimen 6

FIRST CYCLE

LOAD (LBS)	DISPLACEMENT (MILS)
0	0
1035	147
2130	187
3250	259
3825	369
4255	519
4740	803
4950	1022
5060	1210
5100	1439
5000	1743
4850	1886
4720	2008

SECOND CYCLE

LOAD (LBS)	DISPLACEMENT (MILS)
0	27
1160	128
2255	175
3520	253
4650	394
5150	581
5355	778
5360	1019
5330	1053
5250	1183
5140	1325
4950	1431

Appendix D

Crack observation

The crack initiation and propagation during the loading of specimens 2, 3, 5 and 6 was recorded using the video microscope. From the recorded tape, still images were obtained. Those images are shown in the following pages.

Each photo corresponds to a point of the load-displacement curves shown in figure 4.12 for specimen 2, figure 4.13 for specimen 3, figure 4.22 for specimen 5 and fiure 4.23 for specimen 6. This point is indicated at the legend of each picture. For specimens 2 and 3 each picture is accompanied with a drawing showing the stage of the crack propagation.

Specimen 2

Point definition

Point	Load (lbs)	Displacement (mils)	Crack length (mm)
B	5380	135	initiation
C	5360	1685	initiation
D	4620	1753	4
E	4240	1855	6.5
F	4020	1905	8.5

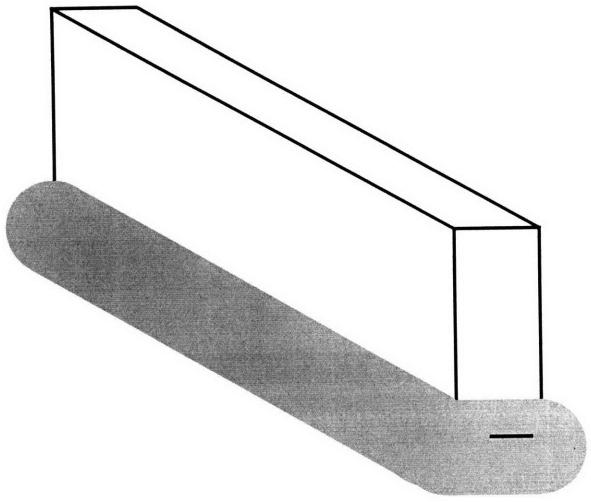

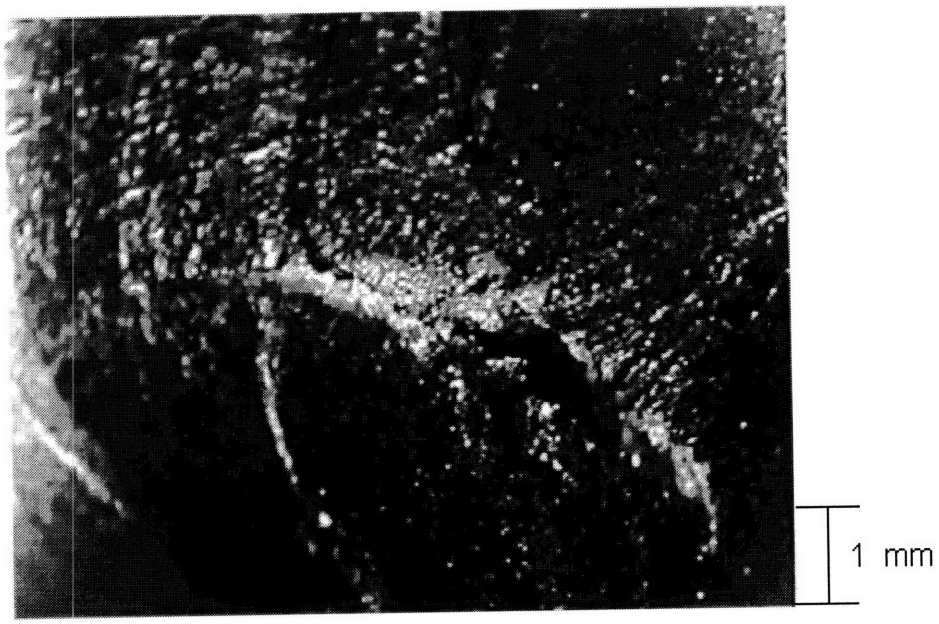

Crack initiation (B)

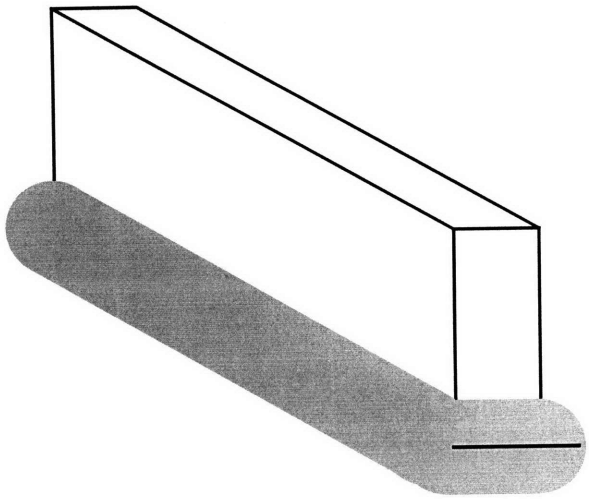

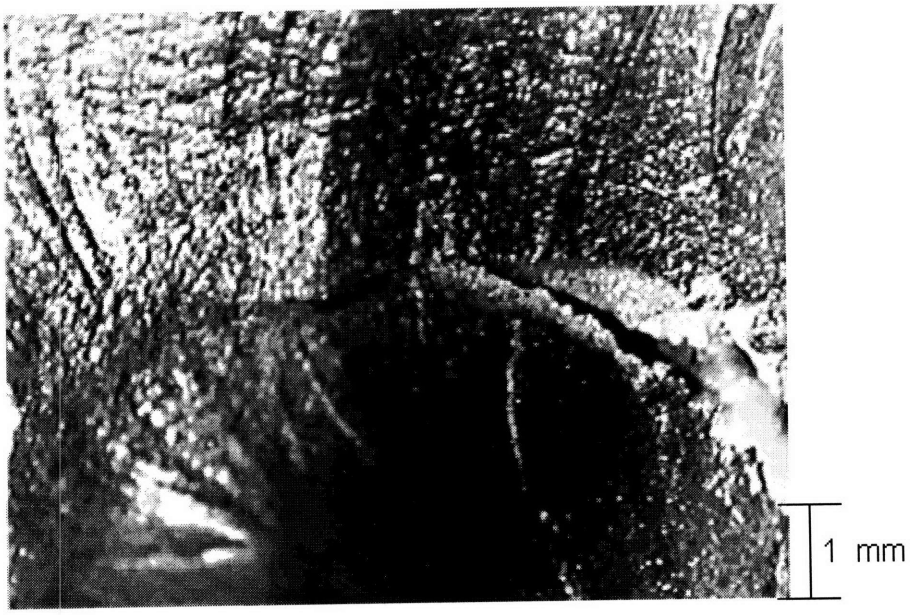

Transverse crack propagation and transition from transverse to longitudinal cracking (C)

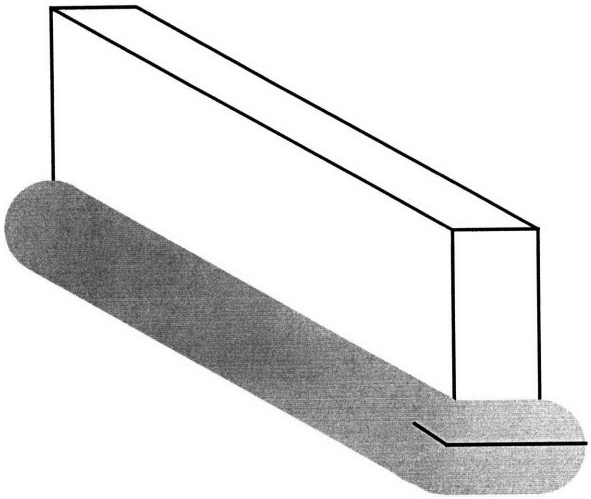

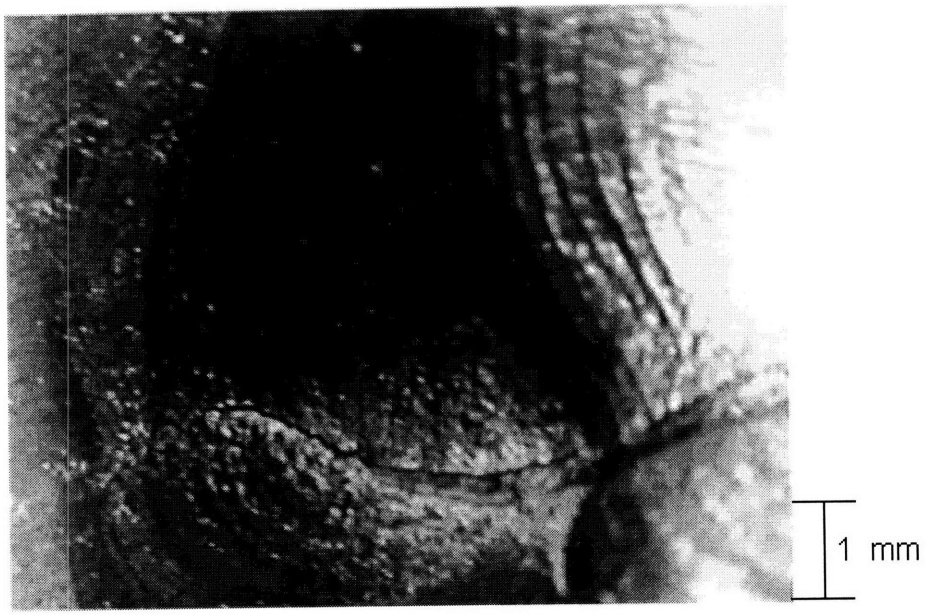

Initiation of steady state peeling fracture (D)

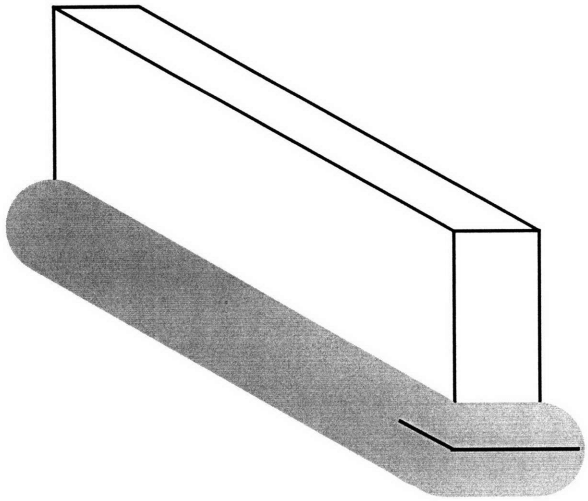

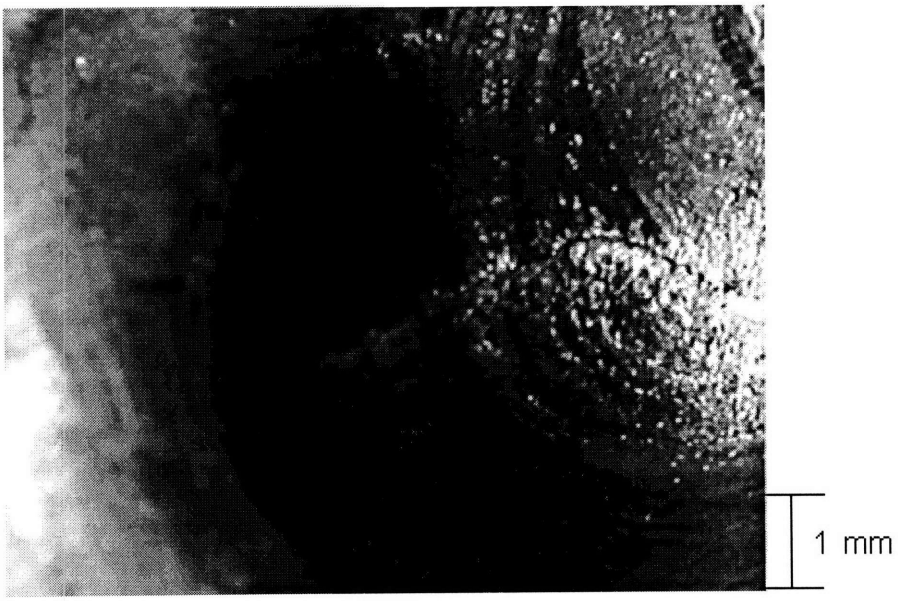

Crack propagation along the weld bead (E)

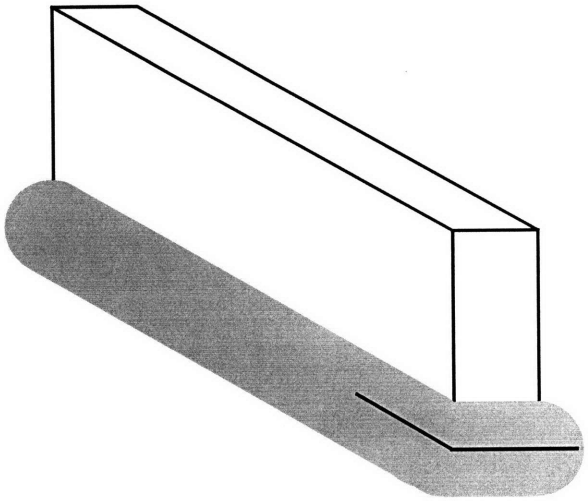

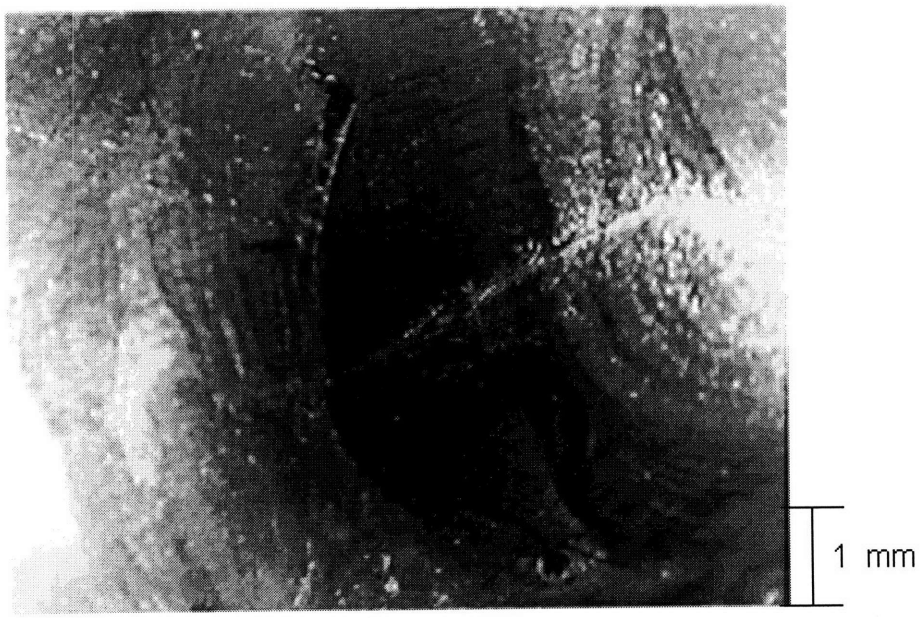

Final stage of crack propagation (F)

Specimen 3

Point definition

Point	Load (lbs)	Displacement (mils)	Crack length (mm)
B	5380	853	initiation
C	5360	1155	initiation
D	4440	1258	2
E	4360	1340	4
F	3860	1440	10.5
G	3700	1588	12.5

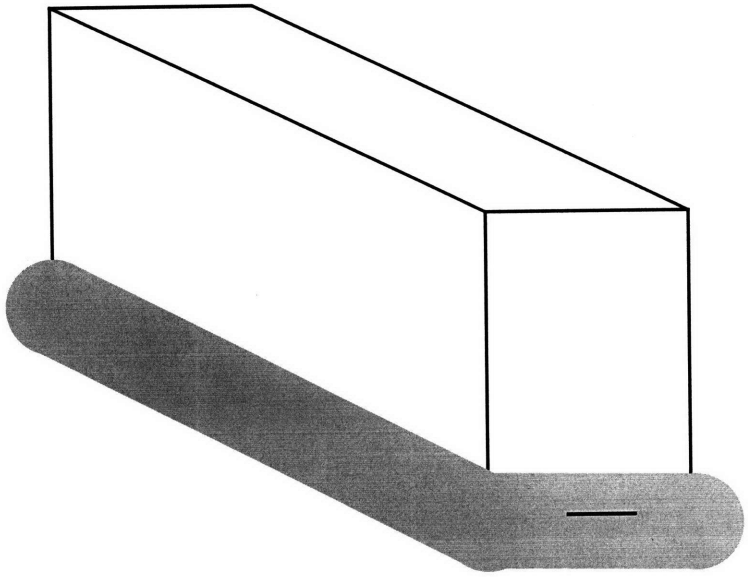

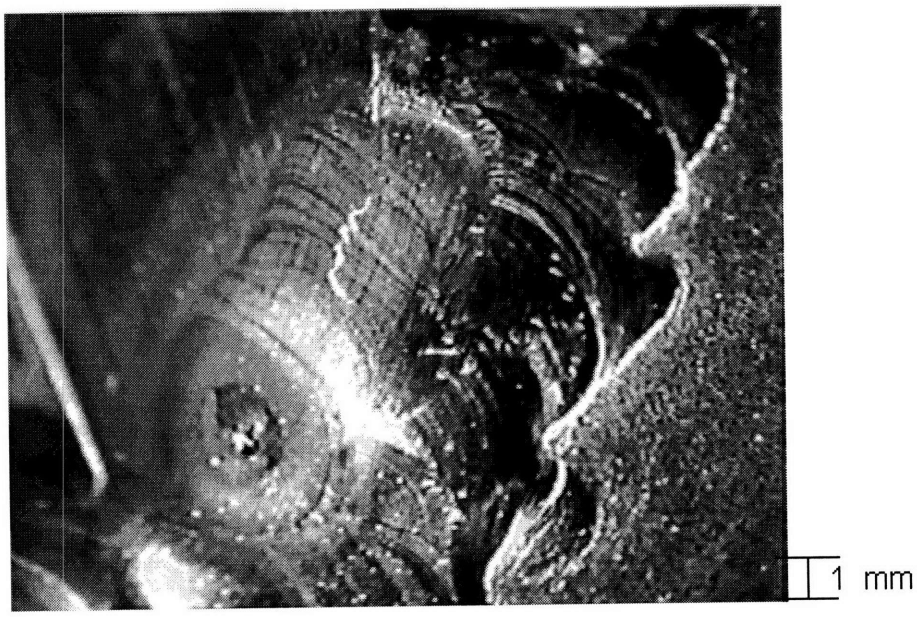

Crack initiation (B)

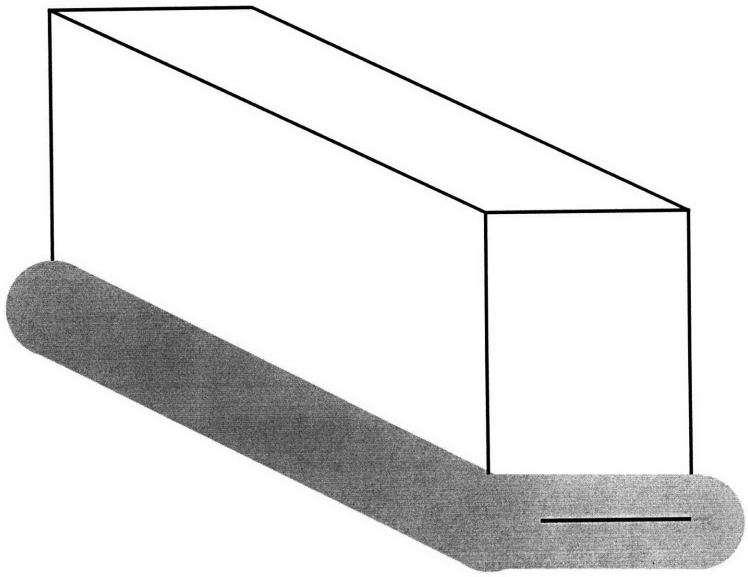

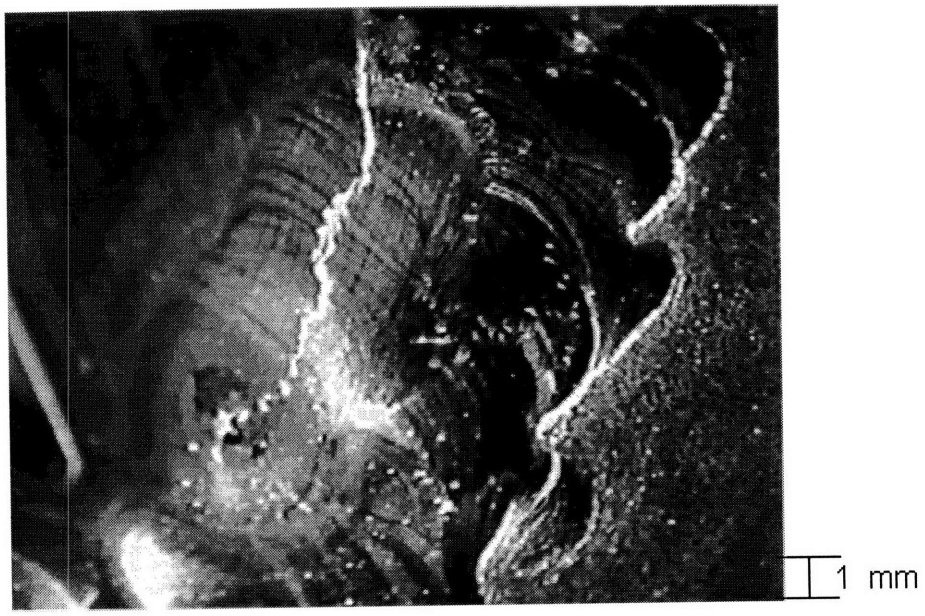

Crack propagation along the width of the weld (C)

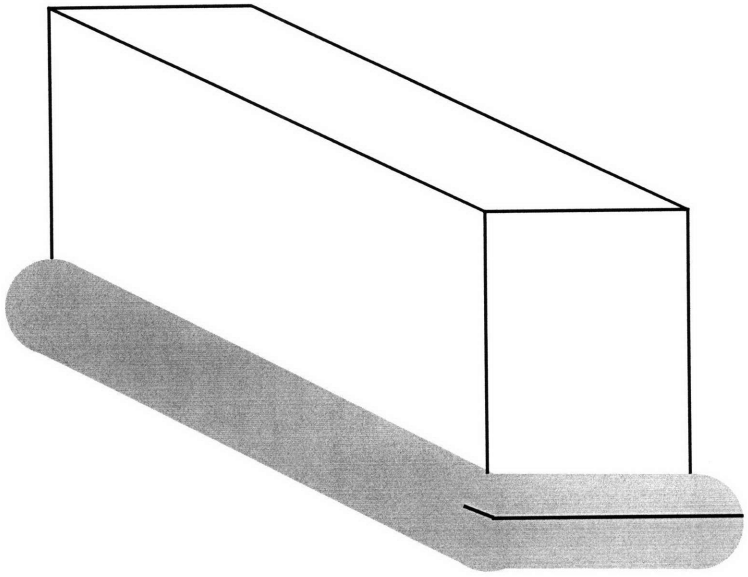

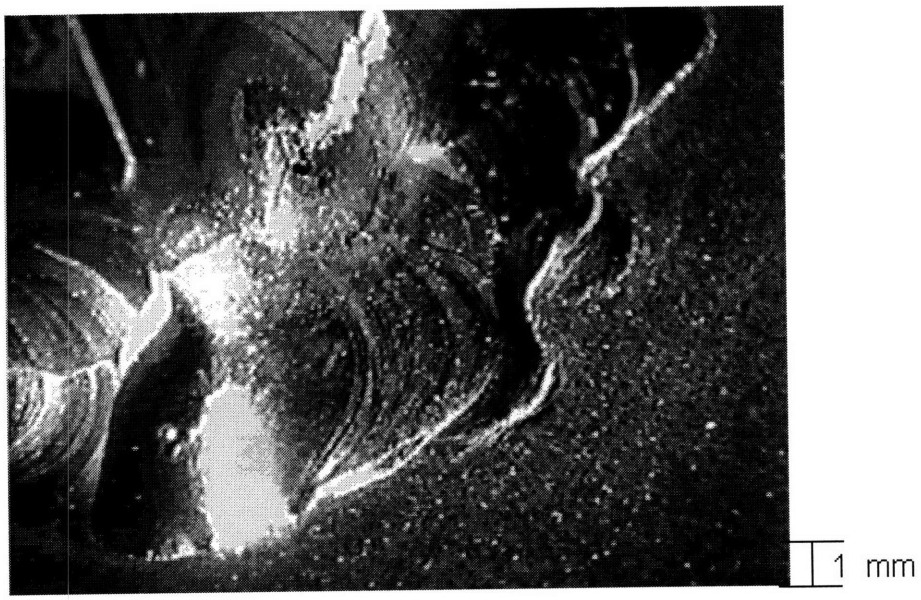

Steady state peeling fracture initiation (D)

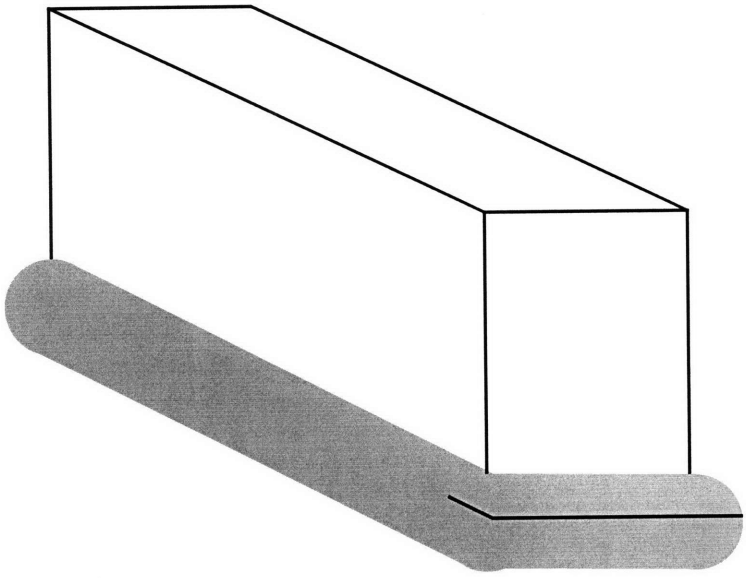

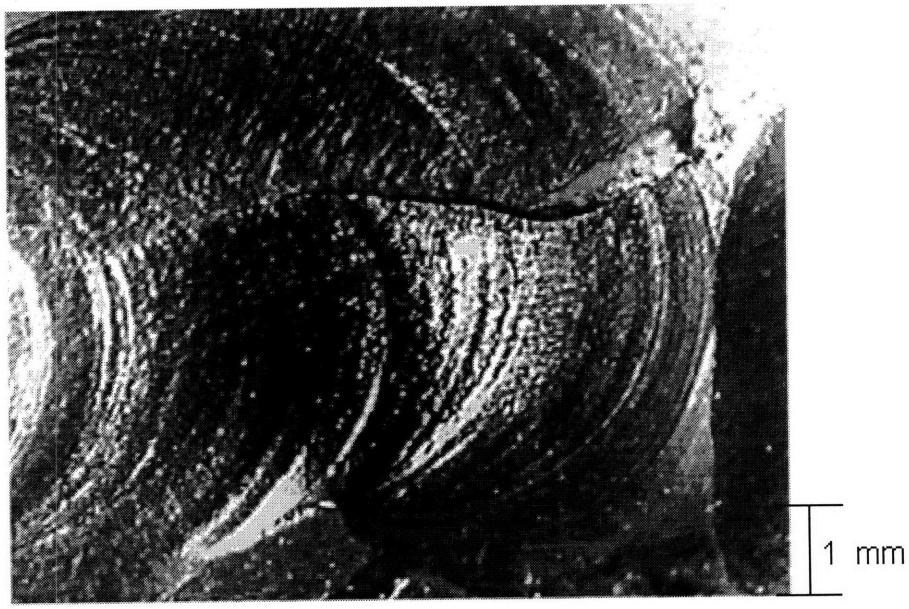

Peeling fracture of the fillet weld (E)

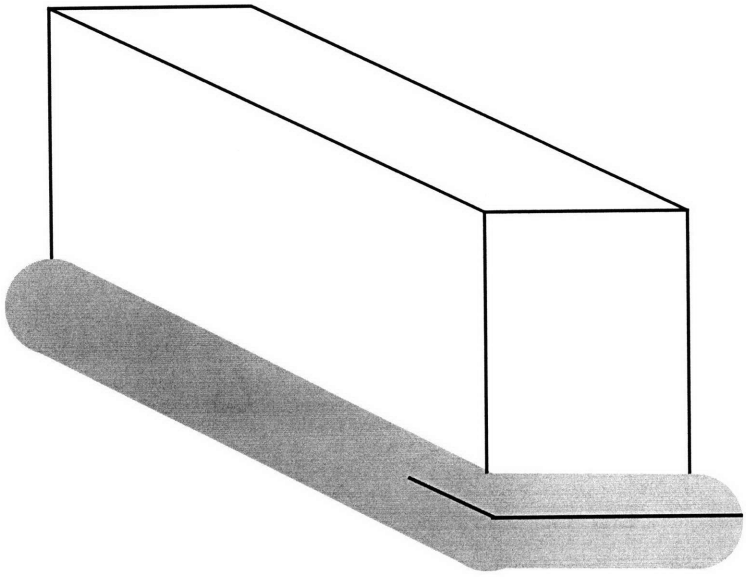

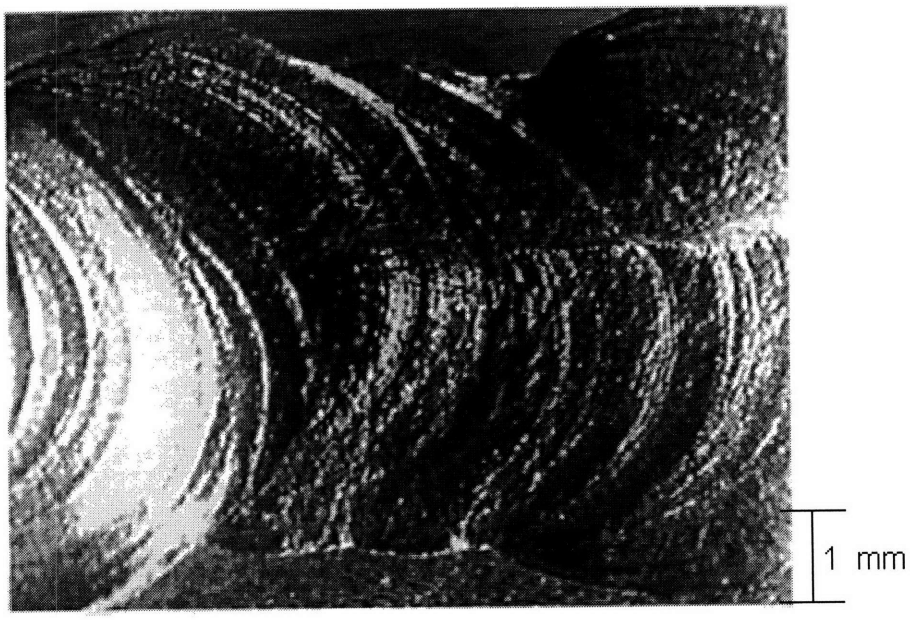

Peeling fracture of the fillet weld (F)

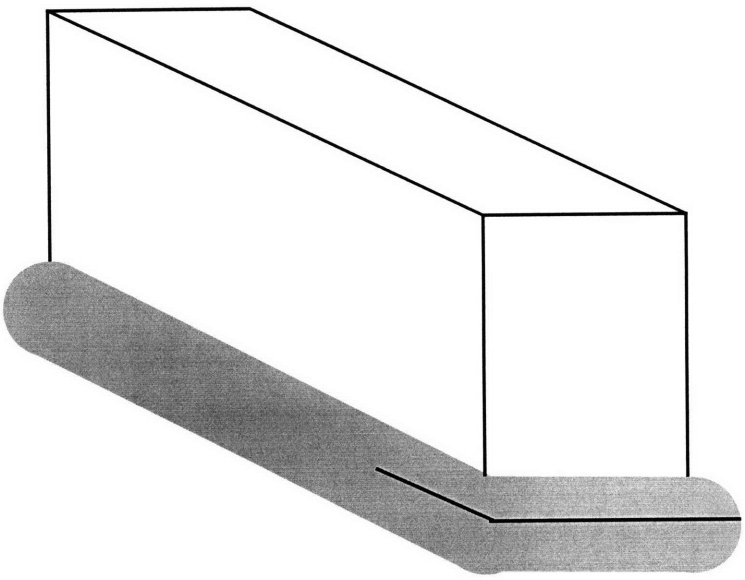

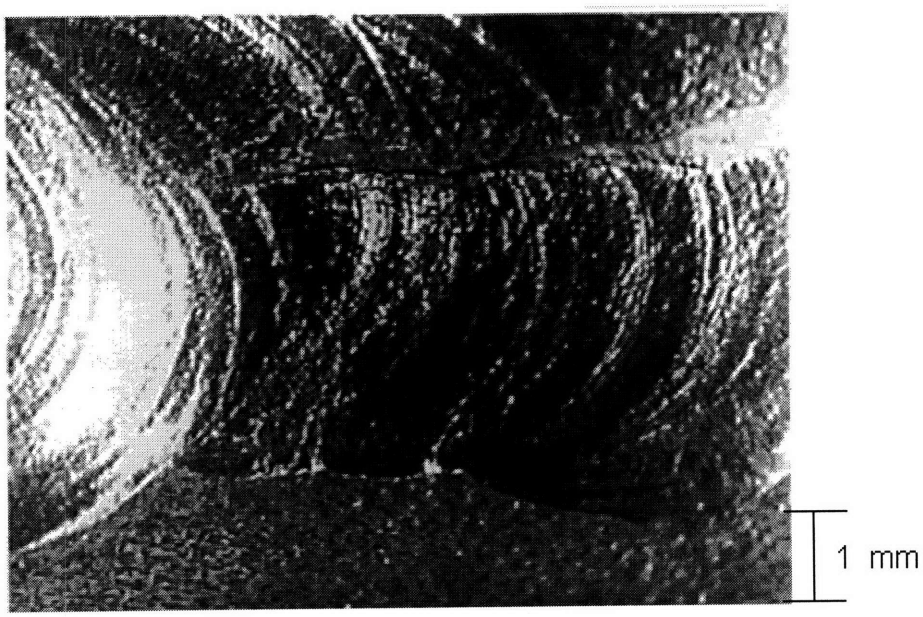

Final point of longitudinal weld tearing (G)

Specimen 5

Point definition

Point	Load (lbs)	Displacement (mils)
A1	4235	543
B1	4750	860
C1	4875	1614
A2	4380	399
B2	5080	832
C2	5125	1020
D2	4925	1336

Crack initiation at the tip of the notch (A1)

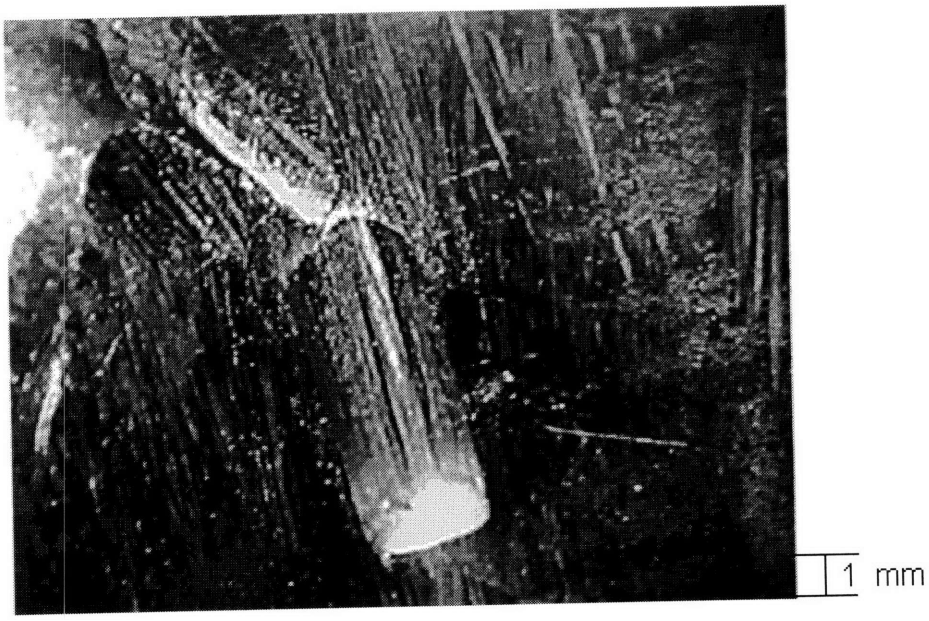

Crack appearance at point B1

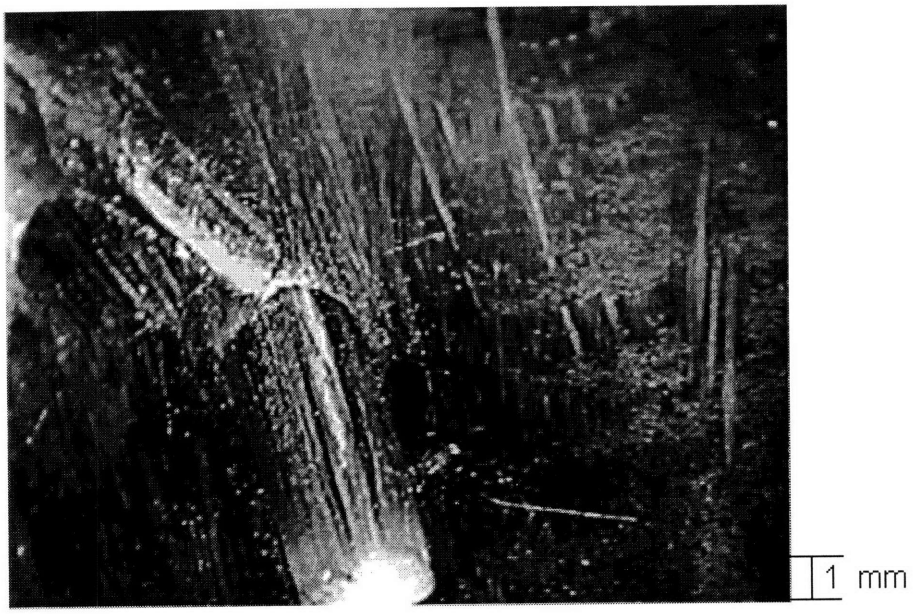

Crack appearance at point C1

Crack initiation at the low end of the notch at the surface of the base plate (A2)

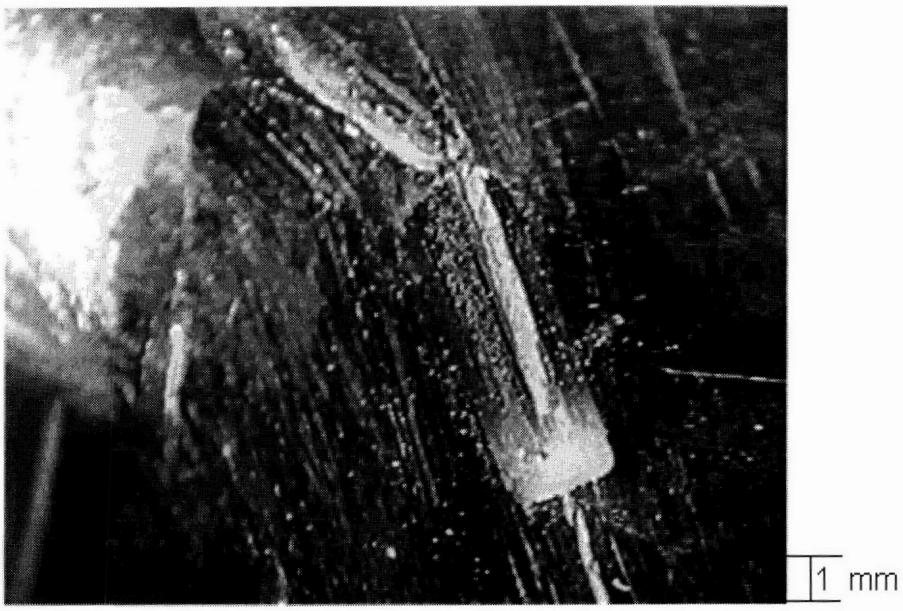

Crack appearance at point B2

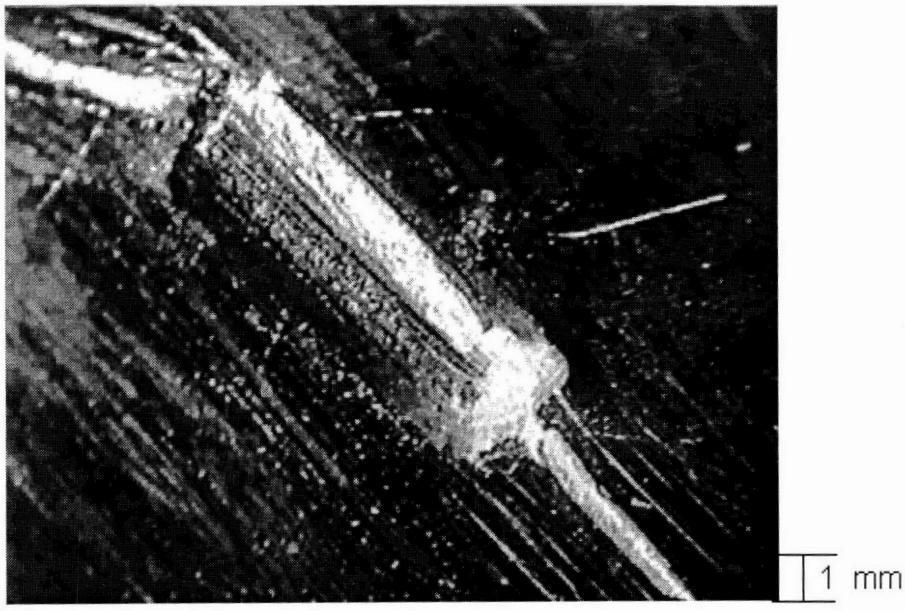

Crack appearance at point C2

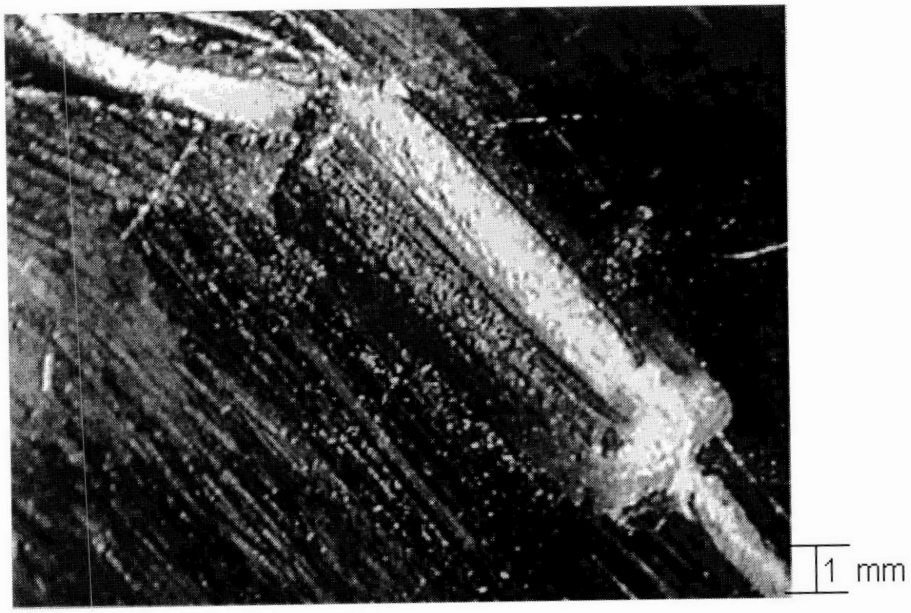

Crack appearance at point D2

Specimen 6

Point definition

Point	Load (lbs)	Displacement (mils)
A1	4740	803
B1	5060	1210
C1	5000	1743
A2	4650	394
B2	5150	581
C2	5360	1019
D2	5140	1325

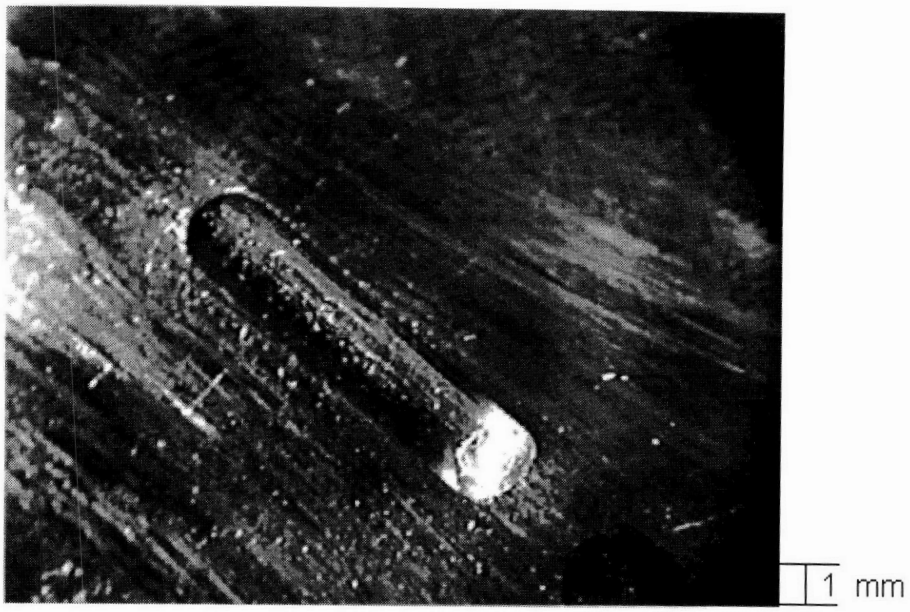

Crack initiation (A1)

Multiple cracking in the notch and crack initiation at the notch end at the plate surface (B1)

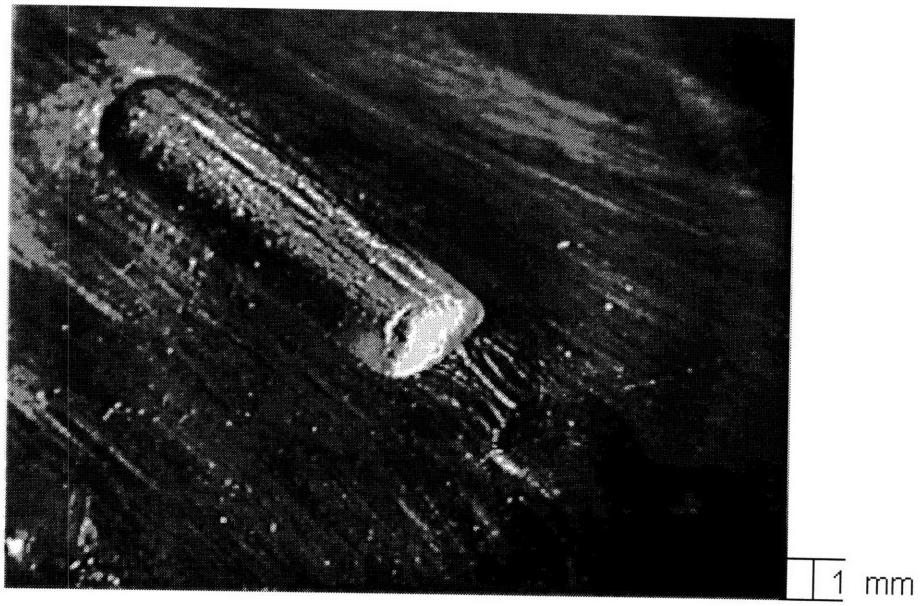

Multiple cracking at the final stage of the first loading cycle (C1)

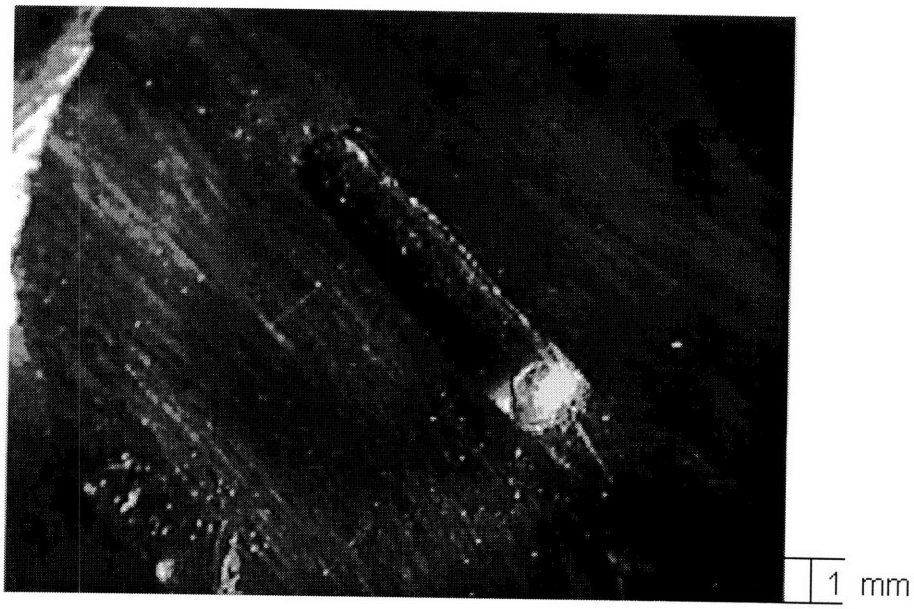

Single cracking appearance at the second cycle (A2)

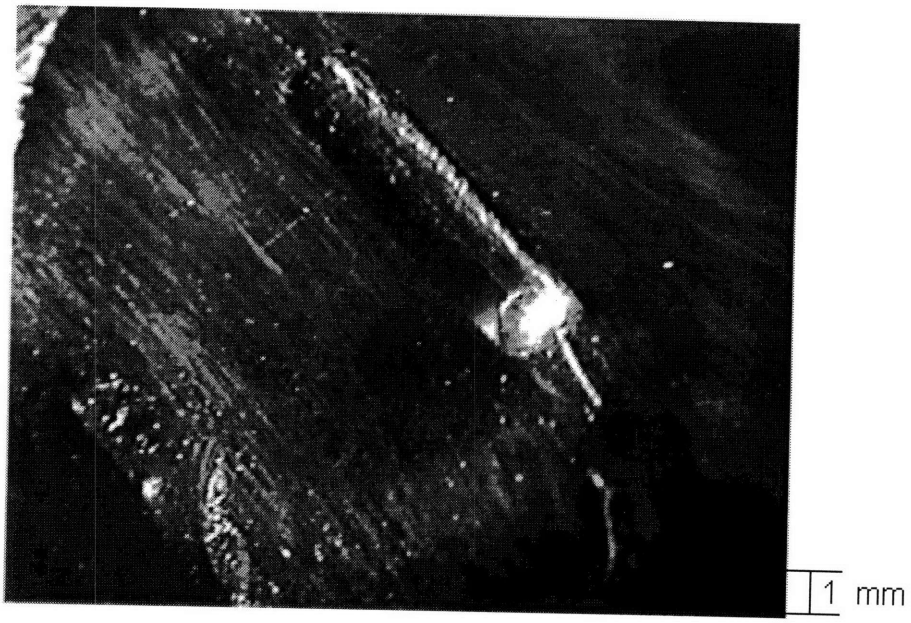

Crack appearance at point B2

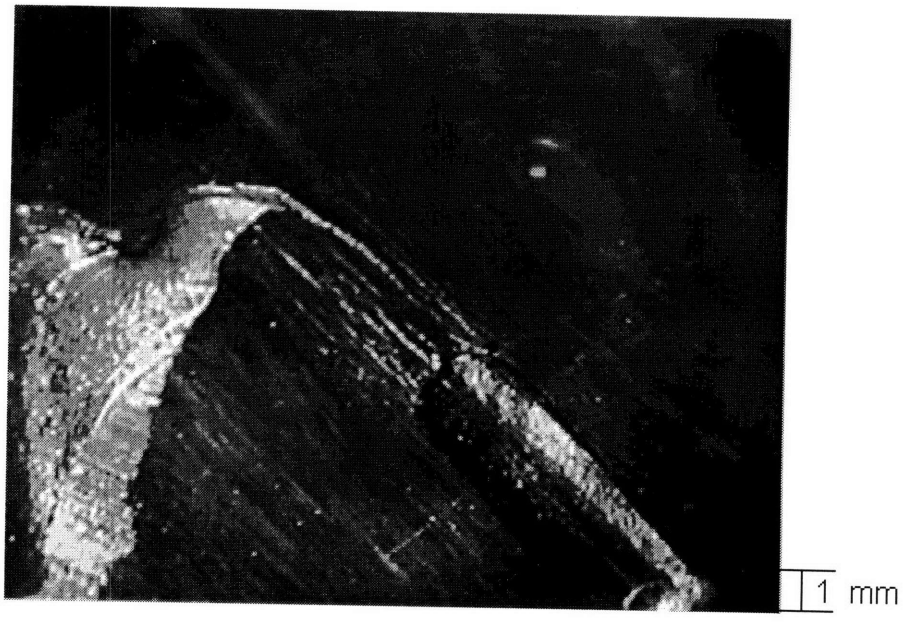

Crack appearance at point C2

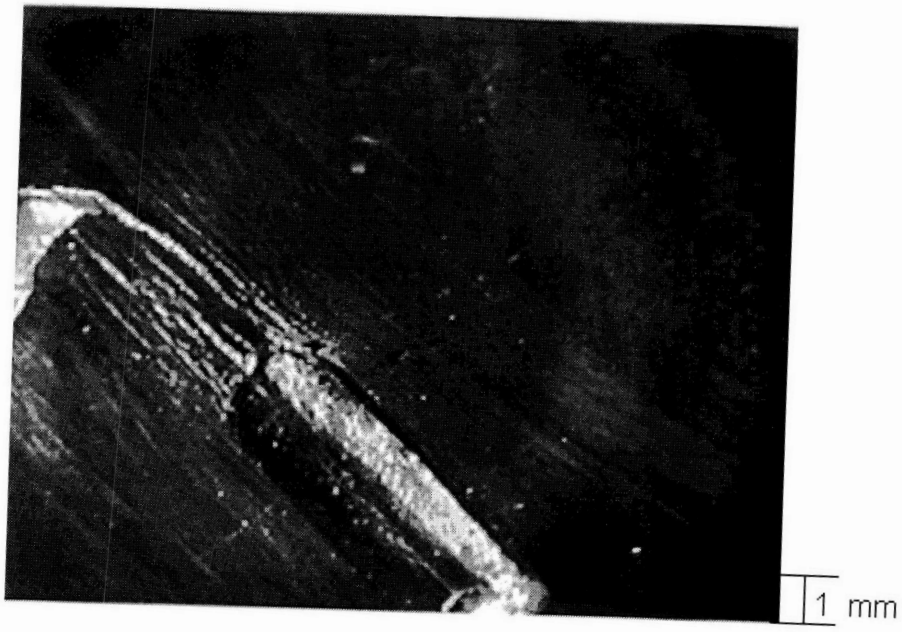

Crack appearance at point D2